sciendo

Journal of Environmental Geography 13 (3–4), 1–14.

DOI: 10.2478/jengeo-2020-0007
ISSN 2060-467X

ENVIRONMENTAL ARMED CONFLICT ASSESSMENT USING SATELLITE IMAGERY

Fernando Arturo Mendez Garzón[1]*, István Valánszki[1]

[1]Szent István University (SZIE), Department of Landscape Protection and Reclamation
+36-1-305-7387, H-1118 Budapest, Villányi út 29-43
*Corresponding author, e-mail: famendezg@yahoo.com.mx

Research article, received 8 February 2020, accepted 11 August 2020

Abstract

Armed conflicts not only affect human populations but can also cause considerable damage to the environment. Its consequences are as diverse as its causes, including; water pollution from oil spills, land degradation due to the destruction of infrastructure, poisoning of soils and fields, destruction of crops and forests, over-exploitation of natural resources and paradoxically and occasionally reforestation. In this way, the environment in the war can be approached as beneficiary, stage, victim or/and spoil of war.

Although there are few papers that assess the use of remote sensing methods in areas affected by warfare, we found a gap in these studies, being both outdated and lacking the correlation of remote sensing analysis with the causes-consequences, biome features and scale. Thus, this paper presents a methodical approach focused on the assessment of the existing datasets and the analysis of the connection between geographical conditions (biomes), drivers and the assessment using remote sensing methods in areas affected by armed conflicts. We aimed to find; weaknesses, tendencies, patterns, points of convergence and divergence. Then we consider variables such as biome, forest cover affectation, scale, and satellite imagery sensors to determine the relationship between warfare drivers with geographical location assessed by remote sensing methods. We collected data from 44 studies from international peer-reviewed journals from 1998 to 2019 that are indexed using scientific search engines. We found that 62% of the studies were focused on the analysis of torrid biomes as; Tropical Rainforest, Monsoon Forest / Dry Forest, Tree Savanna and Grass Savanna, using the 64% Moderate-resolution satellite imagery sensors as; Landsat 4-5 TM and Landsat 7 ETM+. Quantitative analysis of the trends identified within these areas contributes to an understanding of the reasons behind these conflicts.

Keywords: armed conflict, biomes, land use change, remote sensing, deforestation

INTRODUCTION

The complex relation between warfare and environment has been studied relatively little; one exception is the Report on the Protection of the Natural Environment in Armed Conflict made by the International Law and Policy Institute ILPI (2014). The report shows that war may generate large damage to the environment and populations that depend upon natural resources. Attacks produce direct harm on animals, vegetation, soil, and water systems, with consequent impacts on local or regional ecosystems. Vast defoliation campaigns are also utilized by combatants to realize strategic dominance. Meanwhile, serious contamination may incidentally result as an outcome from attacks on industrial sites, oil wells or other infrastructure (Gorsevski et al., 2012; Hanson et al., 2008; ILPI, 2014; Jha, 2014; Le Billon, 2001; Murad and Pearse, 2018; Potapov et al., 2012; Butsic et al., 2015). Secondary consequences such as displacement may in turn take tolls on the natural environment (Leiterer et al. 2018; Sanchez-Cuervo and Aide, 2013). In some cases, the environmental impacts of warfare extend over large regions and continue for years or perhaps decades after the conflict finishes.

The armed conflict is a less well-studied driver of deforestation (Machlis and Hanson, 2008; Butsic et al., 2015), which is unfortunately recurrent in tropical forests worldwide (Geist and Lambin, 2002; Gorsevski et al., 2012; Hecht and Saatchi, 2007). Empirical investigations as ILPI (2014) suggest a complex link between warfare and forest conservation (Armenteras et al., 2006; Draulans and Van Krunkelsven, 2002; Gorsevski et al., 2012; Rustad et al., 2008). Additionally, Machlis and Hanson (2008) and Butsic et al. (2015) have widely studied the direct effects of the conflict that includes road building, deforestation, and unsustainable use of natural resources. Indirect effects may include reduced economic activity during the wartime, which could reduce vegetation cover, and increase changes in land use (Jha, 2014; Stevens et al., 2011). It has been proven that these impacts remain in post-conflict times (Nackoney et al., 2014). Notwithstanding, experimental researches indicate that warfare may have both negative and positive results regarding wild forest conservancy (Rincon-Ruiz et al., 2013; Rustad et al., 2008) even in local areas (Gorsevski et al., 2013, Butsic et al., 2015). Additionally, the effectiveness of protected areas in times of hostilities also modifies over space and time (de Merode et al., 2007).

The appraisal of the implications of warfare on the environment is especially challenging due to the endogenous nature of vegetation cover loss and land-

use changes. Warfare is also the outcome and/or the reason behind deforestation, implying a tight, unique, and particular relation. Neglecting this particularity in models of deforestation can produce biased coefficients and standard errors, thus constraining our ability to know the causal structure between warfare and deforestation in a statistical frame (Blackman, 2013; Butsic et al. 2015).

Ordway (2015) has demonstrated that wartime and post-conflict period may relate to land use and land cover activities to clout the alteration of the landscape and increase forest deterioration. Land use changes have promoted the devastating deterioration in biodiversity through habitat dissolution, modification and destruction, resulting in the decline of ecosystems and environmental services (Jha, 2014; Kwarteng, 1998; Ordway, 2015; Nackoney et al., 2014; Qamer 2012 et al., 2005). The increasing amount of literature framing various direct and indirect consequences of armed conflict on the environment has created diverse hypotheses (Black, 1994; Jarret, 2003; Machlis and Hanson, 2008; McNeely, 2003; Omar and Bath, 2009; Ordway, 2015). In fact, some assessments have shown that conflict and warfare can stimulate deforestation or promote vegetation cover recovery (Alvarez, 2003; Biswas and Tortajada-quiroz, 1996; Dávalos, 2001; Hecht and Saatchi, 2007; Lodhi et al., 1998; McNeely, 2003).

Armed conflict causes and effects on the environment

Direct causes are all activities that are physically associated with direct action of confrontation which generally appears within the immediate or short-term (bombings, direct armed confrontations, military infrastructure). While indirect causes are those that are frequently linked to several causes not necessarily military and only reveal themselves fully within the medium or long-term (Jha, 2014; Mendez and Valánszki, 2019; Partow, 2008; Solomon et al., 2018) (Fig. 1).

Some examples of direct effects encompass the intentional loss of natural resources, environmental pollution from the bombing of industrial areas, the military remains, and explosion wastes from military infrastructure. Furthermore, Solomon et al., (2018) affirms that indirect impacts include the ecological footprint of displaced communities (Hagenlocher et al., 2012), deforestation as a result of new expansion areas, the increase of illegal crops and illegal mining, the impossibility of the implementation of the

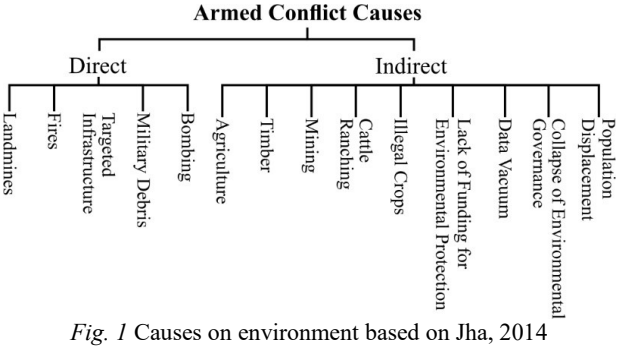

Fig. 1 Causes on environment based on Jha, 2014

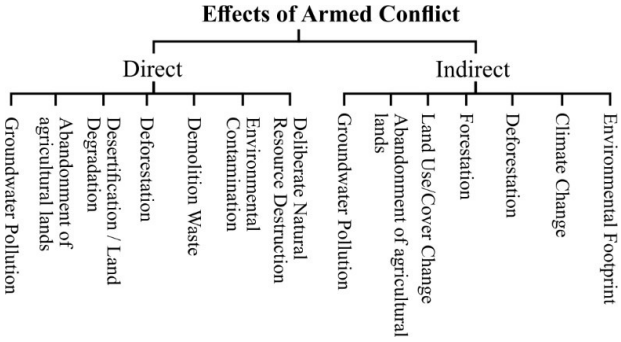

Fig. 2 Effects of conflict on environment based on Jha, 2014

environmental regulations, and also the information gaps, in addition to the lack of funds for environmental conservation. Another complementary problem is that any conflict destroys buildings and infrastructure that has to be rebuilt costing large resources and increasing emissions (Jha, 2014; Solomon et al., 2018) (Fig. 2).

Witmer (2015) affirms that the impacts can be classified into four categories, arranged by time required for each consequence to be visible. For instance, physical harm generated by bomb or fire detonations is commonly an immediate effect, which appears in minutes or hours. Alternative impacts like environmental damage (hours to days), population forced and unforced displacement (days to months), and changes of land cover/use (months to years) take longer to emerge. Even though there is some overlap between various impacts of warfare between direct and indirect, this classification creates a convenient and methodical way of approaching research.

Satellite imagery and armed conflicts

Initially, Remote Sensing (RS) methods, including aerial photos, were used for analysis in conflict zones with warlike purposes. This is due to the military sector having for a long time been a source of technological innovation with enough financial resources to invest in RS research (Corson and Palka, 2004). Advances in photography, airplanes, and satellites have largely improved the efficacy of battleground monitoring, with many military helicopters, airplanes, and unmanned aircraft systems (UASs) now capable of grabs video evidence registering the effectiveness of air and ground attack missions. Improvements in RS technology and satellite imagery have increased the effectiveness of armies and the accuracy of military operations (Witmer, 2015).

The complicated access to a zone in wartime combined with a diffuse spatial and/or temporal definition makes a precise and timely evaluation of the effects highly demanding (Gorsevski et al., 2012; Uriarte et al., 2010; Butsic et al., 2015). Due to these restrictions, info acquired from satellite imagery can bring a wide vision of how confrontations affect directly the physical environment during wartime and post-conflict, and how indirect causes drive shifts in local communities, land-uses and land-covers (Hoffmann et al., 2018; Murad & Pearse, 2018). As a result of the cause-consequence complex interdependence generated by the warfare and the need for larger protection efforts, the link between conflict

and ecosystem needs to be investigated more deeply (Ordway, 2015). Resolution is a major aspect of the usage of RS methods. Spatial, spectral, and temporal resolutions are perchance the most important but radiometric resolution also affects what can be perceived. Table 1 lists the sensors frequently used to detect the effects of armed conflict. The sensors are grouped by spatial resolution which are Very Fine ≤1 m, Fine >1-10 m, Moderate >10–120 m, and Coarse >250 m.

Aim

Although we found two studies that assess the use of RS analysis in areas impacted by armed conflicts (Solomon et al., 2018; Witmer, 2015), these studies present a gap in research because they do not cover many types of research related to conflicts and environment. Furthermore, these studies are outdated regarding the latest RS methods and satellite sensors. The diversity of methods, classifications, satellite imagery sensors, and approaches for RS calls for a systematic revision that addresses their relation to conflict features such as biome type and geographical location, conflict causes-consequences, and the study area scale. Our aim is the assessment of the existing studies to identify relationships and patterns (and, implicitly, differences) in order to methodically approach the warfare-environment issue within an accurate and integral view for each specific type of conflict in future investigations.

This study seeks to offer an overview of the most important tendencies in the usage of RS as a tool for environmental damage assessment in warfare areas. Our aim is to demonstrate the specific correlation between armed conflicts (causes) and environment (consequences) using state-of-the-art RS technology to provide conditioned geospatial environmental information. More exactly, this paper presents an integrative and transferable approach for the quantification, systematic comparison, and evaluation of the RS studies used in zones affected by armed conflicts.

The impacts outlined in this paper, such as deforestation or land-use/land-cover changes, were quantified systematically and in exclusive regard to their RS analysis. This means that results here provided are considered applicable and relevant for the analysis of RS studies and are not necessarily applicable nor usually considered accurate for armed conflicts in general. Other scopes will be considered in future investigations.

Table 1 Characteristics of commonly used sensors

Sensor	Spatial resolution [m]	Swath width [km]	Spectral bands	Operating period	Active	Domain	Origin
Very fine spatial resolution (≤1m)							
GeoEye	0.46	10	Pan	09-2008 - Currently	Yes	Pr	US
World View II	0.46	18	Pan	10-2009 - Currently	Yes	Pr	US
QuickBird II (Pan)	0.6	30	Pan	10-2001 to 12-2014	No	Pr	US
IKONOS (Pan)	0.82 - 1	11	Pan	09-1999 to 03-2015	No	Pr	US
Fine spatial resolution (>1–10m)							
GeoEye	1.84	10	4	09-2008 - Currently	Yes	Pr	US
QuickBird II (MS)	2.4	30	4	10-2001 to 12-2014	No	Pr	US
ALOS	2.5		Pan	01-2006 to 05-2011	No	Pu	JP
SPOT-5	2.5, 5, 10	60	Pan	05-2002 to 03-2015	No	Pu	FR
CBERS-2B	2.7	27	Pan	09-2007 to 06-2010	No	Pu	CN-BR
IKONOS (MS)	3.28 – 4	11	4	09-1999 to 03-2015	No	Pr	US
KVR-1000 (MS)	3.3	40	4	1994 - N.D.	No	Pu	RU
Rapid Eye	5	77	5	02-2009 to 03-2020	No	Pr	DE-UK
Google Earth VHR	5, 10	N.A.	Pan	N.A.	Yes	Pr	US
IRS 1C LISS III	6	70	Pan	12-1995 - 09-2007	No	Pu	IN
Moderate spatial resolution (>10–120m)							
Sentinel 2	10, 20, 60	290	13	06-2015 - Currently	Yes	Pu	EU
ASTER	15, 30, 90	60	14	02-2000 - Currently	Yes	Pu	US-JP
Landsat 8 OLI	15, 30	185	11	02-2013 - Currently	Yes	Pu	US
Landsat 6-7 ETM +	15, 30	185	8	10-1993 - Currently	Yes	Pu	US
IRS 1C LISS III	23, 50	142	4	12-1995 to 09-2007	No	Pu	IN
Landsat 4-5 TM	30	185	7	07-1982 to 06-2013	No	Pu	US
Landsat 1-3 MSS	60, 120	N.D.	4	07-1972 to 01-1983	No	Pu	US
Coarse spatial resolution (>250 m)							
MODIS	250, 500, 1000	2330	36	1999 to 2005	No	Pu	US
VIIRS	375, 750	3060	22	10-2011 - Currently	Yes	Pr	US
AVHRR	1100, 4400	2500	5, 6	03-2004 - Currently	Yes	Pu	US-EU
Radar Data - No Category							
LIDAR	1	N.A.	N.A.	N.A.	Yes	Pr	N.A.
Aerial Photos		N.A.	N.A.	N.A.	N.A.	Pr / Pu	N.A.

Abbreviations: (N.D) No Date, (N.A.) Not Applicable, (PAN) Panchromatic, (Pr) Private, (Pu) Public

The questions motivating this paper are:

- What is the relationship between remote sensing sensors and the geographical / biome location of the study area?
- How are the remote sensing sensors and the scale of the study area related?
- What is the relationship between causes generated by the armed conflict (indirect and direct drivers) and the study area type of biome?
- What is the relationship between armed conflict consequences and the study area type of biome?

MATERIALS AND METHODS

RS assessment has been used at least in 21 countries across 4 continents as an approach to armed conflict and their environmental effects. For the data collection and the analysis of methods, we looked for articles and data sets through scientific search engines using the following keywords: "Remote sensing + Armed Conflict", "Biomes + Armed Conflict" and "Deforestation + Armed Conflict". Then we made a filtered search based on the indicators (satellite sensor, resolution, scale, cause, consequence, biome, location, imagery preprocessing, etc.). We collected and analyzed 116 studies. After a second and deeper revision, we chose 44, documents that fulfilled all or almost all the parameters required for the assessment. These are listed in Table 2. The documents were read, evaluated, synthesized, and tabulated for their processing. Although the studies analyzed were carried out from 1998 to 2019, they do not necessarily correspond to the time when the armed conflicts occurred. The majority of the studied armed conflicts occurred between 1980 and the present.

In order to evaluate the datasets from 44 studies that used satellite imagery and aerial photos, we framed the assessment seeking the following parameters: study area size, armed conflict causes and consequences, types of causes (direct or indirect), affectation of forest cover (increase or decrease), time-lapse, satellite imagery sensor, spatial resolution, conflict period, imagery preprocessing, imagery classification, geographical location, and type of biome. Quantitative analysis of the parameters identified within these studies contributed to an understanding of the reasons behind these consequences. Their correlations can be useful for future research suggestions and can work as a guideline of RS assessment in areas affected by conflict. Besides the assessment of satellite resolution, we analyzed the micro and macro-level consequences that can be drawn in the resulting inventory mapping of comprises statistics charts, patterns, trends, and findings on RS and its relationship with the armed conflict. This was done in the context of a comprehensive review, processing, tabulating, appraising, and synthesis of collected data.

Table 2 Features of remote sensing studies of armed conflict repercussions in the environment

Country	Scale (km^2)	Causes	Consequences	Sensor	Reference
Kuwait	Re	Bo	LU, LC	LS4-5	Abuelgasim et al. 1999
N. Macedonia, Palestine	Re	N.D.	N.D.	IKONOS	Al-Khudhairy et al. 2005
Colombia	Re 42000	Ag, CR, Ti	Df	LS1-3, LS4-5, LS6-7	Armenteras et al. 2006
Colombia	Na 1,142,000	NFM, IC, Ag, CR, Ti, Fi	Df	LS4-5, LS6-7	Armenteras et al. 2013
Thailand	Lo	FM	LU	KVR-1000	Bjorgo 2000
Sierra Leona	Re 71740	Bo, DC, MI	Df	LS4-5, LS6-7	Burgess et al. 2015
Colombia	Na 1,142,000	Mn, Ag, CR	Df, LU	LS6-7, LS8, ASTER, Se, CBERS, RE	Cabrera et al. 2019
Colombia	Re	IC	Df	LS6-7	Chadid et al. 2015
Liberia	La 1639	DC, MI, FM, Ms, Ag	Df, Ds, LU, LC	LS4-5, LS6-7, LS8	Enaruvbe et al. 2019
Colombia	Re 25000	FM, CR	Df, LU, LC	ASTER	Garcia-Corrales et al. 2019
Sierra Leona	Lo 557	FM, NFM, Ag	Df, LU, LC	SPOT-5, LS1-3, LS4-5, LS6-7	Gbanie et al. 2018
Belgium	La 2500	Bo	MI	AP, ALS	Gheyle et al. 2018
Colombia	Lo 935	Mn	Df, LU	LS6-7	Gómez-Rodríguez et al. 2017
S. Sudan, Uganda	La 8375	FM	Df, Fo, Ds, AAL	LS4-5, LS6-7, MODIS, AP	Gorsevski et al. 2012
South Sudan	La 1032	FM	Df	SPOT-5	Gorsevski et al. 2013
South Sudan	La	FM	Df, Ds, LD, Gw	QB	Hagenlocher et al. 2012
El Salvador	Re 21000	FM	Df	LS4-5, MODIS, AVHRR	Hecht and Saatchi 2007
Afghanistan	La	IC, Ag, CR	Df, LU, LC, AAL	GE, LS4-5	Ingalls and Mansfield 2017
Kuwait	La	Bo, DC, MI	LU	LS4-5	Kwarteng 1998
Colombia	Na 1,142,000	DC, MI, FM	Df, LU, LC	N.D.	Landholm et al. 2019
South Sudan	La	FM	Df, LC	LS4-5, LS6-7, LS8, WV2	Leiterer et al. 2018
Arab Countries	Na	Bo, DC, MI	AAL	VIIRS	Levin et al. 2018

Country	Scale (km^2)	Causes	Consequences	Sensor	Reference
Pakistan	Lo 618	FM	Df	LS1-3, LS4-5	Lodhi et al. 1998
Cambodia	Lo 50	Bo, DC, MI	Df	LS6-7	Loucks et al. 2009
Colombia	La 3927	Mn, Ag	LC	LS6-7, LS-8	Monroy and Armenteras 2017
Colombia	Re	IC, Ag, CR	Df, LU, LC	LS6-7, LS-8	Murad and Pearse 2018
R.D. Congo	La 1510	FM	Df, LU, LC	LS4-5, LS6-7	Nackoney et al. 2014
Colombia	Na 1,142,000	DC, MI, IC	Df	N.D.	Negret et al. 2019
Belgium	Lo 142,5	Bo	MC	AP	Note et al. 2018
Rwanda	La 271	FM, NFM, Ag, Ti	Df	LS4-5, LS6-7, ASTER	Ordway 2015
R.D. Congo	La	FM, NFM	LU, LC	LS4-5, LS6-7, LS8, GE-VHR, WV2	Pech and Lakes 2017
Zambia	Lo 217	N.D.	Df, LU	SPOT-5	Petit et al. 2001
R.D. Congo	Na 2,345,409	FM, NFM, Mn	Df	QB, LS6-7	Potapov et al. 2012
Pakistan	La 4109	FM, Ag, CR	Df, LU	SPOT-5, LS4-5, LS6-7, ASTER	Qamer et al. 2012
Colombia	Na 1,142,000	N.D.	Df, LU, LC	QB, GE-VHR, MODIS	Sánchez-Cuervo and Aide 2013
South Sudan	Re 23000	FM	LU, LC	MODIS	Sosnowski et al. 2016
Nicaragua	La 1600	FM	Df	LS1-3, LS4-5	Stevens et al. 2011
Belgium	La 1560	Bo	MC	AP, ALS	Stichelbaut et al. 2016
Sri Lanka	La 1125	DC, MI, Lm, FM, Ti	Df, LU, MI	LS4-5, IRS	Suthakar and Bui 2008
Myanmar	Na 236342	IC	Df, LU, LC	SPOT-5, QB, IKONOS, ALOS, ASTER	Tian et al. 2011
R.D. Congo	Na 2,345,409	DC, MI, Mn	Df, LU, LC, MI, AAL	LS4-5, LS6-7	Van Butsic et al. 2015
Turkey	La 7600	Bo, DC, MI	Df, LU, LC	LS4-5	Van Etten et al. 2008
Sierra Leone	La 5397	N.D.	Df, LU, LC	LS4-5	Wilson and Wilson 2013
Bosnia & Herzegov.	Re 3887	Bo, Lm, FM	LU, LC	LS4-5, LS6-7, QB	Witmer 2008

Abbreviations: (N.D) No Date, (N.A.) Not Applicable
Scale: (Lo) Local 0-999 km^2, (La) Landscape 1000-9999 km^2, (Re) Regional 10000-99999 km^2, (Na) National/Global ≥100,000 km^2
Causes: (Ag) Agriculture, (Bo) Bombing, (CR) Cattle Ranching, (DC) Direct Confrontation, (Fi) Fires, (FM) Forced Migration, (IC) Illegal Crops, (Lm) Landmines, (MI) Military Infrastructure, (Mn) Mining, (NFM) Non-Forced Migration, (Ti) Timber
Consequences: (AAL) Abandonment of Agricultural Lands, (Df) Deforestation, (Ds) Desertification, (Fo) Forestation, (Gw) Groundwater Pollution, (LC) Land Cover Changes, (LD) Land Degradation, (LU) Land Use Changes, (MC) Mine Craters, (MI) Military Infrastructure.
Sensor: (ALOS) Advanced Land Observation Satellite, (ALS) Lidar - Airborne Laser Scanning, (AP) Aerial Photo, (ASTER) Advanced Spaceborne Thermal Emission and Reflection Radiometer, (AVHRR) Advanced Very-High-Resolution Radiometer, (CBERS-2B) China–Brazil Earth Resources Satellite, (GE-VHR) Google Earth Very High Resolution, (GE) GeoEye, IKONOS, (IRS) IRS-1C LISS-III Indian Remote-Sensing Satellite, KVR-1000, (LS1-3) Landsat 1-3 MSS, (LS4-5) Landsat 4-5 TM, (LS6-7) Landsat 6-7 ETM+, (LS8) Landsat 8 OLI, (MODIS) Moderate Resolution Imaging Spectroradiometer, (QB) QuickBird II,(RE) Rapid Eye, (Se) Sentinel 2, (SPOT-5) Satellite Pour l'Observation de la Terre, (VIIRS) Visible Infrared Imaging Radiometer Suite, (WV2) WorldView-2

RESULTS

Armed conflict & remote sensing assessment by biomes

Unlike countries' borders, biomes' physical limits are rarely clear or defined. As a result, several studies may cover two or more biomes. Within the 44 investigations assessed, we found the use of RS in the study of 13 general types of biomes and the assessment in 92 different cases. This means that each study could have used more than one sensor to assess two or more biomes, depending on the area, complexity, and the availability of satellite imagery data set. The analysis outcome regarding the number of studies by biome indicates that high biodiversity spots near the equatorial line such as tropical rainforest (23), monsoon forest/dry forest (17), tree savanna (7) and grass savanna (6) cover the biggest number of studies. Furthermore, we found a considerable number of studies located in subtropical areas, a diverse number of biomes as a montane forest (13) temperate broadleaf forest (5), semi-arid desert (4), alpine tundra (4), subtropical dry forest (4) and subtropical rainforest (1). Finally, we identified few studies performed in the temperate biomes; Mediterranean vegetation (3), dry steppe (2), and xeric shrubland (1) (Fig. 3 & 4).

Relationship between satellite imagery sensors and biomes

Regarding the satellite sensors used, we observed that two-thirds (64%) of the biomes were analyzed by sensors with moderate resolution (10-120 m) where Landsat 4-5 TM and Landsat 7 ETM+ stand out (e.g., Armenteras et al., 2013; Butsic. et al., 2015; Gorsevski et al., 2012; Leiterer et al., 2018; Murad and Pearse, 2018). We found that Very fine (≤1m) and Fine (1-10m) resolution sensors covered 23% of the biomes, with SPOT-5 and QuickBird II sensors slightly standing out (e.g., Petit et al., 2001; Qamer et al., 2012).

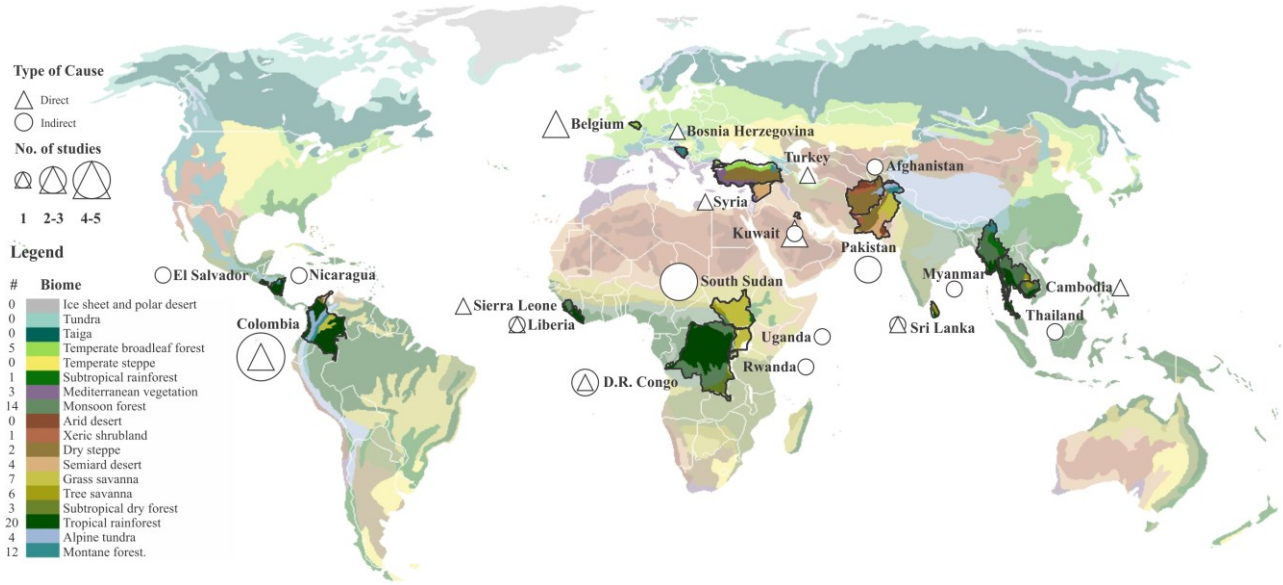

Fig. 3 Armed conflict causes analyzed using remote sensing by biomes and countries

Uncategorized sensors covered 7% of the biomes, aerial photographs, and Lidar ALS sensor stands out within this segment (e.g., Note et al., 2018). Finally, coarse sensors (>250 m) covered 6% of the biomes in which MODIS sensor was the most outstanding (e.g., Gorsevski et al., 2012; Hecht and Saatchi, 2007; Sánchez-Cuervo and Aide, 2013; Sosnowski et al., 2016) (Fig. 5).

Table 3 was obtained after crossing the data between the study area type of biome and the satellite imagery sensors used for RS. The outcome indicates that the most common satellite imagery sensors used was the moderate resolution sensors (10-120 m) with 61% of the total, mainly Landsat 4-5 TM and Landsat 7 ETM+ in the analysis of biomes such as tropical rainforest, monsoon forest/dry forest, montane forest, and tree savanna. The Very fine (≤1 m) and Fine (1-10 m), resolution sensors were used in 27% of the studies per biomes; Spot 5, QuickBird, and Google Earth VHR have been used noticeably more in the study of biomes such as tropical rainforest, monsoon forest/dry forest, montane forest, tree savanna, and grass savanna. GeoEye sensor was used once each in non-common biomes as xeric shrubland, dry steppe, and alpine tundra. Sensors with coarse resolution (>250 m) were utilized in the 8% of the total and highlight the use of MODIS for several types of biomes. Uncategorized sensors were used rarely (4% of the total). Aerial photos and LIDAR ALS were used mainly in the temperate broadleaf forest.

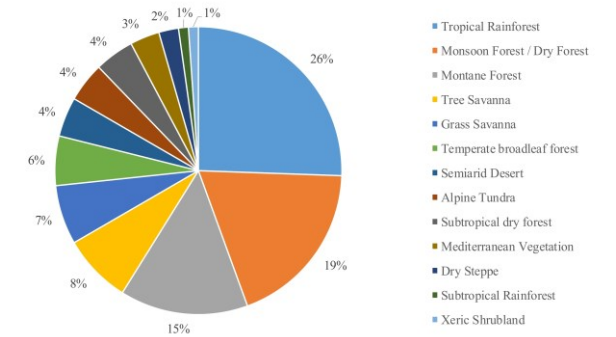

Fig. 4 Biomes analyzed for occurrence in the studies

Relationship between satellite imagery sensors and study area scale

To analyze and study the relationship between the use of satellite image sensors and the scale of the area affected by armed conflict, we first categorized the scale sizes into four types: Local (0-999 km^2), Landscape (1000-9999 km^2), Regional (10,000-99,999 km^2) and National/Global (≥100,000 km^2). Then, we checked, crossed the data and created a correlation table to identify trends and patterns of repetition. We obtained the following results: moderate resolution (10-120 m) sensors such as Landsat 4-5 TM, Landsat 7 ETM+ and to a lesser extent Landsat 8 OLI are the most widely used sensors in all scales, is noticeable a clear trend in the use of these sensors mainly in studies of medium to large small such as Landscape (e.g., Gorsevski et al., 2012; Gorsevski et al., 2013; Leiterer et al., 2018; Monroy and Armenteras, 2017; van Etten, 2008), and Regional (e.g., Armenteras et al., 2006; Burgess et al., 2015; Hecht and Saatchi, 2007; Witmer, 2008).

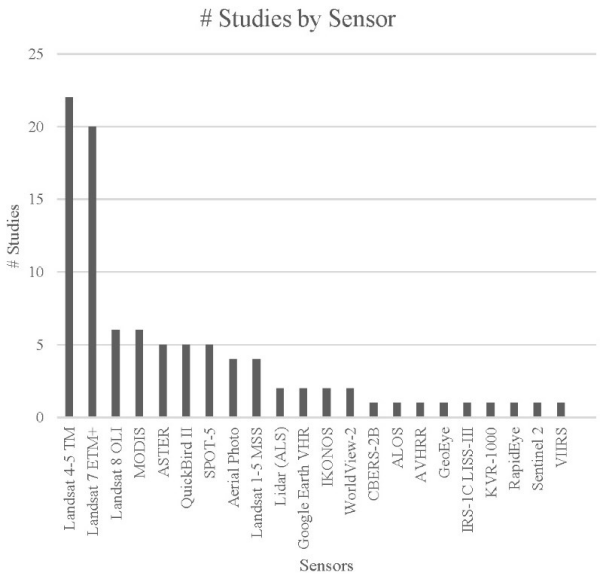

Fig. 5 Distribution by satellite sensor

In addition, we observed that high (1-10m) and very high-resolution (≤1m) satellite image sensors such as QuickBird, IKONOS, RapidEye, and CBERS were barely used in studies that analyzed sites with small scales such as Regional (10,000-99,999 km^2) and National/Global (≥100,000 km^2) excepting SPOT-5 and KVR-1000 that were used mainly in smaller scales. Concerning coarse (>250 m) sensors, the use was very low with the MODIS sensor standing out slightly on the regional scale. The aerial photos and ALS sensors were used primarily in researches that use Landscape scale. Several studies used more than one sensor to fulfil the gaps of information that the use of a single sensor can offer. This produces that each study can use the satellite images from more than one sensor mainly when Landsat data does not provide sufficient cloud-free coverage imagery or the availability does not cover the required period (Table 4).

Preprocessing of satellite imagery sensors

Preprocessing involves geometric (orthorectification) and radiometric calibration. Geometric calibration corrects for the angle of sight of the satellite sensor, the relief of the ground, and lens distortions in order that images from different sensors at different times may be compared with the same way as maps made using the identical projection and scale (Warner et al., 2009). Radiometric calibration is recommended due to the appearance of the identical image varies with the angle of view and radiance conditions. Of the 44 studies analyzed, 18% mentioned explicitly the utilization of satellite imagery preprocessing methods. For the reflectance calibration and image normalization, top-of-atmosphere (TOA) data was used 15 times in five studies (e.g., Cabrera et al. 2019; Enaruvbe et al. 2019; Potapov et al. 2012; Stevens et al. 2011; Wilson and Wilson 2013). In the case of top of canopy (TOC) reflectance data sets were performed just in one study (Potapov et al. 2012) with two satellite imagery sensors. Finally, the cloud presence was removed through atmospheric corrections using the Atmospheric & Topographic Correction - ATCOR-2 for haze removal in two studies with three Landsat sensors (e.g., Kwarteng 1998; Murad and Pearse 2018) (Table 5).

Table 3 Relationship between satellite imagery sensors and biomes

	Sensor vs Biome	Temperate broadleaf forest	Subtropical Rainforest	Mediterranean Vegetation	Monsoon Forest / Dry Forest	Xeric Shrubland	Dry Steppe	Semiarid Desert	Grass Savanna	Tree Savanna	Subtropical dry forest	Tropical Rainforest	Alpine Tundra	Montane Forest	**Total**
Very fine (≤1m) and Fine (1 - 10m)	SPOT-5		1		2				1	1	1	2	1	1	10
	QuickBird II			1	2				2	1		3	1	2	12
	IKONOS	1		1	1			1				1			5
	WorldView-2								1	1		1			3
	GeoEye					1	1						1		3
	ALOS				1							1			2
	CBERS-2B											1		1	2
	KVR-1000 (MS)				1							1			2
	Rapid Eye											1		1	2
	Google Earth VHR				1				1	1		2	1	1	7
Moderate (10–120 m)	Landsat 1-3 MSS				1							3		1	5
	Landsat 4-5 TM	1		1	8	1	2	2	1	3		12	2	6	39
	Landsat 6-7 ETM+			1	10				1	2	1	14	1	9	39
	Landsat 8 OLI				1				1	1	1	4		2	10
	ASTER				3					1	1	4	1	3	13
	Sentinel 2											1		1	2
	IRS-1C LISS-III									1		1			2
Coarse (>250 m)	MODIS				2				2	2	1	4	1	3	15
	VIIRS			1			1								2
	AVHRR											1			1
No Category	Aerial Photo	3			1					1				1	6
	Lidar – ALS	2													2
	Total	7	1	5	34	2	4	3	10	15	5	57	9	32	**181**

Table 4 Relationship between satellite imagery sensors and study area scale

	Sensor vs Scale	Local (0-999 km^2)	Landscape (1000-9999 km^2)	Regional (10,000-99,999 km^2)	National/global (≥100,000 km^2)	Total
Very fine (≤1m) and Fine (1 - 10m)	SPOT-5	**2**	**2**		**1**	5
	QuickBird II		**1**	**1**	**3**	5
	IKONOS			**1**	**1**	2
	WorldView-2		**2**			2
	GeoEye		**1**			1
	ALOS				**1**	1
	CBERS-2B				**1**	1
	KVR-1000 (MS)	**1**				1
	Rapid Eye				**1**	1
	Google Earth VHR		**1**		**1**	2
Moderate (10–120 m)	Landsat 1-3 MSS	**2**	**1**	**1**		4
	Landsat 4-5 TM	**2**	**13**	**5**	**2**	22
	Landsat 6-7 ETM+	**3**	**8**	**5**	**4**	20
	Landsat 8 OLI		**4**	**1**	**1**	6
	ASTER		**2**	**1**	**2**	5
	Sentinel 2				**1**	1
	IRS-1C LISS-III		**1**			1
Coarse (>250 m)	MODIS		**1**	**2**	**3**	6
	VIIRS				**1**	1
	AVHRR			**1**		1
No Category	Aerial Photo	**1**	**3**			4
	Lidar – ALS		**2**			2
	Total	11	42	18	23	**92**

Table 5 Relationship between satellite imagery sensors and preprocessing methods

	Sensor vs Preprocessing	TOA	TOC	ATCOR	IDOS	Total
Very fine (≤1m) and Fine (1–10m)	SPOT-5					0
	QuickBird II	**1**	**1**			2
	IKONOS					0
	WorldView-2					0
	GeoEye					0
	ALOS					0
	CBERS-2B	**1**				1
	KVR-1000 (MS)					0
	Rapid Eye	**1**				1
	Google Earth VHR					0
Moderate (10–120 m)	Landsat 1-3 MSS	**1**			**1**	2
	Landsat 4-5 TM	**3**		**1**	**1**	5
	Landsat 6-7 ETM+	**3**	**1**	**1**	**1**	6
	Landsat 8 OLI	**2**		**1**		3
	ASTER	**1**				1
	Sentinel 2	**1**				1
	IRS-1C LISS-III					0
Coarse (>250 m)	MODIS	**1**	**1**			2
	VIIRS					0
	AVHRR					0
	Total	15	3	3	3	**24**

Abbreviations: (TOA) Top of Atmosphere, (TOC) Top of Canopy, (ATCOR) Atmospheric & Topographic Correction, (IDOS) Improved Dark Object Subtraction

Satellite imagery sensors and imagery classification

The classifiers used for satellite image classification are split into two categories: statistical and machine learning approaches, the performance of which relies on the information distribution. The statistical learning approaches support some mathematical theories which cope with finding a relationship between classes to predict some substantial outcome (e.g., Borra et al., 2019). Maximum Likelihood Classifier was used in at least 25% of the studies. Object-based Image Analysis (OBIA) classifier was utilized in just 5% of the research. The fully automated Multivariate Alteration Detection (MAD) method was used once (2%).

Regarding indexed classification, 25% of the assessed studies, indicated explicitly the use of Normalized Difference Vegetation Index (NDVI) as a graphical indicator to analyze RS measurements. 43% of the studies used some type of Land-Cover Land-Use classification (LULC). Additionally, 36% of the studies stated the utilization of some type of Forest Cover Classification (FCC). Other multispectral vegetation indices as Enhanced Vegetation Index (EVI) and Modified Soil-Adjusted Vegetation Index (MSAVI) were performed in just one study each (Table 6).

Relationship between biomes and causes generated by armed conflicts.

In the table of crossed data between the causes generated by armed conflicts and the types of biomes, we found that the utilization of RS was used three times more in the analysis of indirect causes (74%) than in the analysis of direct causes (26%). Regarding direct causes as bombing (10%) (e.g., Burgess et al., 2015; Kwarteng, 1998; Note et al., 2018; Witmer, 2008; van Etten et al., 2008) were studied mainly at the temperate broadleaf forest, dry forest, and semiarid desert biomes. Direct confrontation and military infrastructure (14%) (e.g., Kwarteng, 1998; Suthakar and Bui, 2008; van Etten et al., 2008) were assessed principally at monsoon forest / dry forest and tropical rainforest biomes. On the another hand, in the case of

indirect causes analyzed by RS, we found that forced migration mostly affected biomes (23%) (e.g., Enaruvbe, et al., 2019; Hecht and Saatchi, 2007; Hagenlocher et al., 2012; Leiterer et al., 2018; Lodhi et al., 1998; Suthakar and Bui, 2008), mainly; tropical rainforest, the monsoon forest / dry forest, montane forest, grass savanna, and tree savanna. Other relevant causes studied were agriculture (12%) (Armenteras et al., 2006; Murad and Pearse, 2018; Qamer et al., 2012), illegal crops (10%) (e.g., Armenteras et al., 2013; Murad and Pearse, 2018; Rincón Ruiz et al., 2013), cattle ranching (10%) (e.g., Murad and Pearse, 2018), mining (7%) (e.g., Monroy and Armenteras, 2017; Potapov et al., 2012) and non-forced migration (6%) (e.g., Armenteras et al., 2013), affecting mainly the tropical rainforest followed in decreased order by the montane forest, monsoon forest / dry forest, tree savanna, alpine tundra, and grass savanna (Table 7).

Table 6 Relationship between satellite imagery sensors and imagery classification

	Sensor vs Imagery Classification	NVDI	LULC	FCC	OBIA	MODIS-EVI	MLC	MAD	MSAVI	Total
Very fine (≤1m) and Fine (1 - 10m)	SPOT-5	1	3	3			2			9
	QuickBird II	3	2	2	1	1		1		10
	IKONOS			1	1					2
	WorldView-2	1	2	1						4
	GeoEye			1						1
	ALOS			1						1
	CBERS-2B			1						1
	KVR-1000 (MS)									0
	Rapid Eye			1						1
	Google Earth VHR		2			1				3
Moderate (10–120 m)	Landsat 1-3 MSS		2	3			1			6
	Landsat 4-5 TM	6	11	11			7	1	1	37
	Landsat 6-7 ETM+	7	12	11			5	1		36
	Landsat 8 OLI	1	4	2			3			10
	ASTER		2	3						5
	Sentinel 2			1						1
	IRS-1C LISS-III		1				1			2
Coarse	MODIS	3	2	3		1	1		1	11
	VIIRS									0
	AVHRR						1		1	2
	Total	22	43	45	2	3	21	3	3	**142**

Relationship between biomes and consequences of the armed conflicts

Based on the analysis of the consequences of armed conflicts on the environment with the affected biomes, we found that the use of RS is strongly focused on the analysis of deforestation (46%) (e.g., Armenteras et al., 2006; Gorsevski et al., 2012; Hagenlocher et al., 2012; Murad and Pearse, 2018; Nackoney et al., 2014; Ordway, 2015; Potapov et al., 2012; Rincón Ruiz et al., 2013; Stevens et al., 2011) and on changes of land use and land cover (36%), mainly in the biomes of tropical rainforest, the monsoon forest / dry forest, montane forest, and tree savanna (e.g., Bjorgo, 1999; Enaruvbe, 2019; Murad and Pearse, 2018; Petit et al., 2001; Rincón Ruiz et al., 2013; Sánchez-Cuervo and Aide, 2013). The analysis of abandonment of agricultural lands (8%) (e.g., Gorsevski et al., 2012; Hagenlocher et al., 2012; Witmer, 2008) is noticeable in the biomes of mediterranean vegetation, the monsoon forest / dry forest, dry steppe, and montane forest (Table 8).

DISCUSSION

Concerning the relationship between RS analysis and geographical location of areas affected by armed conflicts, we can infer that the distribution of the RS articles is mainly located near equatorial line in tropical and monsoon forest areas. This is not because, in general, in these areas, there have been more conflicts, since it is not entirely true, indeed many armed conflicts have occurred in temperate, or desert areas such as the Caucasus, the Balkans, Syria, Yemen, Iraq, Turkey, and Afghanistan, where the use of RS to assess the impact on the environment has been considerably less. Comparing Figure 3 to any armed conflict map in the world will show that the pattern is not the same.

We can consider that the high number of investigations that use RS methods in equatorial zones compared to other biomes is mainly due to a set of factors. The reasons that we infer are, the long duration average of conflicts in these areas, the type of armed conflict, many of them guerrilla wars and internal conflicts on a smaller intensity of bombings and direct confrontations, but with a greater generation of displaced persons and fatalities. Furthermore, the fragility and vulnerability of tropical ecosystems and the high forest density makes land-use and land-cover changes and deforestation more evident. As well in the tropical rainforest, there is a considerable number of collateral affectations such as illicit crops, illegal logging and, illegal mining. Additionally, there is a higher presence of population forced to migrate and settle in refugee camps, the limited attention to this population, which in turn generates higher demand for natural resources and greater environmental damage. The difficulty of physically approaching in situ evaluation to these areas makes the use of RS methods more frequently in tropical biomes.

Table 7 Relationship between biomes and causes generated by armed conflict

	Cause vs Biome	Temperate broadleaf forest	Subtropical Rainforest	Mediterranean Vegetation	Monsoon Forest / Dry Forest	Xeric Shrubland	Dry Steppe	Semiarid Desert	Grass Savanna	Tree Savanna	Subtropical dry forest	Tropical Rainforest	Alpine Tundra	Montane Forest	**Total**
Direct	Bombing	4		2	3		1	3				2		1	16
	Direct Confrontation / Militar Infrastructure	1		1	5		1	2	1	2		7	1	2	23
	Landmines			1						1		1		1	4
Indirect	Forced Migration (Camp Refugees)		1	1	6				4	5	2	12	1	5	37
	Non-Forced Migration (Colonization)				2							5		2	9
	Mining				3						1	5		2	11
	Illegal Crops				3	1	1		1	1		4	2	4	17
	Agriculture				3	1	1				1	7	2	5	20
	Cattle Ranching				1	1	1			1	1	5	2	4	16
	Timber				1					1		4		2	8
	Fires											1		1	2
	Total	5	1	5	27	3	5	5	6	11	5	53	8	29	**163**

Table 8 Relationship between biomes and consequences of the armed conflict

Consequence vs Biome	Temperate broadleaf forest	Subtropical Rainforest	Mediterranean Vegetation	Monsoon Forest / Dry Forest	Xeric Shrubland	Dry Steppe	Semiarid Desert	Grass Savanna	Tree Savanna	Subtropical dry forest	Tropical Rainforest	Alpine Tundra	Montane Forest	**Total**
Deforestation	2	1		14	1	2		5	7	2	20	4	11	69
Forestation				1					1				1	3
Desertification / Land Degradation				1				1	1		1		1	5
Land Use / Land Cover Changes	2		2	10	1	2	3	3	4	4	13	3	7	54
Mine Craters	2													2
Militar Infrastructure	1			1					1		2			5
Abandonment of agricultural lands			2	2	1	2			1		1	1	2	12
Groundwater Pollution							1	1						2
Total	7	1	4	29	3	6	4	10	15	6	37	8	22	**152**

We found that 64% of the documents analyzed used more than one sensor as a source of satellite imagery. This is because in many cases; it is required to complement the information required for the analysis, the use of more than one sensor. The main reasons are the gaps in temporal availability, availability of high-resolution images, availability of cloud-free imagery and, the availability of specialized satellite imagery data in a particular sector, especially for multivariate RS analysis.

The most significant findings of the use of satellite imagery sensors are concentrated in the use of moderate resolution sensors (10-120 m). Mainly Landsat 4-5 TM and Landsat 7 ETM+ were the used to study affectations in the biomes of tropical rainforest, montane forest,

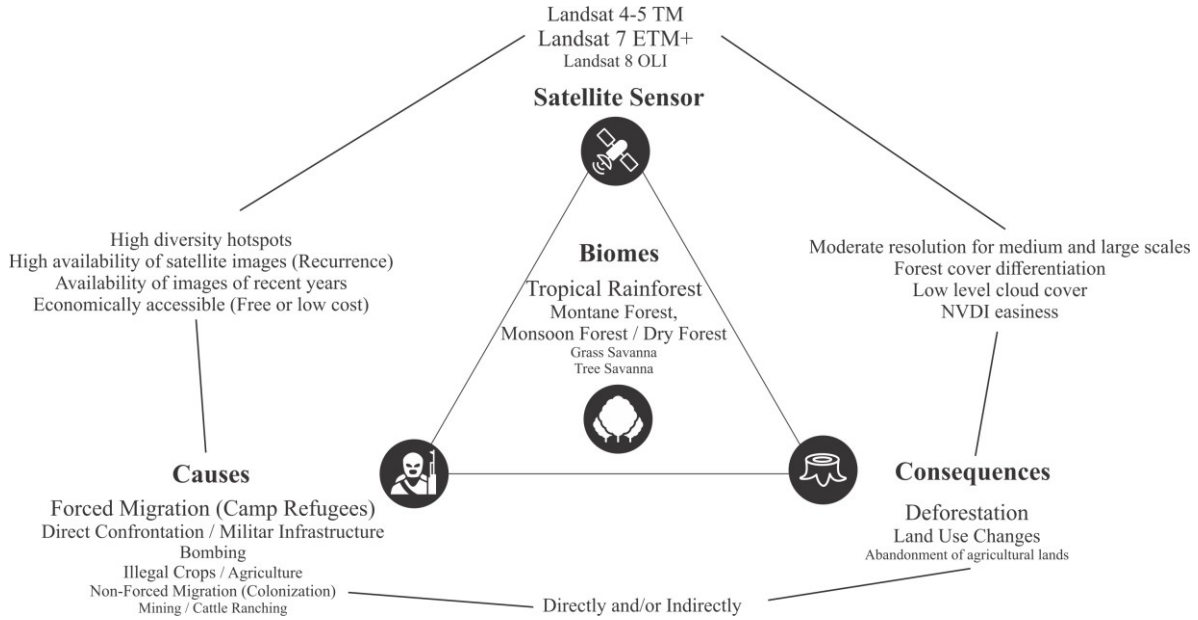

Fig. 6 Relationship between satellite sensor, causes, consequences and biome

monsoon forest/dry forest and to a lesser extent in the biomes of grass savanna and tree savanna. They cover principally the medium-scale (1000-9999 km^2) and the small scale (10,000-99,999 km^2). This is due not only to a single cause but to a set of reasons, such as the higher temporary availability of recurrent and high-quality satellite images. Furthermore, due to the possibility of finding a larger quantity of images with a low level of cloud cover. Another possible cause closely related to the analysis of the consequences is because, for the analysis of vegetation cover of these types of biomes, the size of the scale used does not require a very high level of resolution. Finally, another reason is the ease of acquiring this imagery data set due to the public domain character of these sensors (Fig. 6 and Table 4).

Imagery preprocessing is a mandatory step in the RS analysis. In the case of tropical biomes, the availability of cloud-free cover images is more difficult to acquire because mostly, these biomes present long rainy seasons throughout the year. It means that the use of calibration correctors and haze removals techniques such as TOA, TOC, and ATCOR-2, gain importance as an imperative process, especially in deforestation, land-use, and land cover changes analysis. Nevertheless, just a few studies mentioned explicitly the utilization of which type of preprocessing methods used. Unfortunately, the acquired data is not enough representative to produce significant conclusions.

NDVI can be inferred as the most common method used to classify covers. Mainly because of a series of factors such as high compatibility with several types of satellite sensors (mainly Landsat), the simplicity of the algorithm, and its capacity to distinguish vegetated areas from other surface types. This is especially noticeable in biomes with a large presence of perennial vegetation as the tropical rainforest. NDVI also has the utility of reducing the size of the data to be managed by a factor 2 (or more), since it changes the two spectral bands by a single new.

A relevant finding is a notable relationship between indirect causes and to a lesser extent direct causes with the use of RS in biomes such as tropical rainforests and monsoon forests. Indirect causes such as forced migration generate large refugee camps and to a lesser amount, no-forced migration generates processes of colonization of previously virgin areas and in rare cases, the conflict generates protected lands (forestation). Mining, agriculture, logging, and livestock have also been studied to a certain degree in tropical biomes by RS methods. Direct confrontation and military infrastructure also have a significant but not superlative impact on tropical forests. Illicit crops, forced migration, and agriculture heavily affect mountain forests. The monsoon forest/dry forest has been most affected by military infrastructure, direct confrontation, and bombing. The main cause of the damage to the tree savanna and grass savanna in sub-Saharan Africa is forced migration, generating large refugee camps and changes in land use. Regarding the findings of analyzed consequences in the environment, deforestation and secondly the land-use changes are the most analyzed impacts, mainly in the following high biodiversity biomes; tropical forests, mountain forests, monsoon forest/dry forest, and less studied in tree savanna and grass savanna biomes (Fig. 6).

Some barriers and boundaries that we had during the research were, that despite finding a considerable amount of studies that address the issue of conflict and environment, there is not a very large number of documents that have addressed this problem using RS methods. In those that used RS, it was not easy to identify the type of biome analyzed since they often focus more on country boundaries than on biomes, and these are considered mostly in general rather than

specific. Likewise, biome boundaries are not only different from country boundaries but are much more difficult to delimit since in most cases, there are biological transition zones between one biome and another, which is why it is very common to find that each armed conflict affects more than one type of biome (Uriarte et al., 2010). This is especially noticeable in Colombia, since, due to its particular geographical conditions, in a relatively small area, six different biomes can be differentiated. Some works used RS to assess ecological and wildlife consequences or to identify human populations at risk, but these lines of research are beyond the scope of this analysis and therefore were not considered for this investigation.

We would like to highlight that the scope of this paper is to frame the state of the art on the relationship between armed conflicts, the environment, and their study methods. In order to, from this first step, lay the foundations for more exhaustive research that will allow a better understanding of the complex relationship between armed conflicts and their impact on the environment. This will allow subsequent researches to create more precise and complete methods of evaluation, diagnosis, and possible restoration of the damaged environment. Given the recent and current peace processes, it would be especially interesting to continue tracking deforestation, land-use changes, and other consequences in those countries by adding more data and study parameters. Tracking of year-to-year changes using high-resolution data would be notably useful for correlating specific economic and political conditions with landscape, land use, and deforestation rates and distributions.

CONCLUSION

The observations and results presented here are considered applicable and relevant for the analysis of RS data related to studying the issue between armed conflict and environment, which is not applicable nor considered generally true for armed conflicts itself. The impacts of warfare on environments are diverse and complex; increase mainly deforestation and land-use changes. Over 79% of the RS studies of major armed conflicts between 1980 and 2019 occurred within the torrid area, biomes located near the equatorial line; more than 64% took place directly within high biodiversity hotspot areas. Less than one-third of the 34 recognized hotspots escaped from significant conflict during this period and most suffered repeated episodes of violence. This pattern has been remarkably consistent over these 3 decades.

The most affected studied biome is tropical rainforest; this biome may be found in Southeast Asia, Central Africa, and Amazonia, covering about 12% of Earth's land surface (excluding ice-covered areas such as Antarctica). The largest impact studied using RS in the biomes is deforestation with 45% of the studies, and secondly the land-use change with one-third of the studies. The greatest cause of affectation is indirect causes (70%) such as forced and unforced migration, illicit crops, mining, agriculture, and cattle ranching. This can be explained because migrant populations are larger in these zones, demanding large resources for movement as well as settlement. In the case of Colombia and Afghanistan, illicit crops are a major factor in deforestation and land-use change. Consequences of armed conflicts such as deforestation and land-use change are the most predominant effects in tropical biomes (tropical rainforest, montane forest, monsoon forest/dry forest).

The present research could be useful as a base for future investigations in specific areas in order to analyze armed conflicts and their effect on the landscape. Moreover, it could work as a guideline to make decisions regarding which RS methods and satellite sensors might be used, based on biomes, scales, causes, and consequences. Indeed, the present document provides a background and a starting point that allows for a more extensive analysis of the warfare-environment affair. In the future, we will study the case of the National Parks of Colombia affected by the internal armed conflict, taking as a sample area the "Sumapaz NP".

References

Abuelgasim, A.A., Ross, W.D., Gopal, S., Woodcock, C.E. 1999. Change detection using adaptive fuzzy neural networks: environmental damage assessment after the Gulf War. *Remote Sensing of Environment* 70 (2), 208–223. DOI: 10.1016/s0034-4257(99)00039-5

Al-Khudhairy, D.H.A., Caravaggi, I., Giada, S. 2005. Structural damage assessments from Ikonos data using change detection, object-oriented segmentation, and classification techniques. *Photogrammetric Engineering & Remote Sensing* 71 (7), 825–837. DOI: 10.14358/pers.71.7.825

Álvarez, M.D. 2003. Forests in the time of violence: Conservation implications of the Colombian War. *Journal of Sustainable Forestry* 16 (3-4), 47-68. DOI: 10.1300/J091v16n03_03

Armenteras, D., Rudas, G., Rodriguez, N., Sua, S., Romero, M. 2006. Patterns and causes of deforestation in the Colombian Amazon. *Ecological Indicators* 6 (3), 353–368. DOI: 10.1016/j.ecolind.2005.03.014

Armenteras, D., Cabrera, E., Retana, J., Rodríguez, N. 2013. National and regional determinants of tropical deforestation in Colombia. *Regional Environmental Change* 13 (6), 1181–1193. DOI: 10.1007/s10113-013-0433-7

Bjorgo, E. 1999. Using very high spatial resolution multispectral satellite sensor imagery to monitor refugee camps. *International Journal of Remote Sensing* 21 (3), 611–616. DOI: 10.1080/014311600210786

Biswas, A.K., Tortajada-Quiroz, H.C. 1996. Environmental impacts of the Rwandan refugees on Zaire. *Ambio* 25 (6), 403–408. Online available at: https://www.jstor.org/stable/4314504

Black, R. 1994. Forced migration and environmental change: the impact of refugees on host environments. *Journal of Environmental Management* 42 (3), 261–277. DOI: 10.1006/jema.1994.1072

Blackman, A. 2013. Evaluating forest conservation policies in developing countries using remote sensing data: an introduction and practical guide. *Forest Policy and Economics* 34, 1–16. DOI: 10.1016/j.forpol.2013.04.006

Burgess, R., Miguel, E., Stanton, C. 2015. War and deforestation in Sierra Leone. *Environmental Research Letters* 10 (9) 095014. DOI: 10.1088/1748-9326/10/9/095014

Butsic, V., Baumann, M., Shortland, A., Walker, S., Kuemmerle, T. 2015. Conservation and conflict in the Democratic Republic of Congo: The impacts of warfare, mining, and protected areas on deforestation. *Biological Conservation* 191, 266–273. DOI: 10.1016/j.biocon.2015.06.037

Cabrera, E., Galindo, G., González, J., Vergara, L., Forero, C., Cubillos, A., Espejo, J., Rubiano, J., Corredor, X., Hurtado, L., Vargas D., Duque, A. 2019. Colombian forest monitoring system: Assessing deforestation in an environmental complex country. In: Suratman, M.N. (ed.) Deforestation around the World. IntechOpen, DOI: 10.5772/intechopen.86143

Chadid, M. A., Dávalos, L. M., Molina, J., Armenteras, D. 2015. A Bayesian spatial model highlights distinct dynamics in deforestation from coca and pastures in an Andean biodiversity hotspot. *Forest* 6 (12), 3828–3846. DOI: 10.3390/f6113828

Corson, M. W., Palka, E. J. 2004. Geotechnology, the U.S. Military, and War. In: Brunn, S.D., Cutter, S.L., Harrington J.W. (eds.) Geography and Technology. Springer, Dordrecht, 401–427. DOI: 10.1007/978-1-4020-2353-8_18

Dávalos, L.M. 2001. The San Lucas mountain range in Colombia: how much conservation is owed to the violence? *Biodiversity and Conservation* 10, 69–78. DOI: 10.1023/A:1016651011294

de Merode, E., Smith, K.H., Homewood, K., Pettifor, R., Rowcliffe, M., Cowlishaw, G. 2007. The impact of armed conflict on protected-area efficacy in Central Africa. *Biology Letters* 3 (3), 299–301. DOI: 10.1098/rsbl.2007.0010

Draulans, D., Van Krunkelsven, E. 2002. The impact of war on forest areas in the Democratic Republic of Congo. *Oryx* 36 (1), 35–40. DOI: 10.1017/S0030605302000066

Enaruvbe, G.O., Keculah, K.M., Atedhor, G.O., Osewole, A.O. 2019. Armed conflict and mining induced land-use transition in northern Nimba County, Liberia. *Global Ecology and Conservation* 17, e00597. DOI: 10.1016/j.gecco.2019.e00597

Geist, H.J., Lambin E.F. 2002. Proximate causes and underlying driving forces of tropical deforestation. *Bioscience* 52 (2), 143–150. DOI: 10.1641/0006-3568(2002)052[0143:PCAUDF]2.0.CO;2

Garcia-Corrales, L.M., Avila, H., Gutierrez, R.R. 2019. Land-use and socioeconomic changes related to armed conflicts: A Colombian regional case study. *Environmental Science and Policy* 97, 116–124. DOI: 10.1016/j.envsci.2019.04.012

Gbanie, S.P., Griffin, A.L., Thornton, A. 2018. Impacts on the urban environment: Land cover change trajectories and landscape fragmentation in post-war Western Area, Sierra Leone. *Remote Sensing* 10 (1), 129. DOI: 10.3390/rs10010129

Gheyle, W., Stichelbaut, B., Saey, T., Note, N., Van den Berghe, H., Van Eetvelded, V., Van Meirvenne, M., Bourgeois, J. 2018. Scratching the surface of war. Airborne laser scans of the Great War conflict landscape in Flanders. *Applied Geography* 90, 55–68. DOI: 10.1016/j.apgeog.2017.11.011

Michael Ezequiel Gómez-Rodríguez, M.E., Molina-Pérez, F.J., Agudelo-Echavarría, D.M., Cañón-Barriga, J.E., Vélez-Macías, F. de J. 2017. Changes in soil cover in Nechí, Antioquia: An approach to the environmental impact of mining, 1986-2010. *Revista Facultad de Ingeniería* 26 (45), 149–163. DOI: 10.19053/01211129.v26.n45.2017.6423

Gorsevski, V., Kasischke, E., Dempewolf, J., Loboda, T., Grossmann, F. 2012. Analysis of the impacts of armed conflict on the Eastern Afromontane forest region on the South Sudan - Uganda border using multitemporal Landsat imagery. *Remote Sensing of Environment* 118, 10–20. DOI: 10.1016/j.rse.2011.10.023

Gorsevski, V., Geores, M., Kasischke, E. 2013. Human dimensions of land use and land cover change related to civil unrest in the Imatong Mountains of South Sudan. *Applied Geography* 38, 64–75. DOI: 10.1016/j.apgeog.2012.11.019

Hagenlocher, M., Lang, S., Tiede, D. 2012. Integrated assessment of the environmental impact of an IDP camp in Sudan based on very high resolution multi-temporal satellite imagery. *Remote Sensing of Environment* 126, 27–38. DOI: 10.1016/j.rse.2012.08.010

Hanson, T., Brooks, T.M., Da Fonseca, G.A.B., Hoffmann, M., Lamoreux, J.F., Machlis, G., Mittermeier, C.G., Mittermeier, R.A., Pilgrim, J.D. 2008. Warfare in Biodiversity Hotspots. *Conservation Biology* 23 (3), 578–587. DOI: 10.1111/j.1523-1739.2009.01166.x

Hecht, S.B., Saatchi, S.S. 2007. Globalization and forest resurgence: Changes in forest cover in El Salvador. *Bioscience* 57 (8), 663–672. DOI: 10.1641/B570806

Hoffmann, C., García-Márquez, J.R., Krueger, T. 2018. A local perspective on drivers and measures to slow deforestation in the Andean-Amazonian foothills of Colombia. *Land Use Policy* 77, 379–391. DOI: 10.1016/j.landusepol.2018.04.043

International Law and Policy Institute - ILPI. 2014. Protection of the natural environment in armed conflict. Oslo. 68p. Online available at: https://ceobs.org/wp-content/uploads/2018/03/Protection-of-the-Natural-Environment-in-Armed-Conflict.pdf

Ingalls, M.L., Mansfield, D. 2017. Resilience at the periphery: Insurgency, agency and social-ecological change under armed conflict. *Geoforum* 84, 126–137. DOI: 10.1016/j.geoforum.2017.06.012

Jarrett, R. 2003. The environment: Collateral victim and tool of war. *BioScience* 53 (9), 880–882. DOI: 10.1641/0006-3568(2003)053[0880:TECVAT]2.0.CO;2

Jha, U., 2014. Armed Conflict and Environmental Damage. Vij Books India Pvt Ltd.

Kwarteng, A.Y. 1998. Multitemporal remote sensing data analysis of Kuwait's oil lakes. *Environment International* 24 (1-2), 121–137. DOI: 10.1016/s0160-4120(97)00129-3

Landholm, D.M., Pradhana, P., Kroppa, J.P. 2019. Diverging forest land use dynamics induced by armed conflict across the Tropics. *Global Environmental Change* 56, 86–94. DOI: 10.1016/j.gloenvcha.2019.03.006

Le Billon, P. 2001. The political ecology of war: natural resources and armed conflicts. *Political Geography* 20 (5), 561–584. DOI: 10.1016/s0962-6298(01)00015-4

Leiterer, R., Bloesch, U., Wulfa, H., Eugster, S., Joerg, P, C. 2018. Vegetation monitoring in refugee-hosting areas in South Sudan. *Applied Geography* 93, 1-15. DOI: 10.1016/j.apgeog.2018.01.013

Levin, N., Ali, S., Crandall, D. 2018. Utilizing remote sensing and big data to quantify conflict intensity: The Arab Spring as a case study. *Applied Geography* 94, 1–17. DOI: 10.1016/j.apgeog.2018.03.001

Lodhi, M.A., Echavarria, F.R., Keithley, C. 1998. Using remote sensing data to monitor land cover changes near Afghan refugee camps in northern Pakistan. *Geocarto International* 13 (1), 33–39. DOI: 10.1080/10106049809354626

Loucks, C., Mascia, M.B., Maxwell, A., Huy, K., Duong, K., Chea, N., Long, B., Cox, N., Seng, T. 2009. Wildlife decline in Cambodia, 1953–2005: exploring the legacy of armed conflict. *Conservation Letters* 2 (2), 82–92. DOI: 10.1111/j.1755-263X.2008.00044.x

Machlis, G.E., Hanson, T. 2008. Warfare ecology. *Bioscience* 58 (8), 729–736. DOI: 10.1641/B580809

Mendez, F., Valánszki, I. 2019. Trends in the use of remote sensing methods for the analysis of areas affected by armed conflicts. *SZIEntific Meeting for Young Researchers - Ifjú Tehetségek Találkozója*, 173–192.

McNeely, J. 2003. Conserving forest biodiversity in times of violent conflict. *Oryx* 37 (2), 142–152. DOI: 10.1017/S0030605303000334

Monroy, D., Armenteras, D. 2017. Land cover change caused by alluvial mining on the Nechí River, Antioquia (Colombia). *Gestión y Ambiente* 20 (1), 50–61. DOI: 10.15446/ga.v20n1.61513

Murad, C.A., Pearse, J. 2018. Landsat study of deforestation in the Amazon region of Colombia: Departments of Caquetá and Putumayo. *Remote Sensing Applications: Society and Environment* 11, 161–171. DOI: 10.1016/j.rsase.2018.07.003

Nackoney, J., Molinario, G., Potapov, P., Turubanova, S., Hansen, M., Furuichi, T. 2014. Impacts of civil conflict on primary forest habitat in northern Democratic Republic of the Congo, 1990–2010. *Biological Conservation* 170, 321–328. DOI: 10.1016/j.biocon.2013.12.033

Negret P.J., Sonter, L., Watson, J.E.M., Possingham, H.P., Jones K.R., Suarez, C., Ochoa-Quintero, J.M., Maron, M. 2019. Emerging evidence that armed conflict and coca cultivation influence deforestation patterns. *Biological Conservation* 239, 108176. DOI: 10.1016/j.biocon.2019.07.021

Note, N., Gheyle. W., Van den Berghe, H., Saey, T., Bourgeois, J., Van Eetvelde, V., Van Meirvenne, M., Stichelbaut, B. 2018. A new evaluation approach of World War One's devastated front zone: A shell hole density map based on historical aerial photographs and validated by electromagnetic induction field measurements to link the metal shrapnel phenomenon. *Geoderma* 310, 257–269. DOI: 10.1016/j.geoderma.2017.09.029

Omar S.A.S., Bath, N.R. 2009. Critical assessment of the environmental consequences of the invasion of Kuwait, the Gulf War, and the aftermath. In: Kassim T.A., Barceló D. (eds) Environmental Consequences of War and Aftermath. The Handbook of Environmental Chemistry, vol 3U. Springer, Berlin, Heidelberg, 141–170. DOI: 10.1007/978-3-540-87963-3_5

Ordway, E. M. 2015. Political shifts and changing forests: Effects of armed conflict on forest conservation in Rwanda. *Global Ecology and Conservation* 3, 448–460. DOI: 10.1016/j.gecco.2015.01.013

Partow, H. 2008. Environmental impact of wars and conflicts. In: Tolba, M.K., Saab, N.W. (eds.) Arab environment: Future challenges. Arab Forum for Environment and Development, 159–172. Online available at: http://www.fao.org/fileadmin/user_upload/rome2007/docs/Arab_Environment_Future_Challenges.pdf

Pech, L., Lakes, T. 2017. The impact of armed conflict and forced migration on urban expansion in Goma: Introduction to a simple method of satellite-imagery analysis as a complement to field research. *Applied Geography* 88, 161–173. DOI: 10.1016/j.apgeog.2017.07.008

Petit, C., Scudder, T., Lambin, E. 2001. Quantifying processes of land-cover change by remote sensing: Resettlement and rapid land-cover changes in southeastern Zambia. *International Journal. Remote Sensing* 22 (17), 3435–3456. DOI: 10.1080/01431160010006881

Potapov, P.V., Turubanova, S. A., Hansen, M. C., Adusei, B., Broich, M., Altstatt, A., Mane, L., Justice, C.O. 2012. Quantifying forest cover loss in Democratic Republic of the Congo, 2000–2010, with Landsat ETM+ data. *Remote Sensing of Environment* 122, 106–116. DOI: 10.1016/j.rse.2011.08.027

Qamer, F.M., Abbas, S., Saleem, R. Shehzad, K., Ali, H., Gilani, H. 2012. Forest cover change assessment in conflict-affected areas of northwest Pakistan: the case of Swat and Shangla Districts. *Journal of Mountain Science* 9 (3), 297–306. DOI: 10.1007/s11629-009-2319-1

Rincón Ruiz, A., Pascual, U., Romero, M. 2013. An exploratory spatial analysis of illegal coca cultivation in Colombia using local indicators of spatial association and socioecological variables. *Ecological Indicators* 34, 103–112. DOI: 10.1016/j.ecolind.2013.04.008

Rustad, S.C.A., Rød, J.K., Larsen, W., Gleditsch, N.P. 2008. Foliage and fighting: forest resources and the onset, duration, and location of civil war. *Political Geography* 27 (7), 761–782. DOI: 10.1016/j.polgeo.2008.09.004

Sánchez-Cuervo, A.N., Aide, T.M. 2013. Consequences of the armed conflict, forced human displacement, and land abandonment on forest cover change in Colombia: A multi-scaled analysis. *Ecosystems* 16 (6), 1052–1070. DOI: 10.1007/s10021-013-9667-y

Sigismond A., Wilson, S.A., Wilson, C.O. 2013. Modelling the impacts of civil war on land use and land cover change within Kono District, Sierra Leone: a socio-geospatial approach. *Geocarto International* 28 (6), 476–501. DOI: 10.1080/10106049.2012.724456

Solomon, N., Birhane, E., Gordon, C., Haile, M., Taheri, F., Azadie, H., Scheffran, J. 2018. Environmental impacts and causes of conflict in the Horn of Africa: A review. *Earth-Science Reviews* 177, 284–290. DOI: 10.1016/j.earscirev.2017.11.016

Sosnowski, A., Ghoneim, E., Burke, J.J., Hines, E., Halls, J. 2016. Remote regions, remote data: A spatial investigation of precipitation, dynamic land covers, and conflict in the Sudd wetland of South Sudan. *Applied Geography* 69, 51–64. DOI: 10.1016/j.apgeog.2016.02.007

Stevens, K., Campbell, L., Urquhart, G., Kramer, D., Qi, J. 2011. Examining complexities of forest cover change during armed conflict on Nicaragua's Atlantic Coast. *Biodiversity and Conservation* 20 (12), 2597–2613. DOI: 10.1007/s10531-011-0093-1

Stichelbaut, B., Gheyle, W., Saey, T., van Eetvelde, V., van Meirvenne, M., Note, N., van den Berghe, H., Bourgeois, J. 2016. The First World War from above and below. Historical aerial photographs and mine craters in the Ypres Salient. *Applied Geography* 66, 64–72. DOI: 10.1016/j.apgeog.2015.11.020

Suthakar, K., Bui, E.N. 2008. Land use/cover changes in the war-ravaged Jaffna Peninsula, Sri Lanka, 1984–early 2004. *Singapore Journal of Tropical Geography* 29 (2), 205–220. DOI: 10.1111/j.1467-9493.2008.00329.x

Tian, Y., Wu, B., Zhang, L., Li, Q., Jia, K., Wen, M. 2011. Opium poppy monitoring with remote sensing in North Myanmar. *International Journal of Drug Policy* 22 (4), 278–284. DOI: 10.1016/j.drugpo.2011.02.001

Uriarte, M., Schneider, L., Rudel, T.K., 2010. Land transitions in the tropics: going beyond the case studies. *Biotropica* 42 (1), 1–2. DOI: 10.1111/j.1744-7429.2009.00580.x

van der Meer, F., van der Werff, H., Jong, S.M. 2009. Pre-Processing of optical imagery in Warner, T.A., Nellis, M.D., Foody, G.M. (eds.) The SAGE Handbook of Remote Sensing. 55 City Road, London: SAGE Publications, Inc. DOI: 10.4135/9780857021052.n16

van Etten, J., Jongerden, J., de Vos, H.J., Klaasse, A., van Hoeve E.C.E. 2008. Environmental destruction as a counterinsurgency strategy in the Kurdistan region of Turkey. *Geoforum* 39 (5), 1786–1797. DOI: 10.1016/j.geoforum.2008.05.001

Witmer, F.D.W. 2008. Detecting war-induced abandoned agricultural land in northeast Bosnia using multispectral, multitemporal Landsat TM imagery. *International Journal of Remote Sensing* 29 (13), 3805–3831. DOI: 10.1080/01431160801891879

Witmer, F.D.W. 2015. Remote sensing of violent conflict: eyes from above. *International Journal of Remote Sensing* 36 (9), 2326–2352. DOI: 10.1080/01431161.2015.1035412

sciendo

Journal of Environmental Geography 13 (3–4), 15–26.

DOI: 10.2478/jengeo-2020-0008
ISSN 2060-467X

APPLYING AUTOMATIC MAPPING PROCESSING BY GMT TO BATHYMETRIC AND GEOPHYSICAL DATA: CASCADIA SUBDUCTION ZONE, PACIFIC OCEAN

Polina Lemenkova[1]*

[1]Schmidt Institute of Physics of the Earth, Russian Academy of Sciences.
Laboratory of Regional Geophysics and Natural Disasters (Nr. 303).
Bolshaya Gruzinskaya St., 10, Bld. 1, Moscow, 123995, Russian Federation.
Tel.: +7-916-298-37-19 ORCiD ID: 0000-0002-5759-1089
*Corresponding author, e-mail: pauline.lemenkova@gmail.com

Research article, received 17 July 2020, accepted 30 September 2020

Abstract

The Cascadia Trench is stretching along the convergent plate boundaries of Pacific Plate, North America Plate and Juan De Fuca Plate. It is an important geomorphological structural feature in the north-east Pacific Ocean. The aim of the paper is to analyse the geomorphology of the Cascadia Trench west of Vancouver Island (Canada and USA) using the GMT cartographic scripting toolset. The unique geomorphological feature of the Cascadia Trench is that the thick sediment layer completely obscures the subduction zone and abyssal hills. This results in the asymmetric profile in the cross-section of the trench. Bathymetric data were extracted from the GEBCO 2019 dataset (15 arc-second grid), sediment thickness by the GlobSed dataset. Due to the dominance of high sedimentary rate and complexity of the tectonic processes and geologic settings, Cascadia Trench develops very specific asymmetric geomorphic shape comparing to the typical V-form. The results of the geomorphic modelling show that eastern side of the trench has a gentle curvature (slope: 35.12°), partially stepped, due to the tectonic movements and faults. The opposite, oceanward side is almost completely leveled. The trench is narrow with maximal depth at the selected segment -3489 m and for the whole dataset -6201 m. The most repetitive depth is in a range -2500 to -2400 m (267 samples) and -2500 to -2600 m (261 samples). The bottom is mostly flat due to the high sedimentation rates indicating the accumulative leveling processes. Marine free-air gravity anomalies along the Cascadia Subduction Zone are characterized by weakly positive values (20 mGal) increasing rapidly in the zone of the continental slope (>200 mGal), which is associated with a decrease in thickness of the Earth's crust.

Keywords: GMT, Cascadia Trench, Cascadia Subduction Zone, Pacific Ocean, Cartography, Geomorphology

INTRODUCTION

Deep-sea trenches, or oceanic trenches are important geomorphological structures of the oceanic seafloor, and typically associated with zones of tectonic plates subduction. The genesis of the geomorphological landforms of the submarine relief in oceanic trenches is closely related to the origin and development of the oceans which is, one of the most difficult issues of geology and geomorphology. Trenches are formed in the subduction zones, where one tectonic plate moves under another, as a morphological expression of the inclined seismic focal planes along which the plane moves. There are various publications focusing on trench geomorphology and various aspects regarding ocean seafloor geology: slab fragmentation (Long, 2016), plate-boundary earthquakes (Hutchinson and Clague, 2017), seismic properties of the subducted slabs (Flueh et al., 1998), factors affecting trench topography and geomorphology (Lemenkova, 2018, 2019d), relations with climate (Kuhn et al., 2006), synthesis of geophysical characteristics (Agostinetti and Miller, 2014), correlation of slab anomalies with plate locking and slab dip (Bodmer et al., 2020), fluid release from the slabs (Evans et al., 2014), to mention a few. The complexity of the submarine geomorphology of the oceanic trenches indicates a need for a modelling by advanced cartographic methods of data analysis. Furthermore, it requires a detailed cartographic mapping of the geomorphology of the oceanic trenches supported by the longitudinal profiles based on the median depth of cross-sections. The visualization of the multi-source datasets (e.g. geology, sedimentation, tectonics) enables a better understanding of the trench development and formation. As a response of such objectives, this paper presents a systematic visualization of the digital data on the Cascadia subduction zone with a focus on the selected segment located westwards of the Vancouver Island, Canada and USA.

The study aims to present a novel method of the cartographic modelling by automated mapping using Generic Mapping Tools (GMT) with a case study of Cascadia Trench. Scripting approach provided by GMT enables to combine a number of thematic raster grids and visualize layers using selected code lines of a GMT syntax (Wessel and Smith, 1991). In contrast with traditionally used GIS, such a collection of codes is repetitive as shell scripts, and it can be reused for automatization of geological mapping. The data analysis was supported by the longitudinal profiles edited based on the median depth of cross-sectional profiles, visualization of the geological

and tectonic settings, sediment thickness and geophysical datasets. The application of shell scripts in cartographic visualization and numerical modelling, in contrast to plotting maps GUI in a traditional GIS, provides advantages in editing and data analysis due to their repeatability and automatization. Compared to the classic GIS, shell scripting of GMT presents a novel approach in cartographic machine learning through visualizing of the large geologic datasets in a rapid and effective way. In this sense, this paper is focused on the contribution to the development of the cartographic methods in environmental geology with a case study of Cascadia Trench through a complex analysis of the raster datasets overlaid with vector geologic maps.

This manuscript presents details of a special geomorphological situation of the Cascadia Trench which contrasts from other trenches because of its sediment-filled structure. The research combines information on geomorphological, geological (including sedimentology) and geophysical maps and datasets. The focus of this works is to demonstrate the geomorphological analysis based on the available data using presented maps plotted in GMT. Based on high-resolution data analysis (GEBCO DEM, GlobSed and EGM-2008) processed by the GMT, the paper first analyses regional geological settings of the study area around Oregon, Washington and British Columbia states (USA and Canada) and then presents a geometric modelling of the trench as a function of sediment deposition, tectonic activities and dynamics and coastal environmental processes. The topographic data across the trench segment were collected through automatic digitizing of the trench segment and compared regarding the frequency of data distribution. In a comparative study of geological properties of the Cascadia Subduction Zone reflected in topographic patterns, the paper aims to visualize the structure of the Cascadia Trench using scripting cartographic methods (a sequence of the GMT codes and modules) and geospatial datasets derived from open sources. A study is based on using digital datasets, literature sources, information on coastal environmental settings in the Vancouver Island area, and methods of the geomorphological modelling of the Cascadia Trench.

STUDY AREA

The study area is geographically located in the area of the Cascadia Trench (Cascadia Subduction Zone), along the western coast of Canada off Vancouver Island and the USA, Oregon and California States (Fig. 1). The exact corner coordinates (lower left – upper right) of the larger study area are 136°W 35°N – 120°W 55°N and those of the smaller study area with trench segment are 132°W 47°N – 122°W 52°N (Fig. 1). The depths on the shelf vary between 100 and 200 m (Fig. 1). The seafloor surface is complicated as a result of structural uplifts and ridges. The shelf is relatively narrow along the west coast of the California Peninsula. Its leveled surface is dissected by the individual submarine valleys. The depths of the oceanward edge of the shelf are generally smaller than 100 m.

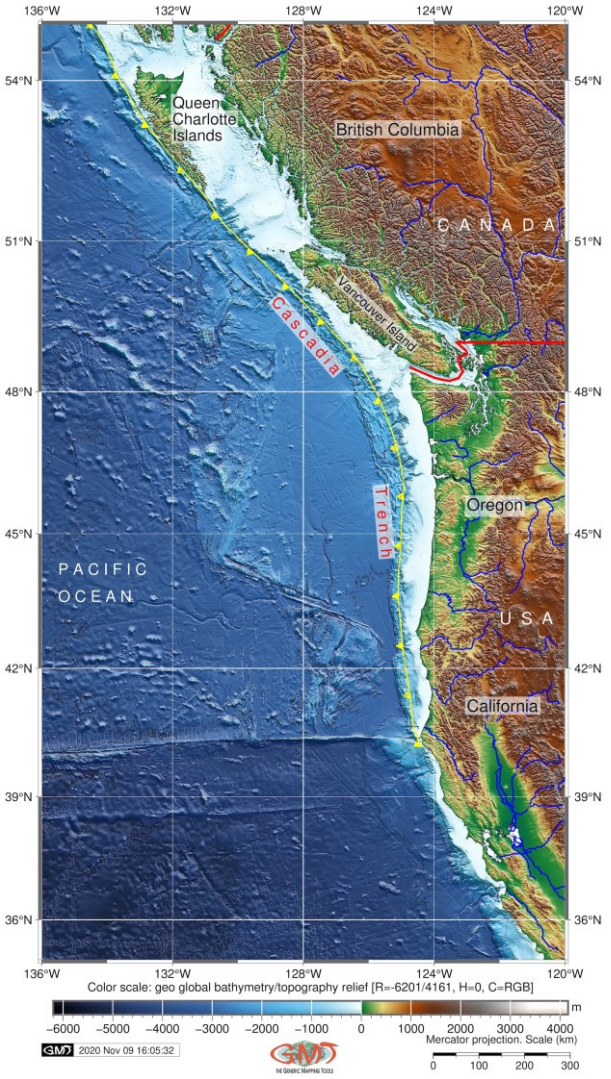

Fig. 1 Topographic map of the Cascadia Subduction Zone, Pacific Ocean. Dataset: GEBCO Compilation Group (2020)

The glacial shelf with typical longitudinal and transverse grooves, banks and shallow areas extends along the coasts of Vancouver Island, Canada. Depths on banks are <150 m, in depressions reaching 250-300 m (Fig. 1).

Geologic settings of the Cascadia Trench are formed in the condition of the tectonic plates subduction and presence of three tectonic plates: Pacific Plate, Juan De Fuca Plate and North American Plate (Fig. 2). The Cascadia Subduction Zone stretches above the almost sub-parallel stretching Mendocino Escarpment (40°N) Murray Fracture Zone, offshore Oregon and British Columbia (USA and Canada, respectively) with localized submarine fan complexes and not developed continental rise (Atwater et al., 2014). The shelf and continental slope in the Gulf of California and northern end of the East Pacific Rise are formed by the submerged flanks of the folded geologic structures, framed by faults descending to the bottom of the gulf. The continental slope along the Cascadia Subduction Zone has a simple structure, represented by a stepped ledge, with the depths at foot around 3000-3500 m. It is, however, made complicated by the

block ledges and ridges in the areas of Mendocino Escarpment (Fig. 2) and by the northern part of Vancouver Island, Gorda Ridge and Bianco Fracture Zone. The most seismically active part of the Cascadia Subduction Zone, the Mendocino Triple Junction region, was described with regards to the mechanism of plates rotation indicating its complex formation (Li et al., 2018).

The crust in the Gorda and Juan de Fuca ridges is typical for the oceanic rift zones. The basaltic layer is thinned with mantle surface rises with the velocity of the boundary waves decreasing to 7.2–7.5 km/s. A triple junction point existed at the end of the Miocene north of the Mendocino Fracture Zone. Gorda and Juan de Fuca ridges appeared along the new axis of the extension which appeared to the west of the North America continent. Therefore, North American Plate began to move behind the Pacific Plate with a general NW direction. Landslides often occur in the mountainous areas of Canada where specific lithological, topographic and geomorphological conditions (e.g. slope angle, curvature, aspect) create favorable conditions for mass movements. These processes contribute to the sedimentation of the Cascadia region by debris flow (Perkins et al., 2018; Lemenkova et al., 2012). The potential development of land sliding mirrors is related to the combined effects of tectonics, geomorphology and lithology. For instance, lithological and structural variations often lead to a difference in variations in permeability of rocks minerals (Guzzetti et al., 1996). Geomorphological factors causing landslides include slope steepness, angle and aspect. Besides, local earthquakes can be another triggering geologic factor of landslides, debris flow and sheet erosion (Penserini et al., 2017).

The Cascadia Subduction Zone developed as a consequence of several types of active tectonic processes: (i) tectonic plate convergence of the minor tectonic plates (Explorer, Juan de Fuca and Gorda) are moving in E direction below the major North American Plate; (ii) the North American Plate subducting in a SW direction, sliding over the minor plates and Pacific Plate; (iii) a complexity of the tectonic processes: accretion, subduction, deep earthquakes and active volcanism (including eruptions) of the Cascades; (iv) active sedimentation processes that deformed the geomorphic shape of the trench and buried it with sediment layer. More detailed studies on the local areas of the Cascadia Subduction Zone formation have been carried out by Greene et al. (2018) who presented mapping of the Skipjack Island fault zone near the Vancouver Island using multi-beam echo-sounder bathymetry, seismic reflection profiles, and sediment cores.

The rift zone of North America crosses the western region of the USA and continues in the ocean seafloor in the Mendocino Escarpment. The sinistral strike-slip zone stretching from the continent to the ocean seafloor reaches 1100 km.

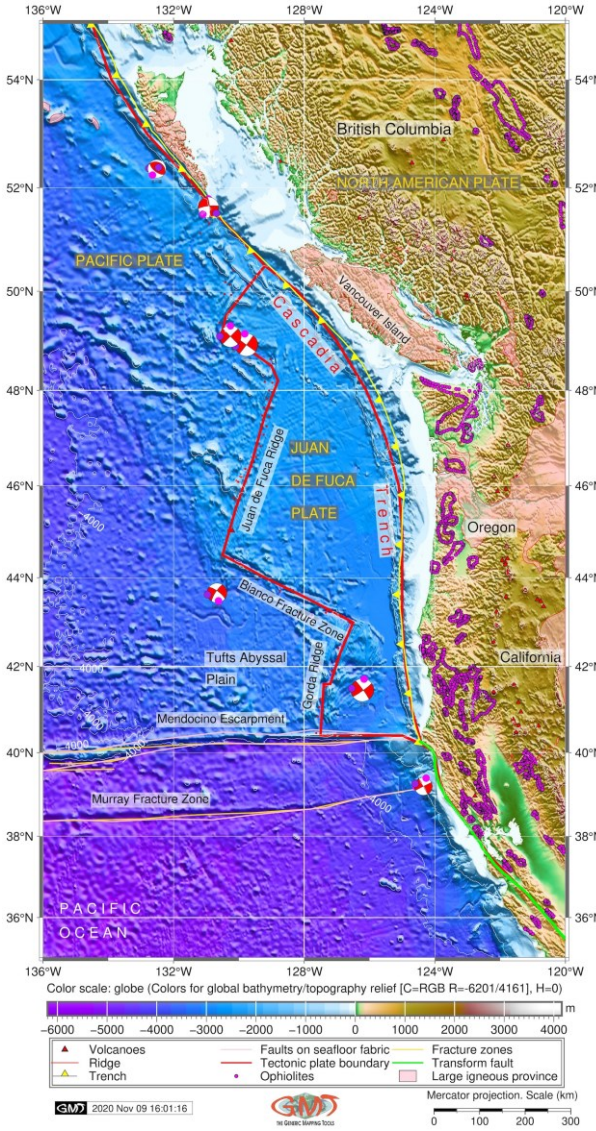

Fig. 2 Geologic map of the Cascadia Subduction Zone. Dataset: ETOPO1 global terrain model (Amante and Eakins, 2009)

The main morpho-structure of the Pacific Ocean, the East Pacific Rise, is stretching in NE direction, approaching North America continent where it enters Gulf of California and continues its structure on the land. However, northward of 40°N its small branches – Gorda Ridge and Juan de Fuca Ridge appear again off Cascadia Fracture Zone (Fig. 2). The short Gorda Ridge extends in an almost submeridional direction from the Mendocino Fracture Zone, which is transected by the Blanco Fracture Zone (Transform Fault Zone) at 43°N, where rift structures are displaced to the NW by ca. 350 km. The Juan de Fuca Ridge is stretching further northwards, reaching continental slope near Vancouver. Deep rift valleys bordered by a series of the rift ridges exist almost everywhere along the axis of these main ridges. The depths in the rift valley of the Gorda Ridge exceed 3000 m, above the ridges – from 1500 to 2500 m, on the Juan de Fuca Ridge – ca. 2800 and 2000 m.

According to the present shape of the deep-sea trenches, they can be discriminated as sediment starved, partly sediment filled, and sediment flooded trenches (Geersen et al., 2018). Most of the sediment starved trenches show tectonic signature well preserved in the trench: outer slope, the depression, and the inner slope. The Cascadia Trench is a sediment flooded trench with relief hidden by a thick layer of sediment. Depending on the sediment rates and filling, trenches may turn into sediment filled such as Cascadia Trench, where the outer slope and the trench axis correspond to a flat seafloor. Such processes are caused by the consequent deposition of thick sediments layers that levels topographic shapes and forms. Submarine sediment geomorphology is strongly controlled by slope, depending on location along the continental margin.

Oceanic sediments deposited on continental margins consist mainly of erosion products of the nearby exposed continental areas, associated with transport and sedimentary processes (Carpentier et al., 2014). The distribution of the submarine sediments in a general approximation reflects fluvial morphology similar to alluvial meandering rivers. For instance, geometry correlates with the location along continental margins, by analogous to alluvial meandering rivers, and with slope similarly to rivers. An important distribution pattern of has been found for the ultrafine sediment particles (size < 38 μm) located in inner Washington shelf to the central Cascadia Basin (Coppola et al., 2007) with deposition increasing further away from the coast. This suggest that various types of sediment are distributed not equally and the coarser sediments are preferably deposited along the coasts.

Since the Cascadia Trench is a sediment filled trench, it has high values of sediment thickness (Fig. 3), in contrast to the sediment starved trenches, for example west of the coasts of Peru and Chile. Sediment input in the Cascadia Trench seafloor region is originated by the sediments of fluvial and glacial origin. Sediments are delivered to the shelf edge during sea level low periods and then transported to the trench by a network of submarine canyons (Geersen et al., 2018). As a result, the submarine fans filled the trench depression completely and also leveled out local bathymetry on the oceanic plate around the trench. As a consequence, the only geomorphological feature is presented by submarine channels instead of seamounts, bend-faults and other seafloor spreading fabric. Influx of sediment from land and the continental slope is an important parameter that controls the absolute depth of the Cascadia Trench.

METHODS AND MATERIALS

The presented research was based on using the Generic Mapping Tools (GMT) cartographic scripting toolset (Wessel et al., 2013). In contrast to existing GIS software, such as ArcGIS (Suetova et al., 2005a, 2005b; Lemenkova, 2011; Klaučo et al., 2013, 2014), the GMT proposes automatization of the cartographic routine through scripting. This enables automatic derivation of the multi-scaled maps from a shell script.

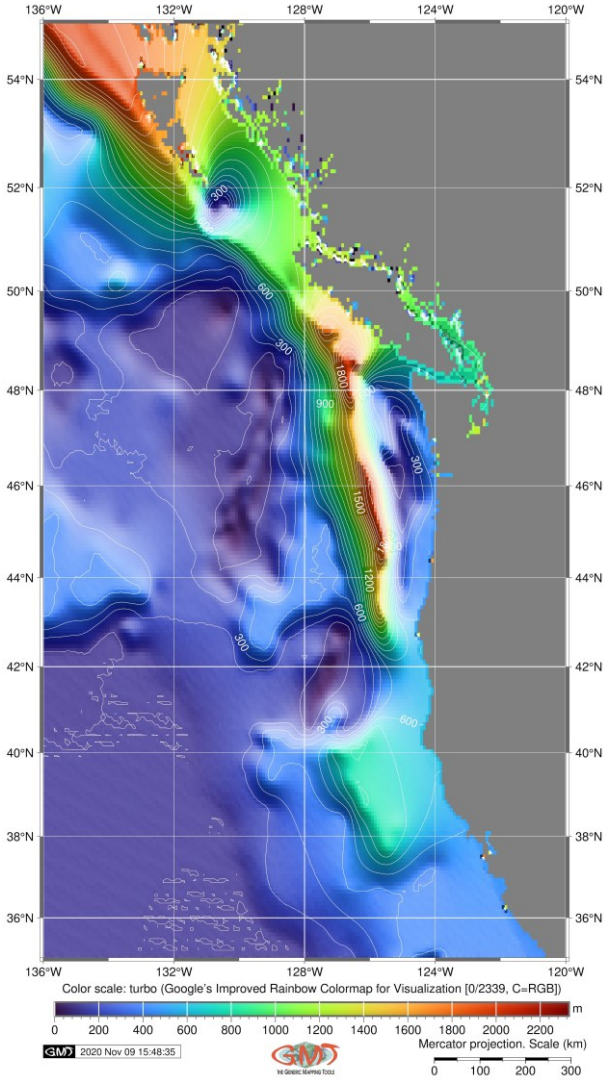

Fig. 3 Sediment thickness of the Cascadia Subduction Zone. Dataset: Straume et al. (2019)

The thematic maps include visualized geologic, topographic and tectonic settings, geoid model and geophysical grid of the satellite derived free-air gravity approximation showing marine free-air gravity anomalies over the study area. Automatization in cartography has until recent times focused mainly on developing specific computer-assisted algorithms to present the machine learning solutions in the cartographic techniques (e.g. Gauger et al., 2007; Schenke and Lemenkova, 2008). GMT presents further steps in cartographic techniques through a console based mapping. Rather than plotting maps by hand from GUI, GMT enables a fast execution of the shell script with a resulting map automatically plotted by the machine using user-defined parameters described in a script.

GMT scripting toolset significantly increases three important factors of the cartographic methodology: i) speed of work; ii) precision of plotting; iii) aesthetic beauty of maps. Using scripts in cartographic plotting enables to quickly check the effects of the maps and, depending on the evaluation, to adjust the image of the map (grids, location of

annotations, ticks, etc.). Moreover, since the GMT significantly automates the process of mapping, it enables to keep on learning about the depicted geological phenomenon rather than technical questions of plotting: whether the correct layer sequence has been transferred, the most relevant geologic and tectonic settings, the marine free-air gravity and geoid have been visualized, and the most recent high-resolution datasets have been selected. Therefore, using GMT enables the cartographic representation to be a more cognitive rather than a technical process and to get to the essence of a geophysical and tectonic phenomenon besides its adequate visualization as a series of printer-quality maps. Through the machine based cartographic plotting, GMT aims for the elimination of various errors arising from various sources of the hand-made cartographic routine often prone to mistakes. Hence, through the increased precision of maps by means of the console-based graphic plotting, GMT-based maps help to highlight the correlations between the geological phenomena leading to the correct conclusions.

The topographic base map (Fig. 1) presents geographic phenomena (e.g. rivers, political borders, coastal lines) gathered from the GMT embedded layers accessed through module 'pscoast' as individual cartographic elements. The rivers were strongly generalized to present a general overview of the Canadian and the USA river network, so as to distract from the topographic content of the map theme as little as possible. The geoid raster grid used for this study (geoid.egm96.grd) is based on the National Geospatial-Intelligence Agency (NGA)/NASA Geoid Height File (Lemoine et al., 1998). A geopotential model of the Earth's gravity fields (EGM-2008) is set up as a 2.5-minute grid of xyz values in the tide-free system (Pavlis et al., 2012) which is an updated version of the EGM96 Geopotential Model (a 15-minute resolution grid). The EGM-2008 dataset is a base raster dataset for modelling geoid (Fig. 4). The interpolation of the geoid undulations from the 15'x15' (15 arc-minute) resolution was done using GMT module 'grdimage' by code 'gmt grdimage ct_geoid.nc -Ccolors.cpt -R224/240/35/55 -JM6i -P -I+a15+ne0.75 -Xc -K > $ps'. The spatial resolution of the geopotential models (e.g. EGM296) depends on the availability of the high-quality raster gravity data. The contour isolines on the geoid undulation grid file were then visualized by 'grdcontour' module using code 'gmt grdcontour ct_geoid.nc -R -J -C1 -A5 -Wthinnest,dimgray -O -K >> $ps'.

The geologic map was plotted as an overlay of the base map consisting of boundaries and coastlines and a GEBCO grid and tectonics (transform fault lines, lines of plate boundaries, ridge, trench and fracture zones, spots of volcanoes and ophiolites, polygon distribution of large igneous provinces or LIPs) in the Cascadia Trench. Such a presentation is based on the combination of thematic data by using several GMT modules and a schematic legend color of the base map (Fig. 2). The main modules of GMT include 'psxy', 'pscoast', 'psbasemap', 'pslegend'. Their functionality is

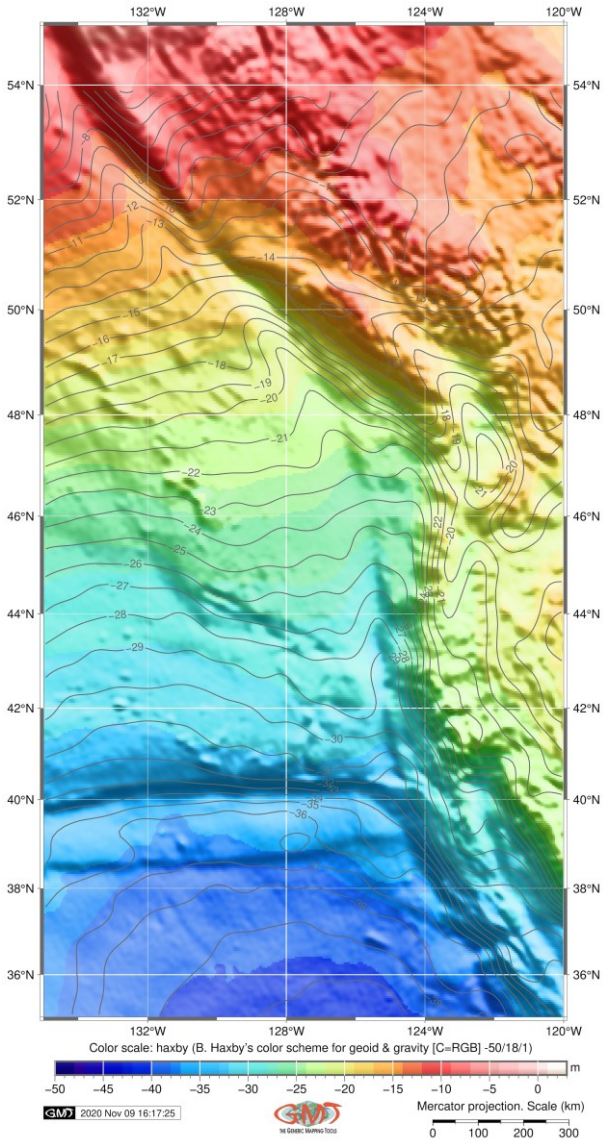

Fig. 4 Geoid model of the Cascadia Subduction Zone. Dataset: Pavlis et al. (2012)

as follows. The 'pscoast' module was used to plot colored, or textured land-masses on maps and draws vector topographic elements: coastlines, rivers, and political boundaries. The 'psxy' module was used to plot lines, polygons, or symbols using their coordinate locations on a map. For example, the dot spots of the volcanos and ophiolites, the plate boundaries and lineaments of trench and ridges were visualized using the 'psxy' module. The 'pslegend' is a cartographic auxiliary module that was used to add horizontally-placed color legends below the maps. The 'psbasemap' is a main cartographic module that specifies the region of interest (West-East-South-North), enables to apply a cartographic projection, defines basic cartographic elements: grid, coordinates, draws boundary frame and axes attributes. Other modules included, for instance, the 'grdimage', used to visualize the raster images, and the 'pstext', used to overlay texts and annotations in a layout.

To arrange recognition of the area, the names of the most important tectonic structures were plotted

using 'echo' Unix utility and a GMT module 'pstext'. The geoid undulations are intrinsically referenced to an ideal mean-earth ellipsoid into undulations referenced to WGS 84. The relation between the WGS 84 and the associated normal gravity field, to which the geoid undulations are referenced, consists in the defined constants used to model reference ellipsoid of the Earth (Hofmann-Wellenhof et al., 1993) and gravity models. The visualized EGM96 grid presents an Earth spherical harmonic gravitational model (Colombo, 1984). Mapping of the free-air gravity (Fig. 5) was based on the data for Earth's gravitational field visualizing global geophysical settings subset for the Cascadia Subduction Zone area derived from the USA datasets (Sandwell et al., 2014).

The sediment thickness was visualized using available global 5-arc-minute total sediment thickness grid calculated by NOAA for the world's oceans and marginal seas from the raster global grid GlobSed (Straume et al., 2019).

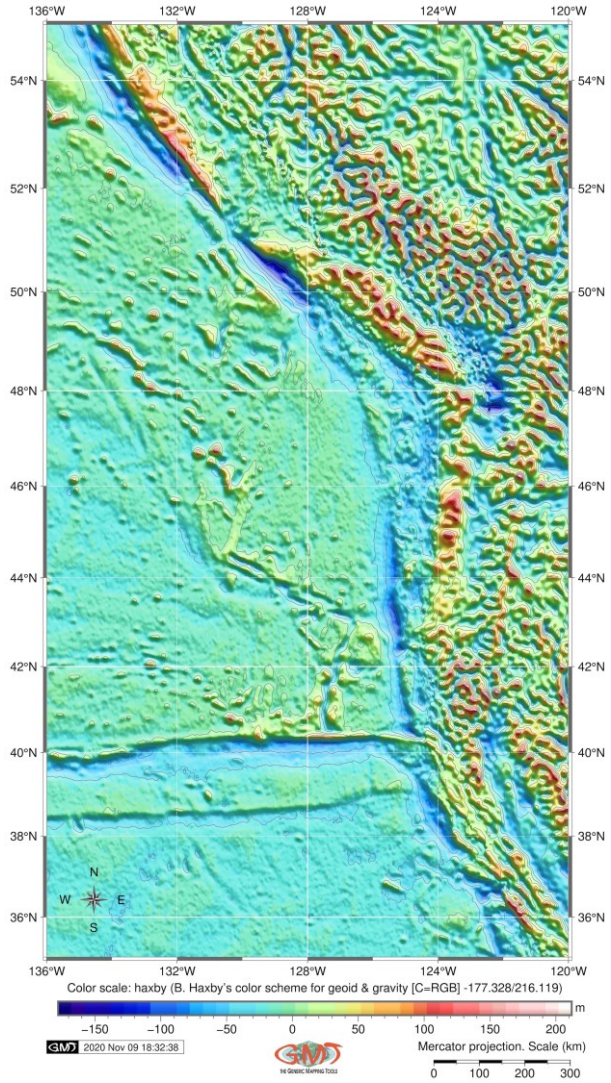

Fig. 5 Marine free-air gravity map of the Cascadia Subduction Zone. Dataset: Sandwell et al. (2014)

Focal seismic mechanisms (Fig. 2: plotted 'beach balls' along the Cascadia Subduction Zone and Juan De Fuca Plate) were plotted using data from the global CMT project (Ekström et al., 2012). The topographic map (Fig. 1), geomorphological modelling (Fig. 6) and derived statistical analysis (Fig. 7) are based on using General Bathymetric Chart of the Oceans (GEBCO). GEBCO is a high-resolution 15 arc-second raster grid of the a bathymetric and topographic grid of the Earth (GEBCO Compilation Group, 2020).

The topographic modelling of the slope steepness of the Cascadia Trench was based on the automatic plotting of the transecting segments by using the following approach. Fourteen samples (cross-sectional segments colored yellow on Fig. 6 B) were collected through the automatic digitizing of GEBCO grid in NetCDF format (GEBCO_2019.nc file) using GMT 'grdtrack' module using derived methods (Lemenkova, 2019a, 2019b) with following technical features: starting point coordinates are 131.2°W, 50.4°N end point coordinates 127.0°W 48.3°N. This segment under off Vancouver Island was chosen as a reference for the Cascadia Subduction Zone and closeness of the Anahim volcanic hotspot located in West-Central Interior of British Columbia, Canada (52°N, 123°W). Anahim is associated with earthquakes and volcanic gas emissions contributing to the geological instability of the region (Bohrmann et al., 1998). The general line and two points were plotted by the following GMT code: 'gmt psxy -R -J -W2p,red trenchCT.txt -O -K >> $ps' # line and 'gmt psxy -R -J -Sc0.15i -Gred trenchCT.txt -O K >> $ps' # points. Afterwards, the fourteen longitudinal profiles edited based on the median depth of cross-sections were drawn by the GMT module 'grdtrack' using code from the applied methodology (Lemenkova, 2019c): 'gmt grdtrack trenchCT.txt -Gct1_relief.nc -C300k/2k/20k+v -Sm+sstackCT.txt > tableCT.txt' and 'gmt psxy -R -J -W0.5p,white tableCT.txt -O -K >> $ps'. This code generated a table containing sampling points with XY (Lat/Lon) coordinates and depth value in each.

To identify topographic parameters of the selected segments' structure, the length of the cross-sections, the distance between each two and the sampling repetition along each line were unified by using the GMT flag markers in the code for samples as shown above (-C300k/2k/20k). The parameters of 'C' flag mean that sample points were measured every 2 km with a space of 20 km between each two segment (drawn as 14 yellow lines on Fig. 6B). The total length of each segment is 300 km. The bathymetric samples were recorded from the surroundings of Vancouver Island, western Canada, where northern part of the Cascadia Subduction Zone is stretching.The first four samples (from the north) are also crossing the Canadian mainland located in British Columbia area.

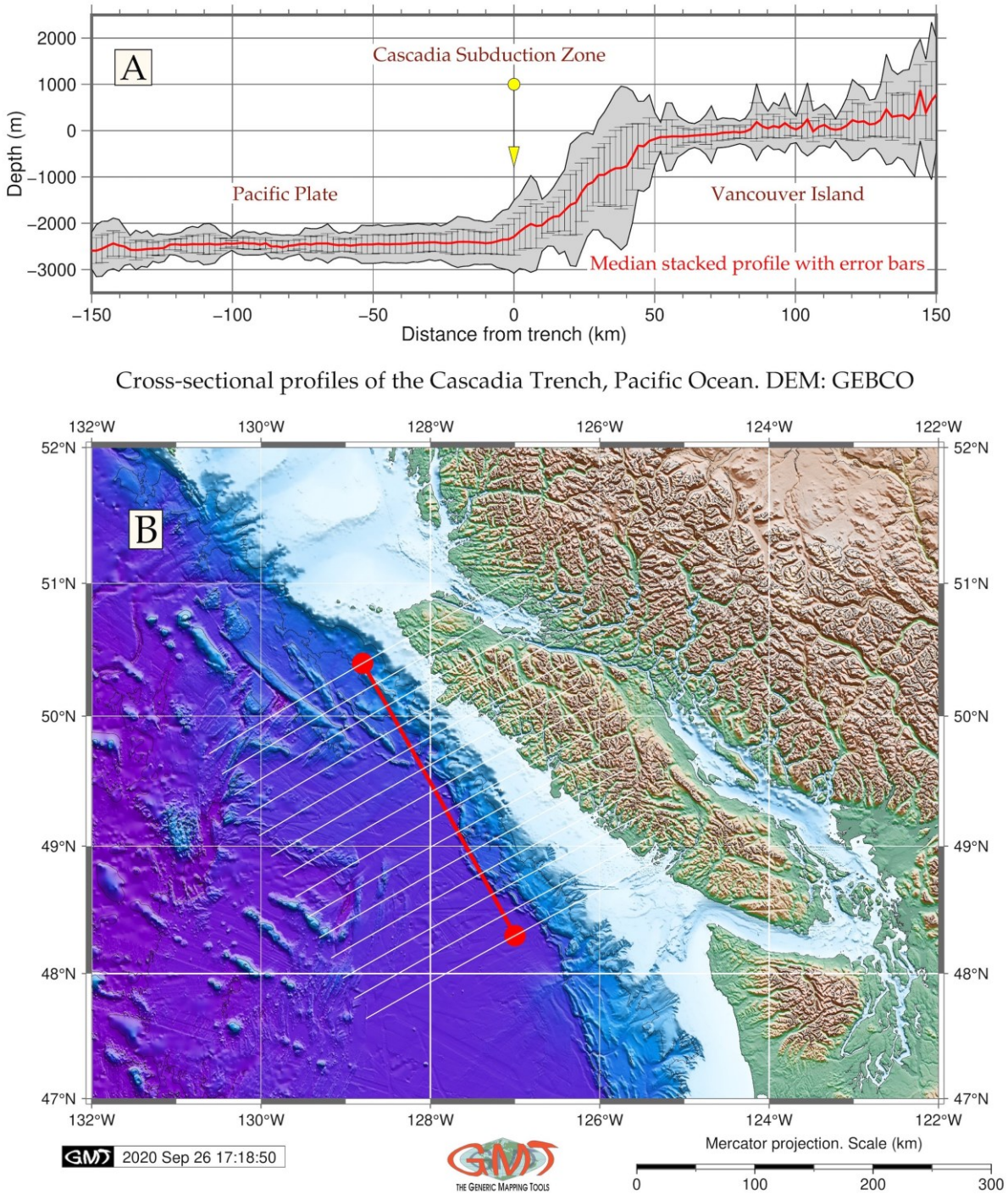

Fig. 6 Longitudinal profiles edited based on the median depth of cross-sectional profiles in the Cascadia Subduction Zone off Vancouver Island. Dataset: GEBCO Compilation Group (2020)

The location of the sampling segments plots was chosen not only according to their geomorphic specificity as the topographic segments well representing both the terrestrial relief and submarine bathymetry of the trench, but also for the geologic reasons showing tectonic plate boundaries: the samples cross both Juan De Fuca Plate and partially the Pacific Plate. Modeled geomorphic cross-section of the trench is visualized (Fig. 6A) using GMT 'psxy' module (code snippet: 'gmt psxy -R -J -W1.0p -Ey+p0.2p stackCT.txt -O -K >> $ps' and 'gmt psxy -R -J -W1.0p,red stackCT.txt -O -K >> $ps') with annotations plotted by 'echo' Unix utility.

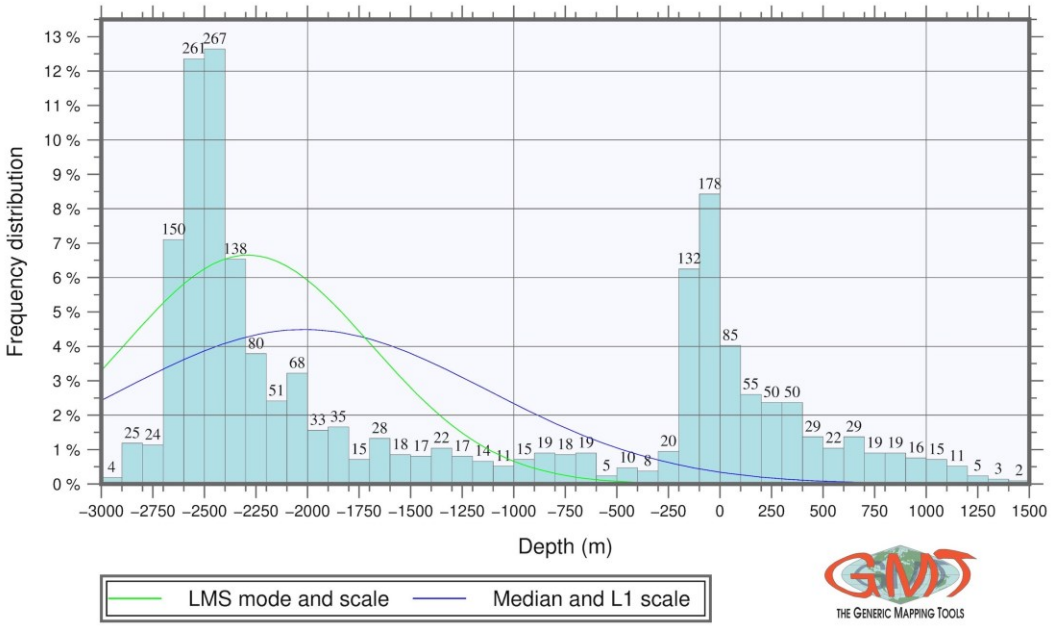

Fig. 7 Depth distribution in the Cascadia Subduction Zone west of Vancouver Island

RESULTS

The transect of the seafloor geomorphology of the Cascadia Trench offshore Vancouver Island is represented on Fig. 6A. The Cascadia Trench is unique among other trenches due to its shape with almost no V-formed typical form, e.g. like in others trenches of the Pacific Ocean: Vityaz, Vanuatu, Mariana, Middle America, Kuril-Kamchatka, studied and described previously (Lemenkova, 2019e, 2020a, 2020b). The actual trench depression of the Cascadia Trench cannot be recognized in the geomorphic cross-section of the seafloor, indicating that the trench is completely filled, that is, flooded with sediments. This corresponds to the map visualizing sediment thickness in the study area showing that Cascadia Trench axis has sediment thickness of 800–1600 m according to the GlobSed data (Fig. 3). However, even though the bathymetric V-form typical for the oceanic trench is missing. The term trench is used, even if it is filled with sediments, since the sediment infill and the structure of the lithosphere are independent from each other.

The slopes of the Cascadia Trench are steeper and significantly higher on the continental slope side of North America and Vancouver Island than on the opposite oceanward side (Fig. 6A). The geomorphology of the eastern side of the Cascadia Trench is characterized by a gentle curvature (35.12°) with partially stepped structure. Opposite side (oceanward) is almost completely leveled so the trench cross-section has a form of a hill side. The depth in the trench is greater than in the ocean basin; however, the Cascadia Trench is rather narrow comparing to other deep-sea trenches: the maximal depth at the selected segment was detected as -3489 m and for the whole dataset it is -6201 m according to the GEBCO (15 arc-sec resolution raster grid). The bottom of the trench is mostly flat due to the high sedimentation rates. This also indicates the development of the accumulative leveling processes.

The results show (Fig. 6) that, in general, the topography of the Cascadia Subduction Zone off Vancouver Island varies with asymmetric relief of the Cascadia Trench showing elevations in the eastern part of the cross-sections gradually decreasing eastwards, separated by a relatively low relief in the central part of the segment. Such a systematic bathymetric variability may reflect the geological factors including epirogenic movements. The Cascadia Subduction Zone has asymmetric bathymetric profiles across the trench. Bathymetry of the oceanward side of the Cascadia Trench is dictated by the subduction of the tectonic plates of Juan De Fuca and North American (Fig. 2). The absolute depths are mainly controlled by the elastic thickness of the lithosphere and age of the subducting tectonic plate (Bodine and Watts, 1979).

Not clearly expressed bathymetry on the oceanic plate is contrasting to a high geomorphological complexity on the landward slope of the Cascadia Trench where multiple steep thrust ridges dominate the continental slope (Fig. 6A). A series of landward-dipping, flat-lying, channels mark the filling of erosional topography and coastal reworking of the irregular shoreline following inundation and erosion (Simms et al., 2017). Multiple canyons and thrust ridge along the inner slope of the Cascadia Trench cause active sediment transport from the continental slope, Vancouver Island and shelf through erosion and reflected in the asymmetric tilted seafloor (Davis et al., 2017).

Marine free-air gravity anomalies (Fig. 5) along the Cascadia Subduction Zone on the shelf of North

America are characterized by zero and weakly positive gravity in milligal (up to 20 mGal). The values increase then rapidly in the zone of the continental slope reaching above 200 mGal at the continental foot, which is associated with a decrease in the thickness of the Earth's crust. There is a vast region of negative Faye's anomalies (up to –40 mGal). Comparing to the previous studies on Bouguer anomalies (Gainanov, 1980), the regions of the marginal plateaus are notable for positive values of Bouguer anomalies (80 to 160 mGal), which can be explained by the impact of the subcontinental crust blocks forming the basement of these structures, while in California Gulf they vary from –120 mGal in the coastal zone to +200 or +250 mGal above the seafloor. The continental margin in the Mendocino Fracture Zone is a special area. Here the submarine rift zone of the East Pacific Rise continues on the land through the Gulf of California.

The histograms (Fig. 7) illustrate the frequency of depths distribution for the segment of Cascadia Trench analyzed for each cross-section profile. It indicates, based on the summarized data, that the distribution has two modi, one modus at -2500 to -2400 m (267 samples) and another at -2500 to -2600 m (261 samples). In accordance with this statement, the data for depths above -3000 m reflect the worst performance in the topographic profile. In context of the comparative analysis by histograms, the topographic variations demonstrate relatively wide shallow areas and a steep decrease in depth. Thus, the depths from -2000 m decrease drastically (the exception is an interval of -2000 to -2100 m with 68 samples). The second peak in the data range lies in the interval of -200 to 400 m taking in total 550 samples indicating shelf and coastal areas that cover relatively large areas near the Vancouver Island. Data on areas of the continental slope are distributed evenly: depth bins from -200 to -1800 m do not exceed 30 samples in each bin (in total 256 samples for 16 bins) following by two small bins for the interval of -1800 to -2000 m (in total 68 samples for the two bins). Terrestrial areas demonstrate gradual smooth decrease in elevations from 0 to 1500 m.

DISCUSSION

Methods of effective visualization of the submarine geomorphology of the deep-sea trenches is a challenging task given its applications in marine geology studies. An application of the GMT is, however, lacking in view of the popularity of the traditional GIS application (e.g. ArcGIS, QGIS and other software). This study combines a new approach of the data-driven mapping of the Cascadia Trench by GMT applied for visualization of the geological (sedimentation) and geophysical settings using high-resolution datasets and geomorphic modelling of the trench relying on cross-sectional. The study was complemented by measurements of depth along the cross-sectional profile using defined parameters (sampling frequency, depth, cross-section extent) to model the profile of the trench in a selected segment westward of the Vancouver Island.

The research applies the GMT scripting methods to a series of high-resolution raster datasets including GEBCO, EGM-2008, ETOPO1, GlobSed and vector layers derived from SIO. Thus, in this study, the Cascadia Subduction Zone was subset from the global grids and visualized by GMT and several raster datasets. In this way, the study presents a multi-source data analysis of the trench geomorphology by a cross-section profile, supported by the visualization of the thematic maps. All maps were plotted in GMT considering layouts, projections, elements of content, scale, design, etc. The advantage of the GMT scripting approach consists in the automatization which enables to generate maps with the same resolution from given datasets (GEBCO, EGM-2008, ETOPO1) at any scale by executing script from the console, and then printing and converting a PostScript file.

An asymmetric type of the submarine profile of the trench was identified using automated methods of GMT. The following findings arise. (i) Spatial correlations analyzed from the comparison of datasets on marine free-air gravity anomalies, topography, geoid based on the EGM-2008, and sediment thickness translate relationships between the geological and geophysical entities. These are highlighted by the contour similarities notable on data distribution and isolines of the distribution of these phenomena in space, and spatial connection in variations of the datasets. Thus, the distribution of the sediment thickness well correlates with the submarine relief and the highest values occupy the marginal part of the coastal area of Vancouver Island which correlates with the topographic relief of the study area. (ii) Submarine geomorphology of the trench is strongly controlled by tectonics and topographic location along the continental margin. Irregular geomorphic shapes are located on the continental slope while the submarine part of the profile flattens down to the basin floor. (iii) Correspondence between the geoid, marine free-air gravity and tectonics (correlation with the Mendocino Escarpment and Murray Fracture Zone, clearly visible area of the Juan de Fuca Plate and the lineament of the Cascadia Trench) illustrates closely correlated phenomena of the tectonic processes reflected in geophysical settings and bathymetry. (iv) Sediment thickness shows distribution of the marine sediments as important variables visualized based on the in geological datasets. Sedimentation depend on the contribution from tributary discharge showing higher values in shallow shelf areas and almost absent or low values in the basin westward of Vancouver Island and the abyssal plains. Such behavior can be explained by decreasing inflow from the coastal areas which significantly contribute to the sedimentation.

Nowadays, the basic source of geologic information for thorough geological analysis is not a print-out map, but a dataset (e.g. in this study: GlobSed dataset with 5 arc-minute resolution, GEBCO 15 arc-second topographic grid). Dataset has not a scale, but a resolution (level of details and precision) which refers

to the original accuracy of the raw data, which in turn depends on the way of data capture or (by remote sensing approaches) satellite characteristics. Datasets enable to derive different kinds of layout maps set up for the specific area by using scripts and machine learning techniques for the processing of these areas. Sediment thickness in the Cascadia Trench axis is controlled by several parameters, including climate and geological setting, geomorphological slope in the coastal area and transport systems to the sea, across the shelf and slope. In humid areas, such as the North America, the denudation explains additional sediment influx to the Cascadia Trench, their accretion and deformation (Davis and Hyndman, 1989).

The existing river systems in western Canada (Fig. 1) additionally contribute to the sediment fill of the Cascadia Trench which in its highest values oversteps two kilometers according to the GlobSed dataset (Fig. 3). Variations in sediment thickness over different parts of the Cascadia Trench can be seen as comparative analysis of the seafloor fabrics of the Juan de Fuca Plate contrasting with Pacific Plate (Fig. 2). Young Juan de Fuca Plate (age less than 10 Ma) is covered by up to 2 km of sediments (orange to red colors in Fig. 3), which is caused by the high rate of terrigenous sediments from North America during the Pleistocene. Because Cascadia Trench is sediment flooded, the shape of its axis and western slope are not clearly seen as bathymetric features as demonstrated further in Figure 6. The topographic cross-section profile (Fig. 6) describes the geometry of the submarine terrain and seafloor of the trench using a given series of point measurements performed in an automated regime of the GMT.

CONCLUSIONS

The GMT scripting approach for cartographic mapping relied on using a GMT code syntax used for processing a series of raster high-resolution datasets, as showing in this research. Such a mapping approach uses the advantage of the repeatability and automatization of scripts and contributes to the development of the machine learning in thematic cartography. A series of maps on the Cascadia Subduction Zone has been presented with defined spatial extend and coverage visualizing relationships between the submarine topography, geophysical marine free-gravity anomalies and geologic settings of the study area. One of the technical goals of this research were visualization of the series of the thematic maps through scripts written on GMT syntax and demonstrate its functionalities for geological mapping. A data-driven paradigm presented in this research demanded an evaluation and standardization of the input datasets (i.e. quality, projections, resolution, extent, coverage, source) to increase the readability of the output maps.

The paper synthesizes results from topographic and bathymetric mapping, cross-sectional geomorphological profiling of the Cascadia Trench, geodetic and gravitational imaging, visualizing its geologic and tectonic setting, sediment thickness and geophysical properties (marine free-air gravity). Digital bathymetric and geophysical data were used to identify the topographic pattern in the selected segment of the Cascadia subduction zone. The results suggest that geomorphology of the Cascadia trench is influenced by the tectonic development of the Cascadia Subduction Zone and geological local settings of the underlying rocks which is also reflected in the gravity anomaly fields due to variations in rock density. The asymmetric shape of the trench is the result of the complex geological, geochemical and tectonic processes exposed in the Cascadia subduction zone. Processes of sediment accumulation and plate subduction affect topographic shape of the Cascadia Trench. Since the trench is a sediment filled, its cross-section transects revealed an almost completely leveled structure of the bathymetry.

The presented geospatial analysis of the multi-source datasets which include geomorphological and geological-geophysical raster grids focused to highlight the structure of the seafloor topography of the Cascadia Trench and its surroundings (Juan De Fuca Plate and Pacific Plate), indicating the role of various factors in its formation (i.e. crustal extension, uplift, tectonic plates subduction). Besides, the geomorphology of the trench is affected by the mineral properties and geochemistry. As demonstrated in this paper, mapping topographic cross-sections of the Cascadia trench was supported by the analysis of its geophysical properties and regional tectonic settings. The formation of the Cascadia Subduction Zone generally corresponds to the existing concept of plate tectonics, while at the same time confirming its main provisions. As mentioned above, the Cascadia Trench is unique among other trenches of the Pacific Ocean due to its very specific geomorphic form: almost leveled topography which results in that Cascadia Trench does not have a classic V-form cross-section. Differences in the topography of the seafloor reflect variations in physical properties of the subducted slabs which in turn are affected by the tectonic processes. Among others, these are explained by the age, rigidity and strength of the subducting Pacific Plate in the mantle.

The research included a series of the new maps of the ocean floor in the Cascadia Subduction Zone region, plotted and visualized as a result of high-resolution data processing and interpretation: topographic map (Fig. 1), geologic map including volcanic spots and tectonic morphological structures, faults, tectonic movements, lineaments of ridges and fracture zones (Fig. 2), sediment thickness (Fig. 3), modeled geoid undulations (Fig. 4), marine free-air gravity (Fig. 5), digitized and visualized 14 cross-section profiles (Fig. 6) and the results of statistical data analysis compiled as a result of the data interpretation (Fig. 7). The maps were plotted in Mercator projection using GMT cartographic scripting toolset. The representation of a series of thematic, visually effective maps covering Cascadia Subduction Zone in general coverage (Figs. 1–5) and with increasing scale (Fig. 6B) enabled to detail categorical data, such as enlarged fragment of the trench area in order to produce

a series of perpendicular cross-sectioning geomorphological profiles which were statistically processed and analyzed. As shown, the geomorphology of the Cascadia Trench reflects the active processes of sedimentation and experiences the effects of the geological factors and processes within the subduction zone. Understanding the major governing processes acting in the background of the geomorphological formation can be recommended for further studies using more extended datasets on geological, lithological and stratigraphic data.

Cascadia trench is one of the least studied oceanic trenches comparing, for instance, to the Mariana Trench or Peru-Chile Trench. A long, narrow depression of the deep seabed stretching along the western coasts of North America, it has a specific geomorphological shape caused by a complexity of the geological conditions, high sedimentation rate, repetitive earthquakes and constant processes of the tectonic plate subduction. Although shallower comparing to the deepest trenches of the Earth (Mariana, Tonga, Kermadec), its depths are greater than those of the adjacent deep ocean basin (-6201 m according to GEBCO dataset). In the modern plate tectonic context Cascadia Trench is structurally connected to convergent plate boundaries, defining the zones where North American Plate is moving in roughly a southwest direction and Pacific Plate moving to the northwest.

A special phenomena of the submarine geomorphology of the deep-sea trenches in contrast to the terrestrial studies consists in the fact that seafloor is hidden from the direct observations. As a result, the marine geological datasets can only be processed, visualized and mapped using advanced cartographic technologies and high-resolution datasets received by satellite-based remote sensing methods (GEBCO, ETOPO1, EGM-2008). In view of this, the advantage of the application of advanced GMT module scripting algorithms for automated data visualization, modelling and mapping is obvious. The GMT, as demonstrated in this research, presents excellent tools for the raster grids processing enabling perform a geospatial analysis and mapping thematic grids.

In Cascadia subduction zone, high-resolution analysis of thematic datasets and modelling of the geomorphic profile helps understanding of regional geomorphological settings. Sedimentary records differ across the study area of varying sediment supply, topography and geologic settings controlling sediment sources. Variations in the data distribution by the GMT advanced cartographic tools reflect these factors. This GMT-based spatial data analysis and modeling highlights the importance of an advanced cartographic tools and approaches for thorough understanding of the Cascadia trench geomorphology, geophysics and the interplay of sedimentation and local tectonics when sediment thickness in continental margins.

The topographic shape of deep-sea trenches was discovered in the 20th century mainly through a precise method of measuring gravity at sea developed by a Dutch geophysicist F.A. Vening-Meinesz. As a result of both increase in bathymetric measurements since the 1960s and intensive development of machine learning technical methods of data processing during computerization (since the 1980s and especially the 2000s) the modelling techniques have developed enabling to visualize the geomorphology of deep sea trenches. The precision of the topographic and bathymetric mapping of oceanic trenches, the least accessible objects on the Earth, was increased by the widespread use of the remote sensing techniques including echo-sounding. However, the progress in our understanding of oceanic trenches still requires more detailed and complex studies using advanced methods of machine learning with combination of high-resolution datasets. The presented study contributed to such task with a special focus on the Cascadia Subduction Zone, western coasts of Canada and the USA.

ACKNOWLEDGEMENTS

This research was implemented in the framework of the Project Nr. 0144-2019-0011, Schmidt Institute of Physics of the Earth, Russian Academy of Sciences, and China Scholarship Council (CSC), State Oceanic Administration (SOA), Marine Scholarship of China, Grant Nr. 2016SOA002, People's Republic of China.

References

Agostinetti, N.P, Miller, M.S. 2014. The fate of the downgoing oceanic plate: Insight from the Northern Cascadia subduction zone. *Earth and Planetary Science Letters* 408 (15), 237–251. DOI: 10.1016/j.epsl.2014.10.016

Amante, C., Eakins, B.W. 2009. ETOPO1 1 Arc-Minute Global Relief Model: Procedures, Data Sources and Analysis. NOAA Technical Memorandum, 19. DOI: 10.7289/V5C8276M

Atwater, B.F., Carson, B., Griggs, G.B., Johnson, H.P., Salmi, M.S. 2014. Rethinking turbidite paleoseismology along the Cascadia subduction zone. *Geology* 42, 827–830. DOI: 10.1130/G35902.1

Bohrmann G., Greinert J., Suess E., Torres, M. 1998. Authigenic carbonates from the Cascadia subduction zone and their relation to gas hydrate stability. *Geology* 26(7), 647–650. DOI: 10.1130/0091-7613(1998)026<0647:ACFTCS>2.3.CO;2

Bodine, J.H., Watts, A.B. 1979. On lithospheric flexure seaward of the Bonin and Mariana trenches. *Earth and Planetary Science Letters* 43, 132–148. DOI:10.1016/0012-821X(79)90162-6.

Bodmer, M., Toomey, D.R., Roering, J.J., Karlstrom, L. 2020. Asthenospheric buoyancy and the origin of high-relief topography along the Cascadia forearc. *Earth and Planetary Science Letters* 531(1) 115965. DOI: 10.1016/j.epsl.2019.115965

Carpentier, M., Weisa, D., Chauvel, C. 2014. Fractionation of Sr and Hf isotopes by mineral sorting in Cascadia Basin terrigenous sediments. *Chemical Geology* 382(29), 67-82. DOI: 10.1016/j.chemgeo.2014.05.028

Colombo, O.L. 1984. The Global Mapping of Gravity with Two Satellites. *Nederlands Geodetic Commission*, 7(3). Publications on Geodesy, New Series.

Coppola, L., Gustafsson, Ö., Andersson, P., Eglinton, T.I., Uchida, M., Dickens, A.F. 2007. The importance of ultrafine particles as a control on the distribution of organic carbon in Washington Margin and Cascadia Basin sediments. *Chemical Geology* 243(1–2), 142–156. DOI: 10.1016/j.chemgeo.2007.05.020

Davis, E.E., Heesemann, M., Lambert, A. He, J. 2017. Seafloor tilt induced by ocean tidal loading inferred from broadband seismometer data from the Cascadia subduction zone and Juan de Fuca Ridge. *Earth and Planetary Science Letters* 463(1), 243–252. DOI: 10.1016/j.epsl.2017.01.042

Davis, E.E., Hyndman, R.D. 1989. Accretion and recent deformation of sediments along the northern Cascadia subduction zone. *Geological Society of America Bulletin* 101, 1465–1480. DOI: 10.1130/0016-7606(1989)101<1465:aardos>2.3.co;2

Ekström G., Nettles M., Dziewonski A.M. 2012. The global CMT project 2004-2010: Centroid-moment tensors for 13,017 earthquakes. *Physics of the Earth and Planetary Interior*s 200–201, 1–9. DOI: 10.1016/j.pepi.2012.04.002

Evans, R.L., Wannamaker, P.E., McGary, R.S., Elsenbeck, J. 2014. Electrical structure of the central Cascadia subduction zone: The EMSLAB Lincoln Line revisited. *Earth and Planetary Science Letters* 402(15), 265–274. DOI: 10.1016/j.epsl.2013.04.021

Flueh, E.R., Fisher, M.A., Bialas, J., Childs, J.R., Klaeschen, D., Kukowski, N., Parsons, T., Scholl, D.W., ten Brink, U.S., Trehu, A.M., Vidal, N. 1998. New seismic images of the Cascadia subduction zone from cruise SO108-ORWELL. *Tectonophysics* 293, 69–84. DOI: 10.1016/S0040-1951(98)00091-2

Gainanov, A.G. 1980. Gravimetric studies of the Earth's crust of the oceans. Moscow, MSU Press, 240 p.

Gauger, S., Kuhn, G., Gohl, K., Feigl, T., Lemenkova, P., Hillenbrand, C. 2007. Swath-bathymetric mapping. *Reports on Polar and Marine Research* 557, 38–45.

GEBCO Compilation Group 2020. The GEBCO_2020 Grid. DOI: 10.5285/a29c5465-b138-234d-e053-6c86abc040b9

Geersen, J., Voelker, D., Behrmann, J.H. 2018. Oceanic Trenches. In: Micallef, A., Krastel, S., Savini, A. (eds.) Submarine Geomorphology. Springer International Publishing AG, 409–425. DOI: 10.1007/978-3-319-57852-1

Greene, H.G., Barrie, J.V., Todd, B.J. 2018. The Skipjack Island fault zone: An active transcurrent structure within the upper plate of the Cascadia subduction complex. *Sedimentary Geology* 378(15), 61–79. DOI: 10.1016/j.sedgeo.2018.05.005.

Guzzetti, F., Cardinali, M., Reichenbach, P. 1996. The influence of structural setting and lithology on landslide type and pattern. *Environmental and Engineering Geosciences* 2(4), 531–555. DOI: 10.2113/gseegeosci.ii.4.531

Hofmann-Wellenhof, B., Lichtenegger, H. Collins, H.J. 1993. Global Positioning System. New York: Springer-Verlag Wien.

Hutchinson, I., Clague, J. 2017. Were they all giants? Perspectives on late Holocene plate-boundary earthquakes at the northern end of the Cascadia subduction zone. *Quaternary Science Reviews*, 169(1) 29–49. DOI: 10.1016/j.quascirev.2017.05.015

Klaučo, M., Gregorová, B., Stankov, U., Marković, V., Lemenkova, P. 2013. Determination of ecological significance based on geostatistical assessment: a case study from the Slovak Natura 2000 protected area. *Central European Journal of Geosciences* 5(1), 28–42. DOI: 10.2478/s13533-012-0120-0

Klaučo, M., Gregorová, B., Stankov, U., Marković, V., Lemenkova, P. 2014. Landscape metrics as indicator for ecological significance: assessment of Sitno Natura 2000 sites, Slovakia. *Ecology and Environmental Protection. Proceedings of the International Conference*. March 19–20, 2014. Minsk, Belarus, 85–90. DOI: 10.6084/m9.figshare.7434200

Kuhn, G., Hass, C., Kober, M., Petitat, M., Feigl, T., Hillenbrand, C.D., Kruger, S., Forwick, M., Gauger, S., Lemenkova, P. 2006. The response of quaternary climatic cycles in the South-East Pacific: development of the opal belt and dynamics behavior of the West Antarctic ice sheet. In: Gohl, K. (ed). *Expeditionsprogramm Nr. 75 ANT XXIII/4, AWI*. DOI: 10.13140/RG.2.2.11468.87687

Lemenkova, P. 2011. Seagrass Mapping and Monitoring Along the Coasts of Crete, Greece. M.Sc. Thesis. Netherlands: University of Twente. 158 p. DOI: 10.31237/osf.io/p4h9v

Lemenkova, P., Promper, C., Glade, T. 2012. Economic Assessment of Landslide Risk for the Waidhofen a.d. Ybbs Region, Alpine Foreland, Lower Austria. In: Eberhardt, E., Froese, C., Turner, A.K., Leroueil, S. (eds.) Protecting Society through Improved Understanding. 11th International Symposium on Landslides and the 2nd North American Symposium on Landslides and Engineered Slopes (NASL), June 2–8, 2012. Banff, AB, Canada, 279–285. DOI: 10.13140/RG.2.2.10077.05600

Lemenkova, P. 2018. R scripting libraries for comparative analysis of the correlation methods to identify factors affecting Mariana Trench formation. *Journal of Marine Technology and Environment* 2, 35–42. DOI: 10.31223/osf.io/437uw

Lemenkova, P. 2019a. Topographic surface modelling using raster grid datasets by GMT: example of the Kuril-Kamchatka Trench, Pacific Ocean. *Reports on Geodesy and Geoinformatics* 108, 9–22. DOI: 10.2478/rgg-2019-0008

Lemenkova, P. 2019b. GMT Based Comparative Analysis and Geomorphological Mapping of the Kermadec and Tonga Trenches, Southwest Pacific Ocean. *Geographia Technica* 14(2), 39–48. DOI: 10.21163/GT_2019.142.04

Lemenkova, P. 2019c. Geomorphological modelling and mapping of the Peru-Chile Trench by GMT. *Polish Cartographical Review* 51(4), 181–194. DOI: 10.2478/pcr-2019-0015

Lemenkova, P. 2019d. Statistical Analysis of the Mariana Trench Geomorphology Using R Programming Language. *Geodesy and Cartography* 45(2), 57–84. DOI: 10.3846/gac.2019.3785

Lemenkova, P. 2019e. AWK and GNU Octave Programming Languages Integrated with Generic Mapping Tools for Geomorphological Analysis. *GeoScience Engineering* 65 (4), 1–22. DOI: 10.35180/gse-2019-0020

Lemenkova, P. 2020a. GMT-based geological mapping and assessment of the bathymetric variations of the Kuril-Kamchatka Trench, Pacific Ocean. *Natural and Engineering Sciences* 5(1), 1–17. DOI: 10.28978/nesciences.691708

Lemenkova, P. 2020b. GMT Based Comparative Geomorphological Analysis of the Vityaz and Vanuatu Trenches, Fiji Basin. *Geodetski List* 74(97), 1, 19–39. DOI: 10.6084/m9.figshare.12249773

Lemoine F.G., Kenyon S.C., Factor J.K., Trimmer R.G., Pavlis N.K., Chinn D.S., Cox C.M., Klosko S.M., Luthcke S.B., Torrence M.H., Wang Y.M., Williamson R.G., Pavlis E.C., Rapp R.H., Olson T.R. 1998. NASA/TP-1998-206861: The Development of the Joint NASA GSFC and NIMA Geopotential Model EGM96, NASA Goddard Space Flight Center, Greenbelt, Maryland, 20771 USA.

Li, D., McGuire, J.J., Liu, Y., Hardebeck, J.L. 2018. Stress rotation across the Cascadia megathrust requires a weak subduction plate boundary at seismogenic depths. *Earth and Planetary Science Letters* 485(1), 55–64. DOI: 10.1016/j.epsl.2018.01.002.

Long, M.D. 2016, The Cascadia Paradox: Mantle flow and slab fragmentation in the Cascadia subduction system. *Journal of Geodynamics* 102, 151–170. DOI: 10.1016/j.jog.2016.09.006

Pavlis, N.K., Holmes, S.A., Kenyon, S.C., Factor, J.K. 2012. The development and evaluation of the Earth Gravitational Model 2008 (EGM2008). *Journal of Geophysical Research* 117, B04406, DOI: 10.1029/2011JB008916.

Penserini, B.D., Roering, J.J., Streig. A. 2017. A morphologic proxy for debris flow erosion with application to the earthquake deformation cycle, Cascadia Subduction Zone, USA. *Geomorphology* 282, 150–161. DOI: 10.1016/j.geomorph.2017.01.018

Perkins, J.P., Roering, J.J., Burns, W.J., Struble, W., Black, B.A., Schmidt, K.M., Duvall, A., Calhoun, N. 2018. Hunting for landslides from Cascadia's great earthquakes, *Eos*, 99, 1–9. DOI: 10.1029/2018EO103689.

Sandwell D.T., Müller R.D., Smith W.H.F., Garcia E., Francis R. 2014. New global marine gravity model from CryoSat-2 and Jason-1 reveals buried tectonic structure. *Science*, 346(6205), 65–67. DOI: 10.1126/science.1258213

Schenke, H.W., Lemenkova, P. 2008. Zur Frage der Meeresboden-Kartographie: Die Nutzung von AutoTrace Digitizer für die Vektorisierung der Bathymetrischen Daten in der Petschora-See. *Hydrographische Nachrichten* 81, 16–21. DOI: 10.6084/m9.figshare.7435538

Simms, A.R., DeWitt, R., Zurbuchen, J., Vaughan, P. 2017. Coastal erosion and recovery from a Cascadia subduction zone earthquake and tsunami. *Marine Geology* 392(1), 30–40. DOI: 10.1016/j.margeo.2017.08.009

Straume, E.O., Gaina, C., Medvedev, S., Hochmuth, K., Gohl, K., Whittaker, J.M., Abdul Fattah, R., Doornenbal, J.C., Hopper, J.R. 2019. GlobSed: Updated total sediment thickness in the world's oceans. *Geochemistry, Geophysics, Geosystems* 20(4), 1756–1772. DOI: 10.1029/2018GC008115

Suetova, I.A., Ushakova, L.A., Lemenkova, P. 2005a. Geoinformation mapping of the Barents and Pechora Seas. *Geography and Natural Resources* 4, 138–142. DOI: 10.6084/m9.figshare.7435535

Suetova, I.A., Ushakova, L.A., Lemenkova, P. 2005b. Geoecological Mapping of the Barents Sea Using GIS. In: *International Cartographic Conference*. DOI: 10.6084/m9.figshare.7435529

Wessel, P., Smith, W.H.F. 1991. Free software helps map and display data. *Eos Transactions AGU* 72 (41), 441. DOI: 10.1029/90EO00319

Wessel, P., Smith, W.H.F., Scharroo, R., Luis, J.F., Wobbe, F. 2013. Generic mapping tools: Improved version released. *Eos Transactions AGU* 94(45), 409– 410. DOI: 10.1002/2013EO450001

sciendo

Journal of Environmental Geography 13 (3–4), 27–33.

DOI: 10.2478/jengeo-2020-0009
ISSN 2060-467X

ASSESSING THE IMMEDIATE EFFECT OF COVID-19 LOCKDOWN ON AIR QUALITY: A CASE STUDY OF DELHI, INDIA

Ankit Sikarwar[1]*, Ritu Rani[1]

[1]Department of Development Studies, International Institute for Population Sciences, Mumbai, Maharashtra 400088, India
*Corresponding author, e-mail: anks.sik@gmail.com

Research article, received 28 July 2020, accepted 30 September 2020

Abstract

In India, a nationwide lockdown due to COVID-19 has been implemented on 25 March 2020. The lockdown restrictions on more than 1.3 billion people have brought exceptional changes in the air quality all over the country. This study aims to analyze the levels of three major pollutants: particulate matter sized 2.5 μm ($PM_{2.5}$) and 10 μm (PM_{10}), and nitrogen dioxide (NO_2) before and during the lockdown in Delhi, one of the world's most polluted cities. The data for $PM_{2.5}$, PM_{10}, and NO_2 concentrations are derived from 38 ground stations dispersed within the city. The spatial interpolation maps of pollutants for two times are generated using Inverse Distance Weighting (IDW) model. The results indicate decreasing levels of $PM_{2.5}$, PM_{10}, and NO_2 concentrations in the city by 93%, 83%, and 70% from 25 February 2020 to 21 April 2020 respectively. It is found that one month before the lockdown the levels of air pollution in Delhi were critical and much higher than the guideline values set by the World Health Organization. The levels of air pollution became historically low after the lockdown. Considering the critically degraded air quality for decades and higher morbidity and mortality rate due to unhealthy air in Delhi, the improvement in air quality due to lockdown may result as a boon for the better health of the city's population.

Keywords: COVID-19, Lockdown, Air pollution, Delhi, Spatial interpolation

INTRODUCTION

The world is facing unforeseen challenges to cope up with the unprecedented growth of Coronavirus Disease (COVID-19). The exponential widespread of the COVID-19 has become a global pandemic that has led to pernicious consequences in various parts of the world. COVID-19 was first identified in December 2019 in the province of Wuhan, China (Kucharski et al., 2020; Zhu et al., 2020), and around four months later it has adversely affected life and economy in more than a hundred countries (WHO, 2020). To curb the spread of this highly contagious disease and minimize the fatality, different countries have adopted drastic yet important measures to reduce the interaction among individuals such as banning large-scale public and private gatherings, imposing a curfew, restraining transportation, promoting social distancing, creating strict quarantine instructions, and locking down countries, states and cities, depending on the country-specific situation.

On the one hand, the cost of enacting the preventive measures against COVID-19 is immense, but on the brighter side, it could have some significant benefits on society too. For example, locking down the country might do contribution to the improvement of overall environmental conditions. This improvement may partially equilibrate the cost of these counter COVID-19 measures. For example, according to Singh and Chakraborty (2020) cities across India, which were the 14 most polluted cities during the last year in the world out of 20, are breathing some of the cleanest air after the nationwide implementation of lockdown. Recently, many researchers have attempted to study the effect of COVID-19 lockdown on air pollution at different levels (Dutheil et al., 2020; Li et al., 2020; Muhammad et al., 2020; Sharma et al., 2020; Wang et al., 2020).

Since the 1990s, Delhi has been ranked as one of the most polluted cities among the world's developing countries (Gujrar et al., 2004; WHO, 2016). Particularly, air pollution caused by onsite burning of agricultural crop residue is one of the many causes of critical levels of air pollution in the northern part of India (Satyendra et al., 2013). The higher level of air pollution in the overcrowded Delhi cause significant public health problems (Dholakia et al., 2013; Rizwan et al., 2013). Due to severely degraded air quality, in 2017, a community health emergency was declared in Delhi by the Indian Council of Medical Research (Chowdhury et al., 2019). A study by Goyal (2003) points out that vehicular emission has shown a decreasing trend due to the CNG (Compressed Natural Gas) implementation. But, the overall particulate matter concentration has seen a consistent rise (Kumar and Goyal, 2014; Gujrar et al., 2016; Nagpure et al., 2016). Moreover, air pollution also has severe implications on society, economy, and the environment including climate change. Therefore, it has become a

paramount concern of public health, environment, and development (Kampa and Castanas, 2008).

However, the extent of lockdown varies across different countries and cities around the globe depending on the number of cases. Undoubtedly, the lockdown has put a temporary rest to a significant number of social and economic activities in the countries and their people (Alvarez et al., 2020; Inoue and Todo, 2020). Overall, the significance and impacts of lockdown are yet not well understood and likely to have a significant role in the restoration of air quality (Mahato et al., 2020). Therefore, to analyze and to understand the temporary improvement in air quality due to COVID-19 lockdown is important in Delhi, which is one of the most polluted cities in the world. Moreover, it could be considered as an effective alternative measure to combat air pollution issues.

India first announced a public curfew on 22 March 2020, and later imposed a nationwide lockdown from 25 March 2020 till 15 April, and extended it further until 3 May 2020 to block the spread of the virus. Looking at the severity of increasing numbers of infections, the third phase of lockdown was extended till 17 May 2020 with the classification of districts into three severity zones (i.e. red, orange, and green). Nationwide lockdown amid the COVID-19 outbreak has created a unique scope for researchers to work in this direction and to suggest future policy measures to control air pollution in cities with degraded air quality. Addressing the above-mentioned points, the present study aims to understand the impact of COVID-19 lockdown on the air quality of Delhi by comparing the levels of air pollutants ($PM_{2.5}$, PM_{10}, and NO_2) before and during the lockdown. When most of the recent studies have dealt with national level measurement of air pollution based on satellite estimates (Dutheil et al., 2020; Li et al., 2020; Muhammad et al., 2020; Sharma et al., 2020; Wang et al., 2020), this study attempts to analyze the data from 38 ground monitoring stations to study the lockdown effect on Delhi's air quality.

STUDY AREA

Delhi, officially the National Capital Territory of Delhi, is a city and a union territory of India located at 28.61°N and 77.23°E (Fig. 1). This city is the administrative center and the second financial capital of India. With the geographical area of 1485 km2, Delhi holds the second position in the list of leading megacities of the world (United Nations, 2018). It stands as India's largest urban agglomeration with more than 15 million people with a population density of 11297 people per km2 (Chandramouli and General, 2011). Two prominent features of the geography of Delhi are the Yamuna flood-plains and the Delhi Ridge. This type of location provides favourable conditions for the accumulation of polluted air masses. The Yamuna River was the historical boundary between the states of Punjab and Uttar Pradesh, and its flood plains provide fertile alluvial soil suitable for agriculture but are prone to recurrent floods. Delhi has been continuously inhabited since the 6th century BC (Asher, 2000). Through most of its history, Delhi has served as a capital of various kingdoms and empires. It has been captured, ransacked, and rebuilt several times, particularly during the medieval period, and modern Delhi is a cluster of many cities spread across the metropolitan region (Sikarwar and Chattopadhyay, 2020).

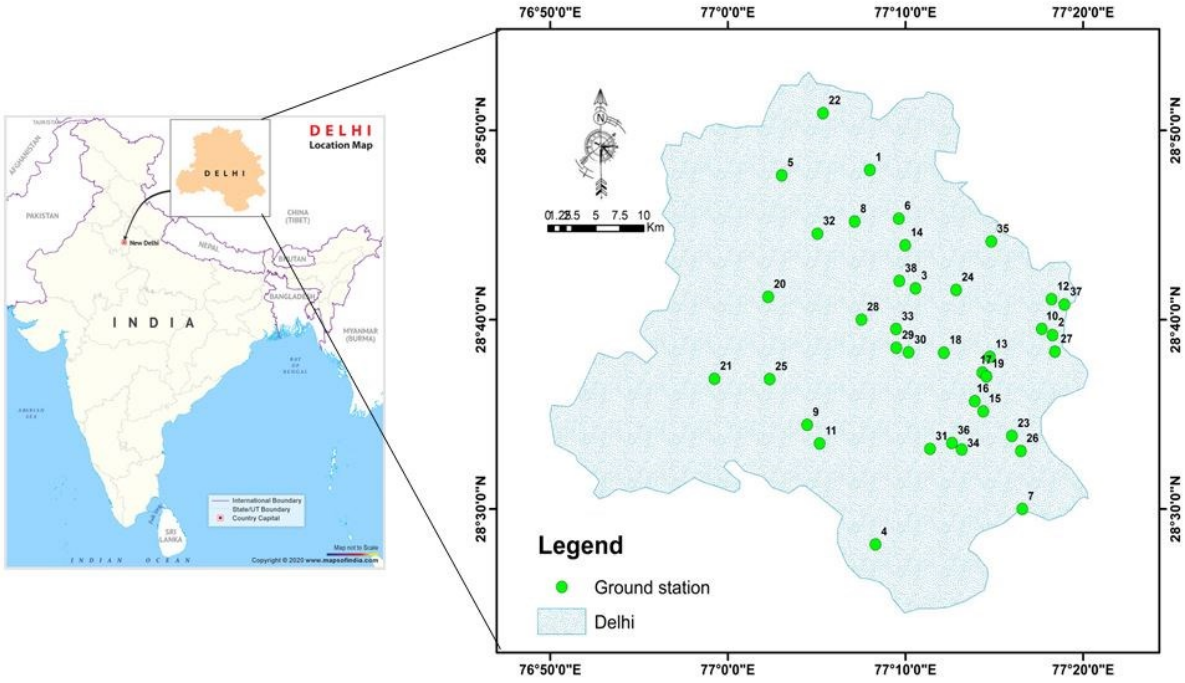

Fig. 1 The study was performed in the city of Delhi. The map shows the administrative extent of the city and ground- based air-monitoring stations considered in the study

DATA AND METHODS

To assess the air quality status of Delhi before and during the lockdown period, data from 38 air quality monitoring stations situated at various parts of the city has been taken into consideration (Table 1). These ground monitoring stations are managed under the authority of three main organizations namely CPCB (Central Pollution Control Board), DPCC (Delhi Pollution Control Committee), and IMD (Indian Meteorological Department). The 24-hour average concentration of three major pollutants including Particulate Matter 2.5 ($PM_{2.5}$), Particulate Matter 10 (PM_{10}), and Nitrogen Dioxide (NO_2) have been obtained from the CPCB online dashboard for air quality data dissemination (https://app.cpcbccr.com/ccr/#/caaqm-dashboard-all/) running by the Central Control Room for Air Quality Management. As described by the Environmental Protection Agency (2020) particulate matter contains microscopic solids or liquid droplets that are so small that they can be inhaled and cause serious health problems. Particles less than 10 µm in diameter (PM_{10}) can get deep into the lungs and some may even get into the bloodstream. Particles less than 2.5 µm in diameter ($PM_{2.5}$), also known as fine particles, pose the greatest risk to health. Whereas NO_2 is one of a group of highly reactive gases and adversely affects the human respiratory system.

The analysis is divided into two sections. In the first section, the trend of daily average (24-hour) concentrations of $PM_{2.5}$, PM_{10}, and NO_2 are studied before and during the lockdown. Considering 25 March (start of the lockdown) as a baseline, the average concentrations of air pollutants were studied from 25 February to 21 April to understand the temporal changes. The second section deals with the mapping of spatial changes in the levels of air pollution before and during the lockdown. The spatially interpolated maps of concentrations of air pollutants on 25 February and 21 April have been generated to estimate the spatial changes in air quality in the city.

Interpolation methods, in general, share the same basic mathematical foundation. They all estimate the value at an unmeasured location as a weighted average of the measurements at surrounding monitoring stations. They differ in their choice of sample weights and the surrounding stations (Xie et al., 2017). This study has used the Inverse Distance Weighting (IDW) method of spatial interpolation of air pollutants. In air pollution modelling the IDW method is popular and widely used among scholars (Hoek et al., 2002; Salam et al., 2005; Neupane et al., 2010; Chen et al., 2014). It is applied operationally by the Environmental Protection Agency (EPA) for generating real-time O3, PM_{10}, and Air Quality Index spatial predictions in nationwide scales (Deligiorgi and Philippopoulos, 2011). The value Z_0 at the unknown point is calculated as:

$$Z_0 = \frac{\sum_{i=1}^{N} Z_i \, d_i^{-n}}{\sum_{i=1}^{N} d_i^{-n}}$$

Where Z_0 is the estimation value of variable Z at point i, Z_i is the sample value in point i, d_i is the distance of the sample point to the estimated point, N is the coefficient that determines weight based on a distance, and n is the total number of predictions for each validation case.

The basic principle of the interpolation methods is based on the assumption that points closer to each other are highly correlated and more similar than those farther. This method will be used by a region in which there are enough sample points (at least 14 points) that are spatially dispersed all over the region (Burrough and McDonnell, 1998).

RESULTS AND DISCUSSION

Temporal trends of air pollution before and during the lockdown

There has been a significant change in the levels of $PM_{2.5}$ before and during the days of COVID-19 lockdown in Delhi (Table 1 and Fig. 2). All the stations in the city have recorded considerable lowering of $PM_{2.5}$ concentrations during the studied period. The average $PM_{2.5}$ concentrations in the city has reduced from 122.48 µg/m^3 on 25 February 2020 to 17.71 µg/m^3 on 21 April 2020. Moreover, at the beginning, all stations within the city have reordered $PM_{2.5}$ concentrations much higher than the standard (25 µg/m^3) set by the WHO. A noteworthy point here is that, on the last day of studied time, 29 stations out of the 35 have recorded $PM_{2.5}$ concentrations below the WHO standard.

The levels of PM_{10} concentration have strikingly reduced all over Delhi after the imposition of COVID-19 lockdown in the city (Fig. 2). Table 2 shows the declining levels of PM_{10} concentration before lockdown (25 February) and during lockdown (21 April). It should be noted that the average PM_{10} concentration in the city has remarkably reduced to 47.46 µg/m^3 on 21 April (during lockdown) from the critically higher level of 216.49 µg/m^3 on 25 February (before lockdown). Furthermore, the concentration of PM_{10} was recorded extremely higher than the WHO standards (50 µg/m^3) in all stations. These critical levels of PM_{10} in the city have reduced after the lockdown and 17 out of 31 stations have recorded the concentration below WHO standards.

Table 1 Details of the ground monitoring stations selected for the study and levels of $PM_{2.5}$, PM_{10} and NO_2 concentration before and during COVID-19 lockdown

ID	Station name, authority			Before COVID-19 lockdown (25 February 2020)			During COVID-19 lockdown (21 April 2020)		
		Lat	Lon	$PM_{2.5}$	PM_{10}	NO_2	$PM_{2.5}$	PM_{10}	NO_2
1	Alipur, Delhi - DPCC	28.7972	77.1331	110.12	206.45	52.61	52.61	52.61	13.4
2	Anand Vihar, Delhi - DPCC	28.6502	77.3027	88.52	209.39	57.14	20.88	81.18	33.55
3	Ashok Vihar, Delhi - DPCC	28.6909	77.1765	136.33	218.4	62.79	8	36.5	6.2
4	Aya Nagar, Delhi - IMD	28.4720	77.1329	72.75	154.72	24.52	36.88	34.54	12.2
5	Bawana, Delhi - DPCC	28.7932	77.0483	140.54	236.46	36.48	13.64	61.27	12.95
6	Burari Crossing, Delhi - IMD	28.7551	77.1607	NA	NA	NA	NA	NA	NA
7	Dr. K S Shooting Range, Delhi - DPCC	28.4997	77.2670	124.28	206.47	75.09	4.6	24.75	1.32
8	DTU, Delhi - CPCB	28.7499	77.1183	167.98	300.16	33.55	6.95	46.41	16.44
9	Dwarka-Sector 8, Delhi - DPCC	28.5720	28.5720	151.08	293.88	55.41	8.68	39.23	9.59
10	East Arjun Nagar, Delhi - CPCB	28.6561	77.2947	NA	NA	65.67	NA	NA	20.85
11	IGI Airport (T3), Delhi - IMD	28.5550	77.0844	92.32	191.91	27.62	7.68	28.81	NA
12	IHBAS, Dilshad Garden, Delhi - CPCB	28.6811	77.3047	103.69	NA	52.32	11.35	NA	10.06
13	ITO, Delhi - CPCB	28.6275	77.2437	177.24	238.21	28.17	133.46	128.89	18.67
14	Jahangirpuri, Delhi - DPCC	28.7296	77.1666	132	275.5	99.03	10.95	39.41	62.99
15	Jawaharlal Nehru Stadium, Delhi - DPCC	28.5828	77.2343	90.64	176.33	41.04	3	27.77	8.8
16	Lodhi Road, Delhi - IMD	28.5910	77.2280	84.02	175.81	31.17	59.93	73.8	22.58
17	MDCNS, Delhi - DPCC	28.6125	77.2373	117.83	204.93	59.93	7.35	22.85	8.84
18	Mandir Marg, Delhi - DPCC	28.6341	77.2004	90.78	204.65	54.45	14.05	38.3	26.14
19	Mathura Road, Delhi - IMD	28.6112	77.2401	100.97	234.49	45.94	6.94	39.63	15.52
20	Mundka, Delhi - DPCC	28.6823	77.0349	207.6	315.64	25.94	9	62	26
21	Najafgarh, Delhi - DPCC	28.6090	76.9854	119.46	164.06	27.54	46.24	154.73	NA
22	Narela, Delhi - DPCC	28.8548	77.0892	136.15	245.52	44.75	6.3	52.4	30.49
23	Nehru Nagar, Delhi - DPCC	28.5638	77.2608	147.88	241.8	34.14	7.72	29.5	11.88
24	North Campus, DU, Delhi - IMD	28.6889	77.2141	84.09	172	31.67	24.4	NA	12.88
25	NSIT Dwarka, Delhi - CPCB	28.6102	77.0378	134.63	NA	30.89	28.05	NA	11
26	Okhla Phase-2, Delhi - DPCC	28.5492	77.2678	133.5	238.27	48.61	8.5	33.1	10.58
27	Patparganj, Delhi - DPCC	28.6347	77.3045	106.91	144.35	29.41	4.18	27.09	8.72
28	Punjabi Bagh, Delhi - DPCC	28.6619	77.1241	146.86	212.91	41.87	7.67	37.36	13.67
29	Pusa, Delhi - DPCC	28.6376	77.1571	131.78	215.6	71.16	1.08	22.45	18
30	Pusa, Delhi - IMD	28.6340	77.1678	73.27	152.18	14.15	NA	NA	NA
31	R K Puram, Delhi - DPCC	28.5503	77.1851	98.73	219.36	54.32	5.75	21.2	7.55
32	Rohini, Delhi - DPCC	28.7382	77.0822	164.95	233.29	26.12	11.91	56.09	8.06
33	Shadipur, Delhi - CPCB	28.6510	77.1562	107.44	NA	86.72	13.21	NA	11.15
34	Sirifort, Delhi - CPCB	28.5505	77.2147	144.53	254.05	47.74	7.8	38.85	9.08
35	Sonia Vihar, Delhi - DPCC	28.7332	77.2495	104.68	183.97	47.29	6.2	35.3	17.27
36	Sri Aurobindo Marg, Delhi - DPCC	28.5563	77.2063	113.35	174.23	32.3	5	19	2.66
37	Vivek Vihar, Delhi - DPCC	28.6712	77.3176	124.02	199.71	43.5	9.5	64	16.41
38	Wazirpur, Delhi - DPCC	28.6975	77.1604	148.51	249.38	75.81	10.3	42.2	22.29
	Average			122.48	216.49	46.40	17.71	47.46	15.82

DPCC: Delhi Pollution Contro Committee, IMD: Indian Meteorological Department, CPCB: Central Pollution Control Board
N.A.= data not available for particular day
Source: Central Control Room for Air Quality Management, Delhi NCR

Table 1 illustrates the NO_2 concentrations in Delhi at various stations for two time periods i.e. before COVID-19 lockdown (25 February 2020) and during COVID-19 lockdown (21 April 2020). All the stations have recorded a pronounced reduction in NO_2 concentrations during the considered period. Though the majority of the stations have recorded NO_2 concentrations below the WHO standard (80 µg/m^3), the average 24-hour levels have further dropped from 46.40 µg/m^3 on 25 February to 15.82 µg/m^3 on 21 April. The trend of day to day NO_2 concentration level decrease before and during the lockdown in all the stations of Delhi has been presented by the line diagram (Fig. 2). There has been a remarkable lowering of NO_2 levels after 24 March when the COVID-19 lockdown started in India. It is also noticeable that the levels of NO_2 are considerably under control in the city compared to the critical levels of particulate matter.

It is indicative that the levels of air pollution declined gradually over the studied period with a steep fall from 25 March and reached historical low levels. Moreover, there is a notable difference between declining patterns of PM and NO_2 (Fig. 2). This difference can be justified with various reasons. The lockdown due to COVID-19 has strictly restricted all construction activities and movement of vehicles, which were responsible for previously higher levels of PM in Delhi (Kathuria, 2004; Taneja et al., 2016). Thus there is a sharp change in PM levels before and during the lockdown. However, as noted by Sikarwar and Chattopadhyay (2020) the levels of NO_2 concentrations in the city were already recorded below the standards and thus, showed a gradual decline during the lockdown.

Spatial changes in the level of air pollution before and during the lockdown

Before lockdown (25 February) the stations have recorded high levels of $PM_{2.5}$ and the most polluted areas of the city have $PM_{2.5}$ concentrations above 106 µg/m^3 (Fig. 3). Furthermore, our analysis found that the concentration was significantly high in the western part of the city but these concentration levels have trickled down remarkably during the lockdown (25 February)

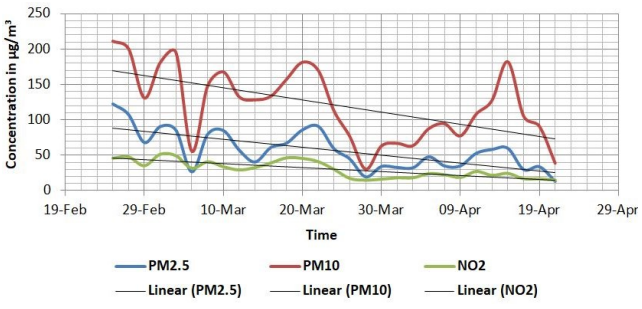

Fig. 2 Trend of $PM_{2.5}$, PM_{10}, and NO_2 concentrations [µg/m^3] before and during the lockdown in Delhi

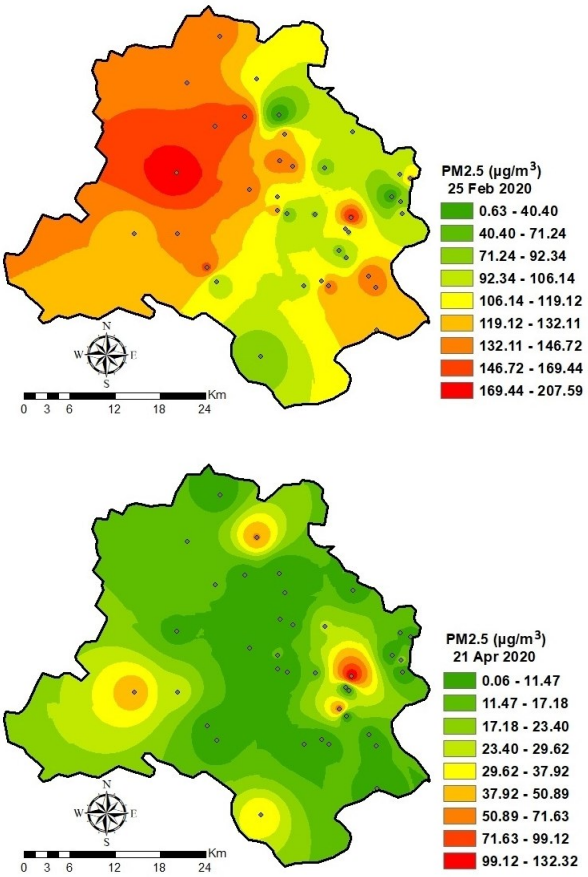

Fig. 3. Spatial concentrations of $PM_{2.5}$ in Delhi before (25 February 2020) (top) and during (21 April 2020) (bottom) COVID-19 lockdown.

when $PM_{2.5}$ concentrations were below 30 µg/m^3 in the maximum areas of the city.

The concentration of PM_{10} in the city before and during lockdown is presented with spatially interpolated surface maps too (Fig. 4). Before lockdown (25 February), the concentration of PM_{10} was critically high, when PM_{10} concentration was observed above 140 µg/m$_3$ in the most polluted areas of Delhi. The north-western and south-eastern parts exhibit the presence of an extreme level of PM_{10} in the air. However, these concentration levels have reduced significantly to lower levels during the lockdown (25 February) as the maximum area of the city has PM_{10} concentration below 56 µg/m^3.

The interpolated maps of NO_2 concentrations before and during the lockdown in Delhi clearly show that the NO_2 concentration in Delhi has reduced to notable levels after the implementation of lockdown in the city (Fig. 5). The analysis shows, that before the lockdown, mainly the eastern part of the city had higher concentrations of NO_2, which further declined during the lockdown. It was also found that the southern part of the city has experienced better air quality in terms of NO_2, during the lockdown. However, the levels of NO_2 concentration remained higher in the northern parts of the city.

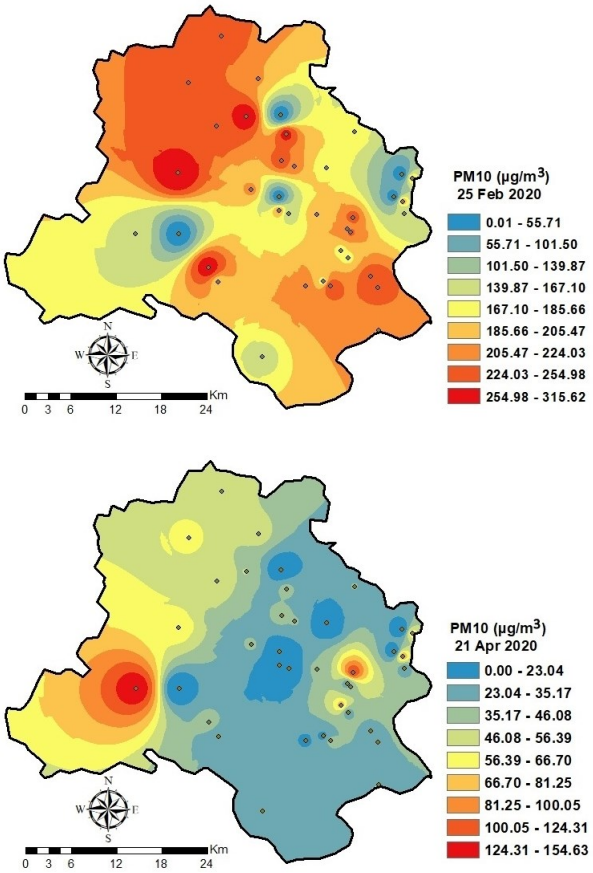

Fig. 4. Spatial concentrations of PM_{10} in Delhi before (25 February 2020) (top) and during (21 April 2020) (bottom) COVID-19 lockdown

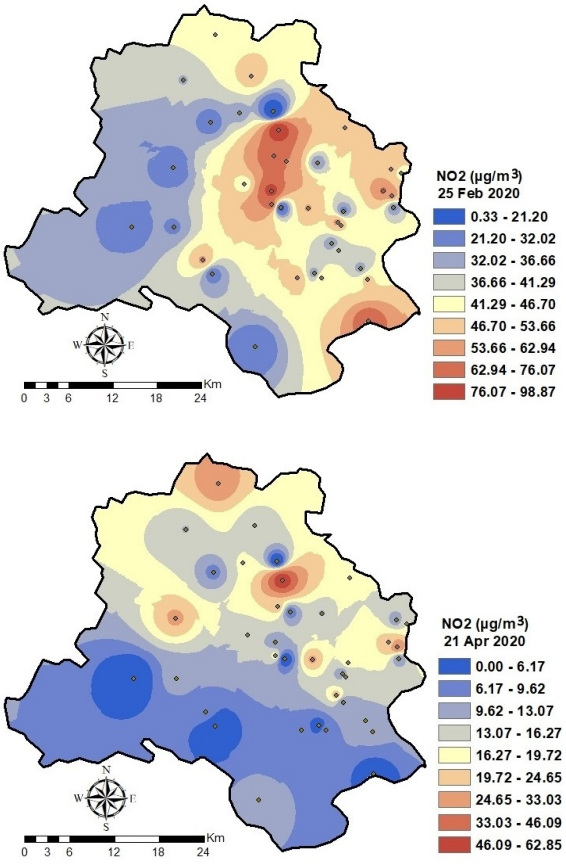

Fig. 5. Spatial concentrations of NO_2 in Delhi before (25 February 2020) (top) and during (21 April 2020) (bottom) COVID-19 lockdown

CONCLUSIONS

Since many Indian metro cities have been in the list of the world's most polluted cities, a sudden significant improvement in the air quality of Delhi has international relevance for environmental policies. Lockdown due to COVID-19 in various parts of the world has provided an opportunity to measure human impact on the natural environment particularly in big cities. When urban mega hubs have been running continuously for economic development without considering the limits of natural resources, measures like temporary lockdown may emerge as an effective solution to control environmental imbalance.

With the use of the IDW method of spatial interpolation, the study estimated concentrations of $PM_{2.5}$, PM_{10}, and NO2 before and during COVID-19 lockdown in Delhi. It is found that the lockdown in the city has positively impacted the air quality. The results reveal that just after one month of the lockdown the reductions in $PM_{2.5}$, PM_{10}, and NO_2 concentrations were by 93%, 83%, and 70% respectively. Consequently, the levels of air pollution are historically low during the lockdown when compared to the levels estimated in previous studies on Delhi (Kumar and Foster, 2009; Dholakia et al., 2013; Rizwan et al., 2013). Considering the critically degraded air quality for decades and higher morbidity and mortality rates due to unhealthy air, the improvement in air quality due to lockdown may result as a boon for the better health of the city's population. This temporary improvement in the air of the capital city gives a positive indication of another chance to mitigate the damage we have done to the environment. Therefore, the study should be considered as a useful supplement to the regulatory authorities that may lead to reconsider the current plan and policies to combat degraded air quality in the city.

ACKNOWLEDGMENTS

We are thankful to the Central Control Room for Air Quality Management, Delhi for providing free data for the studied pollutants.

References

Alvarez, F.E., Argente D., Lippi, F. 2020. A simple planning problem for covid-19 lockdown. National Bureau of Economic Research Working Papers. 26981. DOI: 10.3386/w26981 Online available at: https://ideas.repec.org/p/nbr/nberwo/26981.html

Asher, C.B. 2000. Delhi Walled: Changing Boundaries. In: Tracy, J. (ed.) City Walls: The Urban Enceinte in Global Perspective. Cambridge University Press, Cambridge, 247-281.

Burrough, P.A., McDonnell, R.A. 1998. Principles of Geographic Information Systems. Oxford University Press, Oxford. Online available at: https://trove.nla.gov.au/work/23430924

Chandramouli, C., General, R. 2011. Census of India 2011. Provisional population totals. Government of India, New Delhi

Chen, G., Li, J., Ying, Q., Sherman, S., Perkins, N., Sundaram, R., Mendola, P. 2014. Evaluation of observation-fused regional air quality model results for population air pollution exposure estimation. *Science of the Total Environment.* 485, 563-574. DOI: 10.1016/j.scitotenv.2014.03.107

Chowdhury, S., Dey, S., Guttikunda, S., Pillarisetti, A., Smith, K.R., Di Girolamo, L. 2019. Indian annual ambient air quality standard is achievable by completely mitigating emissions from household sources. *Proceedings of the National Academy of Sciences*. 116, 10711-10716. DOI: 10.1073/pnas.1900888116

Deligiorgi, D., Philippopoulos, K. 2011. Spatial interpolation methodologies in urban air pollution modeling: application for the greater area of metropolitan Athens, Greece. *Advanced Air Pollution*. 17, 341-362. DOI: 10.5772/17734

Dholakia, H.H., Purohit, P., Rao, S., Garg, A. 2013. Impact of current policies on future air quality and health outcomes in Delhi, India. *Atmospheric Environment*. 75, 241-248. DOI: 10.1016/j.atmosenv.2013.04.052

Dutheil, F., Baker, J.S., Navel, V. 2020. COVID-19 as a factor influencing air pollution?. *Environmental Pollution*. 263, 114466. DOI: 10.1016/j.envpol.2020.114466

Environmental Protection Agency. 2020. Particulate Matter (PM) Basics. Online available at: https://www.epa.gov/pm-pollution/particulate-matter-pm-basics

Goyal, P. 2003. Present scenario of air quality in Delhi: a case study of CNG implementation. *Atmospheric Environment*. 37(38), 5423-5431. DOI: 10.1016/j.atmosenv.2003.09.005

Gujrar, B.R., Van Aardenne, J.A., Lelieveld, J., Mohan, M. 2004. Emission estimates and trends (1990–2000) for megacity Delhi and implications. *Atmospheric Environment*. 38, 5663-5681. DOI: 10.1016/j.atmosenv.2004.05.057

Gujrar, B.R., Ravindra, K., Nagpure, A.S. 2016. Air pollution trends over Indian megacities and their local-to-global implications. *Atmospheric Environment*. 142, 475-495. DOI: 10.1016/j.atmosenv.2016.06.030

Hoek, G., Brunekreef, B., Goldbohm, S., Fischer, P., van den Brandt, P.A. 2002. Association between mortality and indicators of traffic-related air pollution in the Netherlands: a cohort study. *The lancet*. 360, 1203-1209. DOI: 10.1016/S0140-6736(02)11280-3

Inoue, H., Todo, Y. 2020. The propagation of the economic impact through supply chains: The case of a mega-city lockdown to contain the spread of COVID-19. *Covid Economics*. 2, 43-59. DOI: doi.org/10.1371/journal.pone.0239251

Kampa, M., Castanas, E. 2008. Human health effects of air pollution. *Environtal Pollution*. 151, 362-367. DOI: 10.1016/j.envpol.2007.06.012

Kucharski, A.J., Russell, T.W., Diamond, C., Liu, Y., Edmunds, J., Funk, S., Eggo, R.M., Sun, F., Jit, M., Munday, J.D., Davies, N. 2020. Early dynamics of transmission and control of COVID-19: a mathematical modelling study. *The lancet infectious diseases*. 20, 553-558. DOI: 10.1016/S1473-3099(20)30144-4

Kathuria, V. 2004. Impact of CNG on vehicular pollution in Delhi: a note. *Transportation Research Part D: Transport and Environment*. 9, 409-417. DOI: 10.1016/j.trd.2004.05.003

Kumar, N., Foster, A.D. 2009. Air quality interventions and spatial dynamics of air pollution in Delhi and its surroundings. *International journal of environment and waste management*. 4, 85-111. DOI: 10.1504/IJEWM.2009.026886

Li, L., Li, Q., Huang, L., Wang, Q., Zhu, A., Xu, J., Liu, Z., Li, H., Shi, L., Li, R., Azari, M. 2020. Air quality changes during the COVID-19 lockdown over the Yangtze River Delta Region: An insight into the impact of human activity pattern changes on air pollution variation. *Science of the Total Environment*. 11, 139282. DOI: 10.1016/j.scitotenv.2020.139282

Mahato, S., Pal, S., Ghosh, K.G. 2020. Effect of lockdown amid COVID-19 pandemic on air quality of the megacity Delhi, India. *Science of the Total Environment*. 730, 139086. DOI: 10.1016/j.scitotenv.2020.139086

Muhammad, S., Long, X., Salman, M. 2020. COVID-19 pandemic and environmental pollution: a blessing in disguise?. *Science of the Total Environment*. 728, 138820. DOI: 10.1016/j.scitotenv.2020.138820

Nagpure, A.S., Gurjar, B.R., Kumar, V., Kumar, P. 2016. Estimation of exhaust and non-exhaust gaseous, particulate matter and air toxics emissions from on-road vehicles in Delhi. *Atmospheric Environment*. 127, 118-124. DOI: 10.1016/j.atmosenv.2015.12.026

Neupane, B., Jerrett, M., Burnett, R.T., Marrie, T., Arain, A., Loeb, M. 2010. Long-term exposure to ambient air pollution and risk of hospitalization with community-acquired pneumonia in older adults. *American journal of respiratory and critical care medicine*. 181,47-53. DOI: 10.1164/rccm.200901-0160OC

Rizwan, S.A., Nongkynrih, B., Gupta, S.K. 2013. Air pollution in Delhi: its magnitude and effects on health. *Indian journal of community medicine: official publication of Indian Association of Preventive & Social Medicine*. 38, 4. DOI: 10.4103/0970-0218.106617

Salam, M.T., Millstein, J., Li, Y.F., Lurmann, F.W., Margolis, H.G., Gilliland, F.D. 2005. Birth outcomes and prenatal exposure to ozone, carbon monoxide, and particulate matter: results from the Children's Health Study. *Environmental Health Perspectives*. 11, 1638-1644. DOI: 10.1289/ehp.8111

Satyendra, T., Singh, R.N., Shaishav, S. 2013. Emissions from crop/biomass residue burning risk to atmospheric quality. *International Research Journal of Earth Sciences*. 1, 1-5.

Sharma, S., Zhang, M., Gao, J., Zhang, H., Kota, S.H. 2020. Effect of restricted emissions during COVID-19 on air quality in India. *Science of the Total Environment*. 728, 138878. DOI: 10.1016/j.scitotenv.2020.138878

Sikarwar, A., Chattopadhyay, A. 2020. Analyzing Population and Land Use Change: Selected Case Studies of Indian Metropolitan Cities. Springer Nature, Singapore. ISBN 978-981-15-5036-2

Singh, R.K., Chakraborty, D. 2020. World's Dirtiest Air Gets Cleaner After India's Lockdown. Bloomberg-Quint. Online available at: https://www.bloombergquint.com/

Taneja, S., Sharma, N., Oberoi, K., Navoria, Y. 2016. Predicting trends in air pollution in Delhi using data mining. In 2016 1st India International Conference on Information Processing (IICIP). 1-6. DOI: 10.1109/iicip.2016.7975379

United Nations. 2018. Revision of World Urbanization Prospects. United Nations, New York. ISBN: 978-92-1-148319-2

Wang, P., Chen, K., Zhu, S., Wang, P., Zhang, H. 2020. Severe air pollution events not avoided by reduced anthropogenic activities during COVID-19 outbreak. *Resources, Conservation and Recycling*. 158, 104814. DOI: doi.org/10.1016/j.resconrec.2020.104814

World Health Organization. 2016. WHO global urban ambient air pollution database (update 2016). Geneva, Switzerland, WHO. Online available at: https://www.who.int/airpollution/data/cities-2016/en/

World Health Organization. 2020. Coronavirus disease (COVID-2019) situation reports. Online available at: https://www.who.int/emergencies/diseases/novel-coronavirus-2019/situation-reports

Xie, X., Semanjski, I., Gautama, S., Tsiligianni, E., Deligiannis, N., Rajan, R.T., Pasveer, F., Philips, W. 2017. A review of urban air pollution monitoring and exposure assessment methods. *ISPRS International Journal of Geo-Information*. 6, 389. DOI: doi.org/10.3390/ijgi6120389

Zhu, N., Zhang, D., Wang, W., Li, X., Yang, B., Song, J., Zhao, X., Huang, B., Shi, W., Lu, R., Niu, P. 2020. A novel coronavirus from patients with pneumonia in China, 2019. *New England Journal of Medicine*. 382, 727-733. DOI: 10.1056/NEJMoa2001017

sciendo

Journal of Environmental Geography 13 (3–4), 34–43.

DOI: 10.2478/jengeo-2020-0010
ISSN 2060-467X

CHARACTERISTICS OF WINTER URBAN HEAT ISLAND IN BUDAPEST AT LOCAL AND MICRO SCALE

Huawei Li[1, 2*], Guifang Wang[1], Sándor Jombach[1*]

[1] Department of Landscape Planning and Regional Development, Faculty of Landscape Architecture and Urbanism, Szent István University, Villányi út 35-43, 1118 Budapest, Hungary
[2]Department of Landscape Architecture, College of Landscape Architecture and Art, Henan Agricultural University, Nongye Rd 63, 450002 Zhengzhou, China
*Corresponding author, e-mail: Li.Huawei@phd.uni-szie.hu; Jombach.Sandor@szie.hu
Research article, received 15 September 2020, accepted 29 October 2020

Abstract

Most of the urban heat island (UHI) researches focused on the phenomenon in summer. They mainly studied the causes, different functional areas, and possible mitigation measures to reduce the high temperature in urban areas. However, UHI also exists in winter, but there are a limited number of studies on winter UHI. The characteristics and causes of UHI in winter have not been received much attention or consideration yet. This study aims to characterize the UHI feature in winter in Budapest, Hungary, based on the analysis of land surface temperature (LST) in relation to the factors of elevation, slope exposure, residential type, and snow coverage. Five different Landsat images in the winter season were applied to detect the surface temperature; besides, pictures of the thermal camera at a micro-scale were also used. Results showed that UHI intensity was not strong in winter; built-up areas were warmer than other urban areas. Topography was one of the significant factors affecting the surface temperature in winter. The surface temperature of the hills (300 m asl) was lower than that of the lowlands (below 120 m asl). The south-facing slopes and south oriented buildings were warmer than north-facing slopes and buildings oriented to the north. Areas with snow coverage had a lower temperature than no snow coverage areas. These findings could give general guidance for further UHI research, urban planning as well as landscape design.

Keywords: UHI, Surface temperature, LST, Topography, Slopes, Aspects, Snow, Influencing factor

INTRODUCTION

Urban heat island (UHI) is a phenomenon that is recognized as the temperature is higher in highly urbanized areas than its surroundings (Oke, 1973, 1982, 1987). This kind of local temperature difference had caused serious environmental problems worldwide. Increased energy consumption, modified natural habitats, endangered human health and well-being are the symptoms of urban heat island (UHI). This phenomenon was first discovered and proposed by Luke Howard in 1818 (Howard, 1818). He analyzed the records of temperature in London and recognized the special effect of urban areas on the local climate. Today we are aware of the general urban heat island effects in summer all over the World. The heat island can be measured by land surface temperature and by air temperature as well (Deilami et al., 2018). The land surface temperature (LST) is the main approach to map the UHI phenomenon based on satellite images covering large areas on a regional scale. Air temperature is measured by weather stations collecting data of exact predefined locations. At the same time, connections between surface and air temperature are also a research concentration.

Most studies on UHI were focused on the summer (Kolokotroni and Giridharan, 2008; Middel et al., 2012; Zhang et al., 2017a; Lam and Lau, 2018;) because this UHI effect is significant during the hot season, the radiation of the solar energy makes the surface stored more heat during the daytime. Thus studies showed that surface urban heat island (SUHI) is related to the surface albedo and heat transfer by the coverage materials (Bhattacharya et al., 2009; Erell et al., 2014). For instance, impervious surfaces such as roads and concrete surfaces absorb more heat than green spaces and water areas. During the night, the buildings and other impervious surfaces in the urban areas release the heat stored at daytime (US EPA, 2014; Zhang et al., 2017b), as a consequence, making the UHI intensity larger than in the day. Studies also investigated the impact factors related to UHI effects, such as urbanization (Chapman et al., 2017; Mathew et al., 2017), urban form (Li et al., 2012), landscape structure (Li et al., 2011), impervious surfaces percentage (Henits et al., 2017), green space coverage (Oliveira et al., 2011; Kong et al., 2014), water surface and geography factors (Mathew et al., 2017; Cai et al., 2018), but most of the research chose the period in the summer season. With the development of satellite image processing, the winter season UHI could be documented as well. However, there are a limited number of articles dealing with the winter UHI and related effects.

For the effect of NDVI and surface temperature in wintertime, a study showed that lower temperature was observed in the high vegetated area at daytime in Tokyo's urban areas in 1990. Based on NDVI analysis,

densely vegetated areas have lower temperatures in winter in the urban areas at night. On the contrary, the densely vegetated areas appeared with higher temperatures in the suburban areas in the same conditions. The relationship between vegetation and temperature was not significant in the urban area at day time, but the high vegetated area tends to lower temperature in suburban areas (Kawashima, 1990). In further research, Kawashima et al. (2000) employed the Automated Meteorological Data Acquisition System (AMeDAS) to obtain air temperature in winter. His research group found that the value of NDVI has a sensitive relationship, but no regulation with the air temperature by linear regression analysis, and they also found surface temperature can explain 80% of the observed variation in air temperature. The urban heat island exists in summer and winter (Zhang and He, 2007; Mathew et al., 2017). The distribution of land surface temperature (LST) is also in relation to the city structure. The studies showed that the variation in the wintertime is less strong compared with other seasons. However, land cover types and LST distribution have a stronger relationship in all seasons (Liu and Weng, 2008). In London, the winter UHI investigation indicated that most outdoor temperature changes are dominantly caused by climate factors (like wind velocity, sky condition) and not the on-site variables (Giridharan and Kolokotroni, 2009). A similar result appeared in Shanghai (China): UHI intensity was relatively weak during the winter period compared to summer and springtime during 1997 and 2008 (Li et al., 2012).

In the wintertime, snow is one of the significant factors which affect LST. The high albedo of snow changes the surface radiation balance; its low thermal diffusivity insulates the local climate (Hinkel et al., 2003; Westermann et al., 2012; Lokoshchenko, 2014). Previous research showed that the snow cover area correlated with surface brightness temperature in California, USA (Yin and Zhang, 2014). When the local surface was covered by snow, the snow area could increase rapidly in snowy weather. The brightness temperature was a good indication of the presence of snow. However, the study revealed that when the snow was more than 0.5 m deep, or the snow was beginning to melt, the brightness temperature had less useful information for LST.

Another investigation demonstrated the existence of UHI in Barrow, Alaska (USA). It used soil and air temperature from the temperature records, and the peak UHI magnitude (UHIM) appeared in the late evening and the early morning. The average temperature in the urban area was 2.2 °C warmer than the hinterland. UHI magnitude generally increased with decreasing air temperature in winter, reflecting anthropogenic heat's input to maintain interior building temperatures (Hinkel et al., 2003). However, in wintertime, urban heat island gave an effect on species migration more extended in Central Europe (Sachanowicz et al., 2018). The growing detection of bat species' winter occurrence (Pipistrellus nathusii, Chiropter asp.) has coincided with an increase in mean winter temperatures and urban warming. Recently recorded new wintering areas for these species, mainly in Central European cities, have largely extended its wintering distribution to the northeast due to the winter urban heat island effect. The orientation of buildings on the streets raised some design challenges, especially considering solar and wind directions (Erell et al., 2014). The building orientation to the sun affects the amount of solar radiation absorbed. A Greek study found that streets on the east-west axis were less exposed to solar radiation (Andreou, 2014). So it could be interesting to do further step on the orientation and aspect field impact on the surface temperature at the city level.

According to the UHI studies made in Hungary, the strongest UHI intensity occurs in the urban center during the heating season. This phenomenon was not dependent on heating, but the season and weather characteristics (Unger and Makra, 2007). Winter UHI existed because of the heating and different surface materials of buildings, and the materials of buildings have low heat capacity. The water surface was warmer than other land cover types in winter (Oláh, 2012). Budapest downtown's annual mean temperature was 1.2 °C higher than outside the city, and the peak month was in January (Probáld, 2014). Due to the meteorological conditions in winter (except February) and autumn, the UHI phenomenon appeared less intensive than that of summer and spring in Debrecen (Hungary) based on long-term data (László et al., 2016). The analysis of the relationship between the SUHI intensity and the Local Climate Zone (LCZ) classes for the Budapest study showed that the SUHI intensity variability was generally greater in summer than in winter, which was caused by the difference in solar radiation in these two different seasons (Dian et al., 2020).

From UHI literature reviews, we found that most studies focused on UHI during summertime, as this is when temperature differences are clear and can be easily understood. It can be quantified by surface and air measurements but surveys in winter season UHI are not so current and widespread. This paper intends to characterize the surface urban heat island phenomenon in Budapest in the winter season, from the city scale to the local scale. Some part of our research was based on satellite images, similar to previous research about summer urban heat island in Budapest (Gábor and Jombach, 2009). We used satellite images and thermal camera surveys to illustrate surface temperature maps and visualize the on-site surface temperature in different site locations.

This study aims to analyze the characteristics of the land surface temperature (LST) of Budapest in winter. The general goal was to discover winter heat island characteristics of Hungary's capital city based on surface temperature analysis by satellite images and field surveys. Our study mainly focused on the following questions:

1) What are the general winter urban heat island (UHI) characteristics?
2) How do elevation, slope aspect and building orientation modify surface temperature?
3) How does snow cover modify the land surface temperature (LST) of Budapest?

STUDY AREA

Budapest is the capital city of Hungary, located in the central part of the country. The city had an estimated population of 1.75 M inhabitants and has a land area of about 525 km^2. Budapest's climate is moderately continental based on Köppen-Geiger climate classification, which has relatively cold winters and warm summers (Beck et al., 2018). According to the long-term observation data record from 1991-2019 (OMSZ, 2020), the mean temperature in Budapest is 11.3 ℃. The warmest month (with the highest average high temperature) is July (26.7°C). The month with the lowest average high temperature is January (2.9°C).

METHODS AND MATERIALS

Digital satellite images, thermal camera images, and an elevation model were used. The key methods were land surface temperature calculation with a combination of field surveys, GIS analysis, and statistical analysis. The measured temperature data is mainly LST from satellite imagery. Additionally, we used a digital elevation model to analyze the slopes and aspects to explore different temperature characteristics based on topography. GIS software is used to retrieve the surface temperature from Landsat 8 satellite images. The sample sites of different land-use types were selected based on Google's very high resolution (VHR) satellite image and field survey experience. Zonal statistical tools summarized temperature. At the same time, Excel statistical tools were used to analyze and show the outcomes. Field photography and thermal images were also applied to illustrate the results.

Satellite data resource

In this study, five Landsat 8 satellite images were used (Table 1). These were chosen and downloaded from the USGS (https://earthexplorer.usgs.gov/). The images focus on the peak winter from November to March. Budapest's heating season is mostly from mid of October to mid of April, and this period is represented by leafless landscape scenery. The images were prepared on sunny days around 10:33 (Central European Time) and these have almost no cloud coverage, which means that the results will show the typical situation of bright, sunny winter days. The only image with partial snow coverage (06.01.2017) was used for snow cover effect analysis.

Retrieval of land surface temperature

The land surface temperature was calculated by GIS-related software from Landsat 8 satellite images. In this study, QGIS and ArcGIS software was used to calculate LST values. The process mainly includes five steps from the satellite image to the LST map based on the radiative transfer equation (RTE) method (Li et al., 2020).

1) Conversion to "Top of atmosphere Radiance"
2) Conversion to "Top of Atmosphere Brightness Temperature"
3) Calculation of "Proportion of Vegetation"
4) Calculation of "Land Surface Emissivity" (LSE)
5) Retrieval "Land Surface Temperature" (LST).

For the analysis, we used single land surface temperature maps (based on all images of Table 1) and Budapest's average LST map.

Digital elevation model

To analyze topographic characteristics and define the significant southern and northern slopes, we used the SRTM digital elevation model. The model was downloaded from the website of USGS. The spatial resolution is 30 m. For the temperature analysis related to the elevation, we identified areas above 300 m asl as "hills," while the areas below 120 m were identified as "lowlands". For the slope analysis based on the SRTM model, we selected slopes steeper than 10%. Based on aspect analysis, we could select the south-facing slopes and the north-facing slopes separately. The sample sites were the largest 27 contiguous areas; each of them was larger than 5.0 hectares.

Thermal camera imaging

We used thermal imaging to illustrate surface temperature in the city and the instrument was the "Seek thermal Pro" camera with a 320 x 240 resolution thermal sensor. It is portable, lightweight, and easy-to-use, based on the Seek application on a smartphone. The method included a parallel use of real photography in the field. An illustration can be shown by comparing thermal and real images (Fig. 1)

Table.1 Landsat images used to estimate land surface temperature

Date	Satellite types	Scale
27.11.2013	Landsat 8 OLI-TIRS	Full Budapest coverage
15.02.2014	Landsat 8 OLI-TIRS	Full Budapest coverage
18.02.2015	Landsat 8 OLI-TIRS	Full Budapest coverage
06.01.2017 *	Landsat 8 OLI-TIRS	Full Budapest coverage
25.01.2018	Landsat 8 OLI-TIRS	Full Budapest coverage

*The satellite image was only used for snow-cover analysis

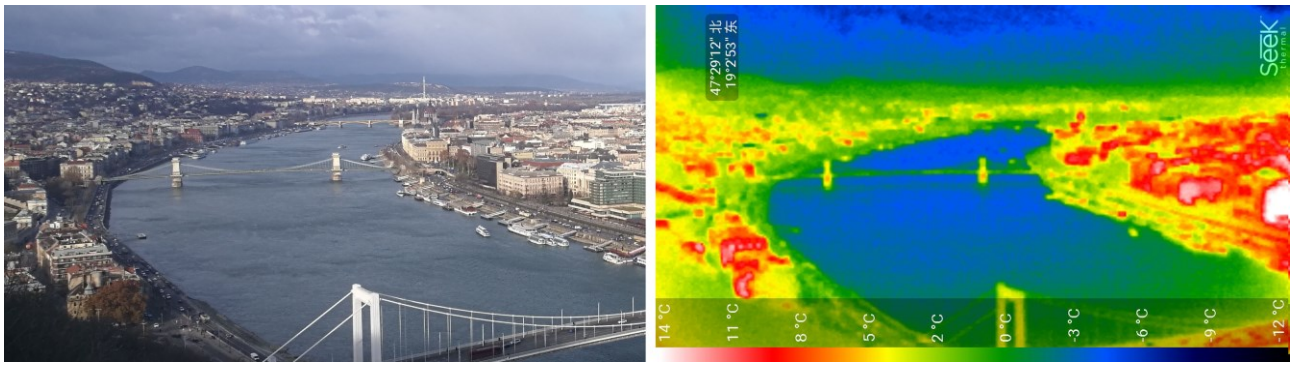

Fig. 1 The real image and the thermal image showing the Budapest city center's surface temperature measured by the Seek Pro heat camera from Gellért hill (at 12:50 on 28. 12. 2018). The thermal image and the real image were prepared simultaneously so that the areas of different temperatures could be recognized. The thermal image includes the legend of temperature in Celsius degree. A diverse colour scale can be set with the software. The analysis of thermal images in the article was assisted by the combined use of real photo contours.

Statistical analysis

The zonal statistical analysis was applied to get the mean LST values from the map (Chen et al., 2006). By using this tool, a mean LST was extracted from all corresponding pixels. According to a previous study (Woodcock and Strahler, 1987), the optimal spatial resolution to capture spatial patterns using remotely sensed imagery was approximately half to three-quarters of the object dimension's size in the scene. A previous study showed that 60×60 m spatial resolution is approximately the optimal spatial resolution in analyzing the scale effect on monitoring UHI (Chen et al., 2006). Therefore, we performed analyses at the finest spatial scale as the data allowed, which was appropriate to capture UHI's spatial features and relevant land-use types. The sample sites we selected were all bigger than 5 hectares; this means that they were much higher above the limit that previous research.

RESULTS AND DISCUSSION

Our results are grouped and discussed according to the general goal and the questions we aimed to answer. Thus we interpreted the results of Budapest in general and for its districts. Then we analyzed the influence of topography and snow coverage on temperature changes.

General winter UHI characteristics in Budapest

We prepared five separate land surface temperature maps (based on the images in Table 1.) and an LST average map for Budapest (Fig.2) representing the whole city region. From this winter average LST map (Fig. 2) the following general outcomes we listed:
The urban heat island existed in Budapest in the analyzed winter days. The winter LST map demonstrated that the temperature was decreasing from urban centers to non-urbanized areas. Although the differences were not significant, the temperature in wintertime was generally low. According to the average map, it varied between -2.7℃ and 7.6℃.

Buda side was generally colder than the Pest side. The western forested and hilly parts in Buda were cooler than the densely urbanized Pest side. We compared the mean LST of different districts in Budapest (Fig. 3a). The 23 districts of the city had a surface temperature above 0.0 ºC. The XII district was the coldest, being 1.1 ℃ on average. The warmest districts were the VII and IX districts, which indicated up to 3.3 ℃ (Fig. 3b). The LST's spatial characteristics reflect that the warmer districts were located in the densely built-up central and south-eastern areas and airport area, while the colder ones are closer to the "semi-natural" areas (i.e., forests, hills) at west.

Warmer spots were mostly dispersed within build-up areas. Spatial distribution of surface temperature based on field thermal photo from aerial photography on Fig. 1, showed similarly that the temperature in built-up area patches was the highest, sometimes reaching peaks like 14℃ in the high resolution. The city's warmest elements were the airport, logistical buildings, huge store and parking areas, garages, and railway stations, which had generally valued above 5 ℃ on average. The urban parks, forests, and other woodland areas were usually colder than the city's average temperature. The Densely built-up residential areas downtown had a higher surface temperature than the suburban-style family house dominant garden cities.

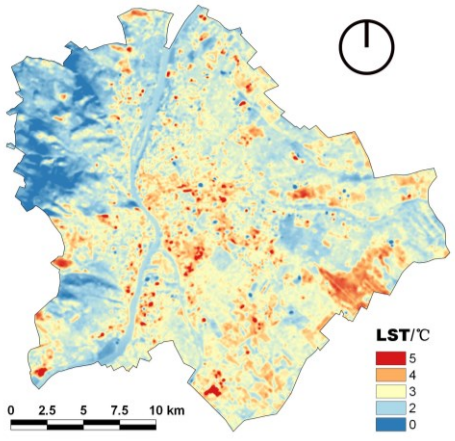

Fig. 2 The average winter land surface temperature (LST) map (based on five images in years 2013-2018) in Budapest

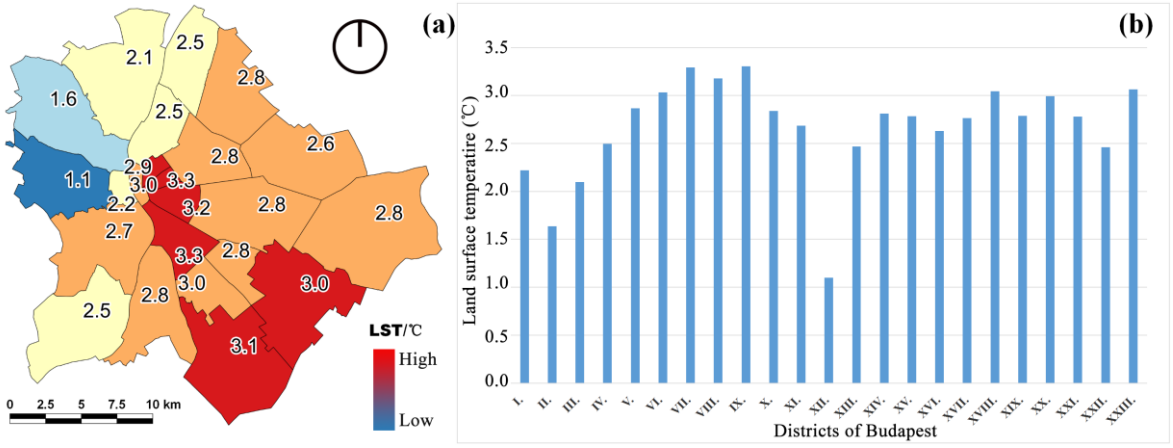

Fig. 3 The mean land surface temperature (LST) map of the 23 districts in Budapest (a) and the temperature differences between the districts (b).

The topographic differences seemed to influence LST depending on the aspect of slopes and sun angle. This phenomenon, we decided to analyze in detail in some selected sampling areas.

Elevation and aspect influence on LST

Based on the SRTM digital elevation data, we analyzed how the elevation and aspect influence the land surface temperature (Fig. 4a). By comparing the average surface temperature of the two elevation classes (above 300 m asl and bellow 120 m asl), it could be seen that the higher the altitude, the lower the surface temperature is. It could be concluded in the topographical division of Budapest that the surface temperature in the lowland was higher. The difference between the two elevation classes was 2.06 °C on average (Fig. 4b). The single image analysis showed that the lowest temperatures could be detected in the hills (below -4 ℃) while the highest was in the lowlands (sometimes above 10 °C). In summary, our results showed that hills were more than 2.0 °C colder than the lowlands in Budapest.

The surface temperature is directly related to the sunlight, the absorption, and the heat storage capacity of the surface. Therefore, the slope orientation (exposure) will inevitably affect the distribution of surface temperature. Comparing the aspect data extracted from the SRTM digital elevation model can be seen in Fig. 5. The temperature in the southern slope surface is every case higher than any slope on the north side. In Sas hill and Gellért hill, the northern slope was around 1 ℃, and the south slopes were around 4 ℃ on average. The temperature difference, on average, was 2,7 ℃. We could sentence that the southern slopes of hills were more than 2 ℃ higher than the northern slopes. The high-resolution field survey with the thermal camera made the phenomenon even more obvious as the extreme temperatures of different slope aspects and building orientations show this in more detail (Fig. 6 and 7). Concluding the results of satellite image analysis and thermal image analysis, it could be stated that during the winter season, a special kind of heat island could be determined in Budapest due to low sun angle. This kind of vertical factor on UHI can be called the "vertical heat island". The sun's vertical elements are illuminated by the sun mostly from the side, so the heat island shows up by slopes, walls, facades significantly, which means that it can be measured better from the field than from the air. Therefore, it is also recommended to have field surveys with thermal camera applications.

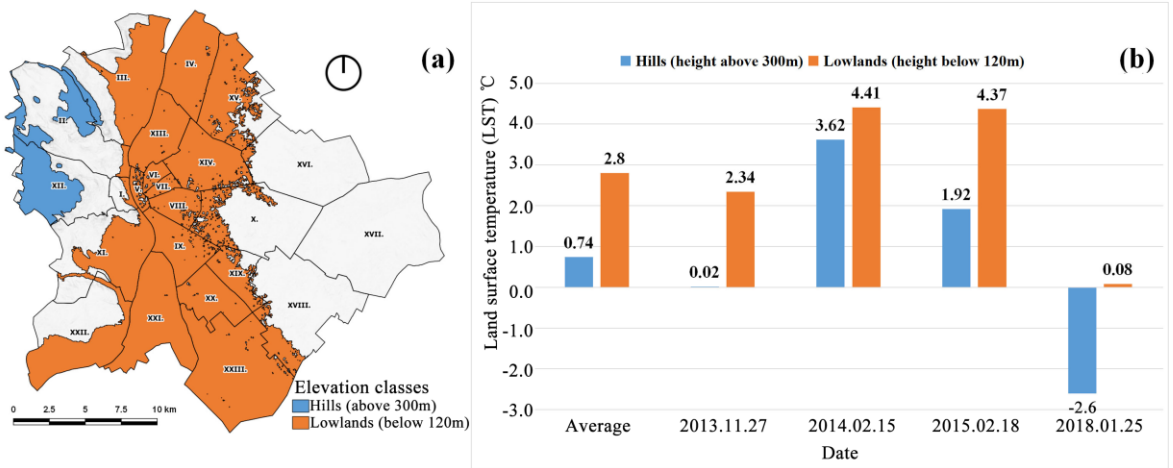

Fig. 4 Mean land surface temperature (LST) of hills and lowlands (a) in Budapest and comparison histogram (b).

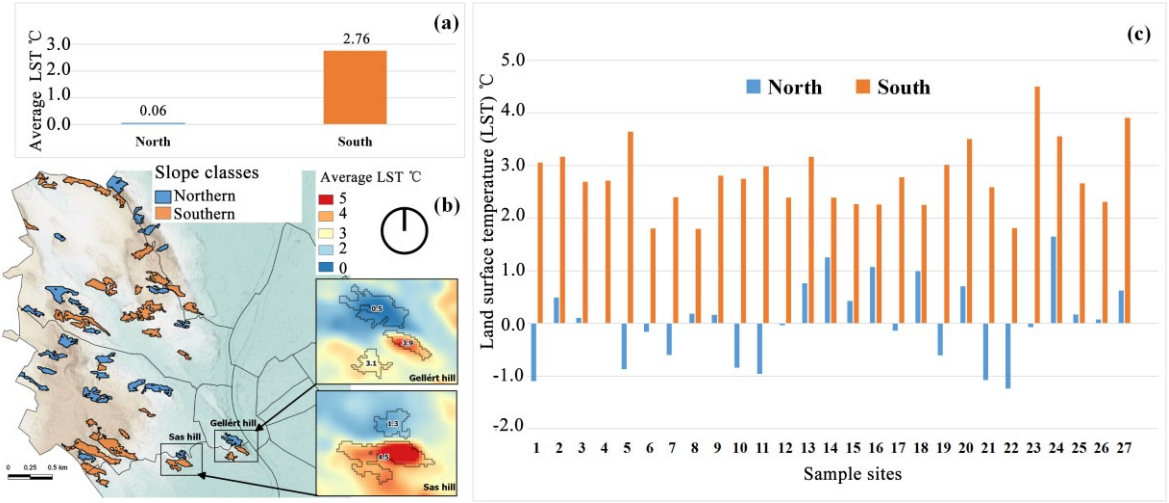

Fig. 5 LST of the two exposure types (a), spatial distribution of selected sites (b) and the average LST of sample sites (c)

The Buda Castle complex showed that the groups of buildings facing different directions could result in a temperature difference of 10 °C.

Relationship between LST and snow cover

To analyze snow cover's cooling effect, we selected a particular image of the year 2017 that had partial snow coverage. This image had snow cover in the southeast and no snow cover on the northwest (taken at 10:33 on 06. 01. 2017). Fig. 8a clearly shows the boundary that divided the city into two parts: areas with snow-cover and without snow-cover. We compared the differences between these two parts. The LST map in Fig. 8b shows that the snow-covered area's surface temperature was lower than those without snow cover. These could lead to similar conclusions like other previous studies (Hinkel et al., 2003; Westermann et al., 2012; Lokoshchenko, 2014). Due to the high albedo of the snow surface, those areas had less heat absorption and storage.

To further explore the influence of snow cover on the surface temperature, we selected sample sites to comparison of the different land-use types. We selected 40 sites representing the two most frequent land-use types of the northeastern suburban area of the XV., XVI., and XVII. Districts (Fig.9):

- Garden community (a type of residential area, dominated by family houses and gardens),
- Arable land (plowland mostly with no vegetation in winter, bare soil)

We selected ten snow-covered sites within the residential areas with gardens and another ten sites without snow coverage. Each site was bigger than 5 hectares but smaller than 20 hectares. Our results show that the snow-covered garden community blocks' temperature was lower than the no-snow covered areas (Fig. 10), as the average temperature difference was 2.66 °C on the given day.

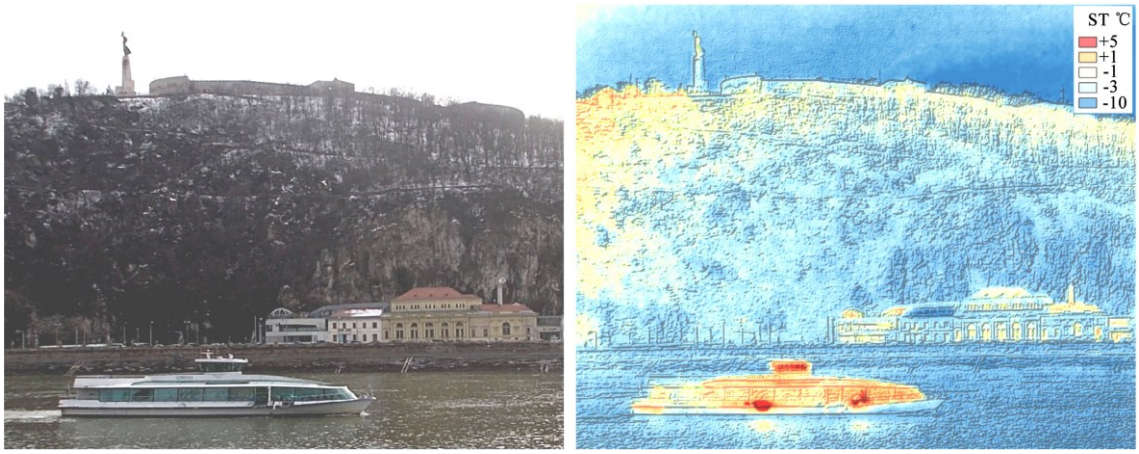

Fig. 6 The northern slopes of Gellért hill were, in some cases, 10 °C colder than the southern slopes on high-resolution thermal camera image (taken at 14:20 on 13. 01. 2019.).

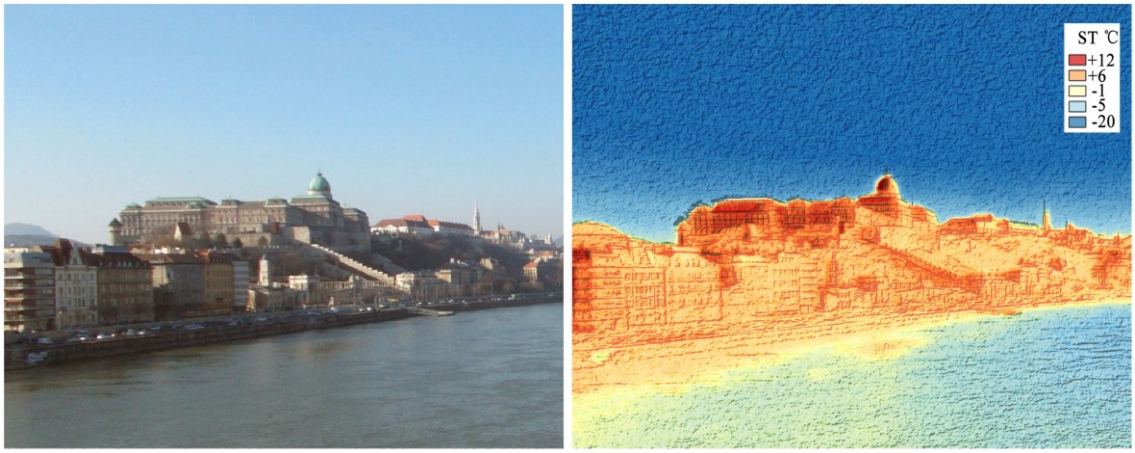

Fig. 7 Surface temperature (ST) of southeast slopes in Buda Castle hill. The castle walls facing south have significantly higher values than the walls facing east (taken at 14:09 on 07. 02. 2019.).

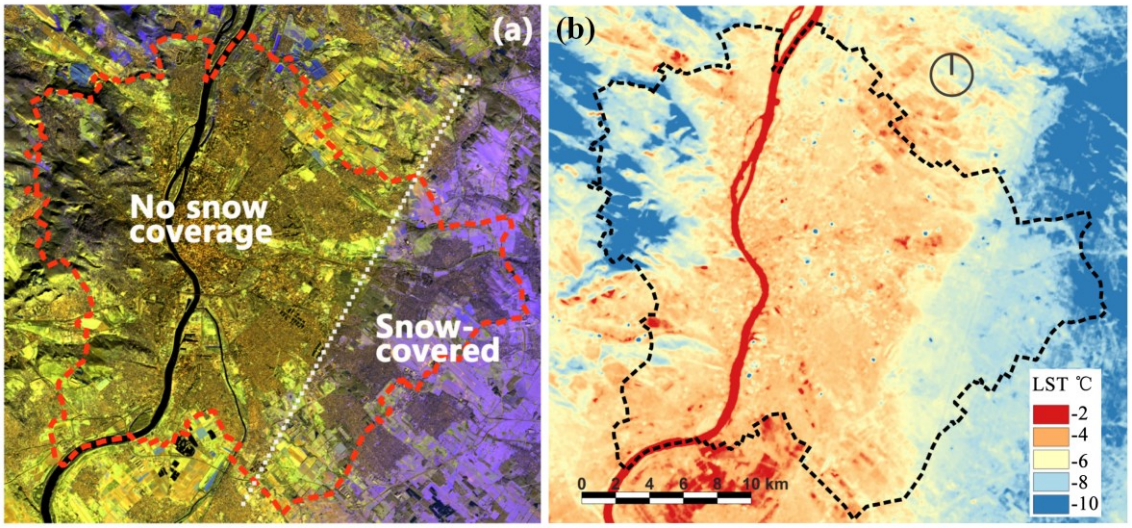

Fig. 8 The Land surface temperature (LST) of the snow-covered area and no snow coverage on 06. 01. 2017 (taken at 10:33). False color images based on the Landsat 8 image (a) and LST map (b).

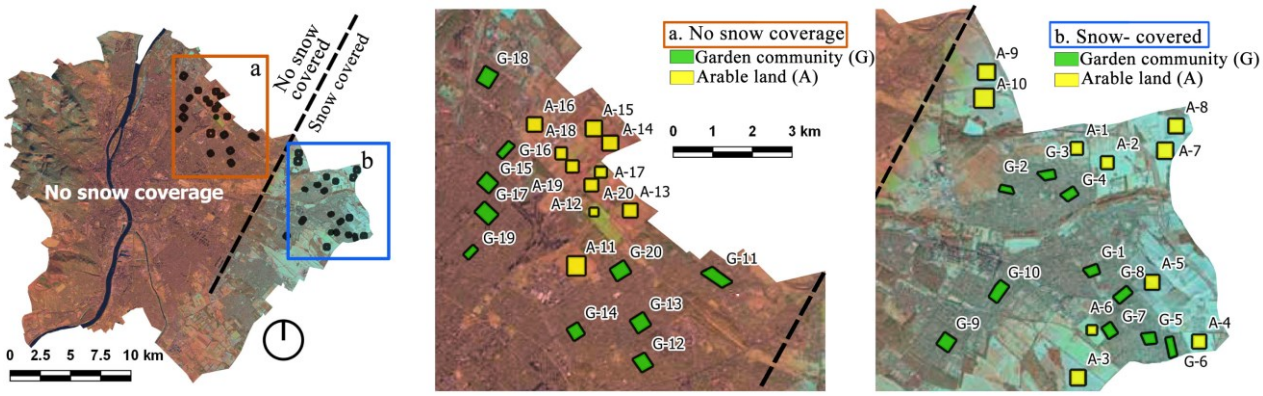

Fig. 9 Sample sites of garden community and arable land in the outer districts of Budapest. The selected 40 sites represent the most frequent land use types in the region.

The results for arable land showed that the snow-covered ten sites had lower temperatures than the areas of no snow cover (Fig. 10). The average temperature difference reached 4.36 ℃.

The results showed that snow cover could reduce LST by several degrees, but there was a slight difference in the intensity of the decrease in the two land-use types. Our study, based on 40 sample sites, showed that the arable land could be slightly colder than the garden community with snow coverage. Snow could cool down LST in arable land more significant than in the garden community. The snow had a less cooling effect in the

garden community than in arable lands, probably thanks to the human activity and variety of artificial elements in the built-up area. This fact reinforced the results that in Budapest, a moderate version of UHI exists in winter and affects snow cover.

The high-resolution thermal images of field surveys confirm the satellite LST results. From Fig.11, we can see that the surface temperature of the snow-covered area is significantly (5 °C) lower than the no snow-covered surface. The top of the pavilion is at the same angle as the top of the trash can, but the top of the trash bin was not covered by snow; due to different materials and larger surfaces, the pavilion preserves low temperature.

The exemplary thermal image shows similar effects along Szilas creek. The creek slopes were not covered by snow and were 5°C warmer than the snow-covered parts Figure 12 Compared to grassy slopes, the snow has higher reflectivity and lower heat capacity, resulting in less heat storage; therefore, indicating lower temperature.

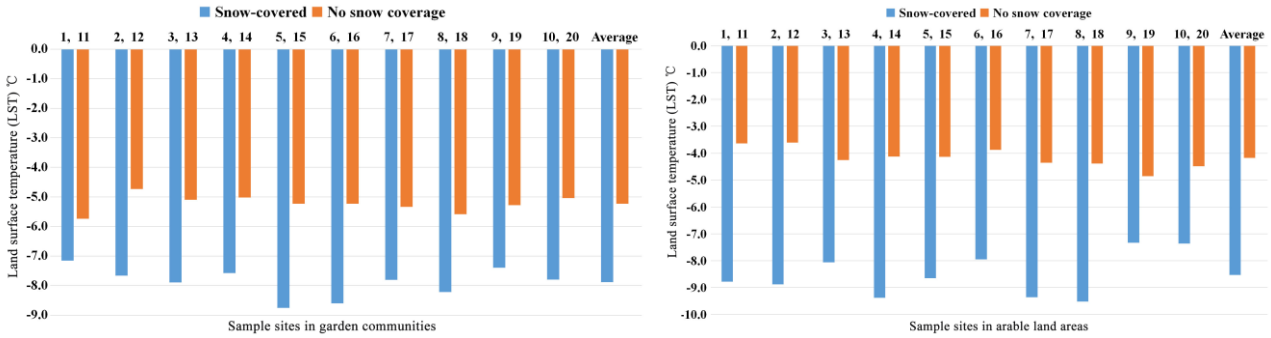

Fig. 10 Comparison between snow-covered and no snow-covered sites in residential areas with gardens (garden community) (left) and in arable land (right).

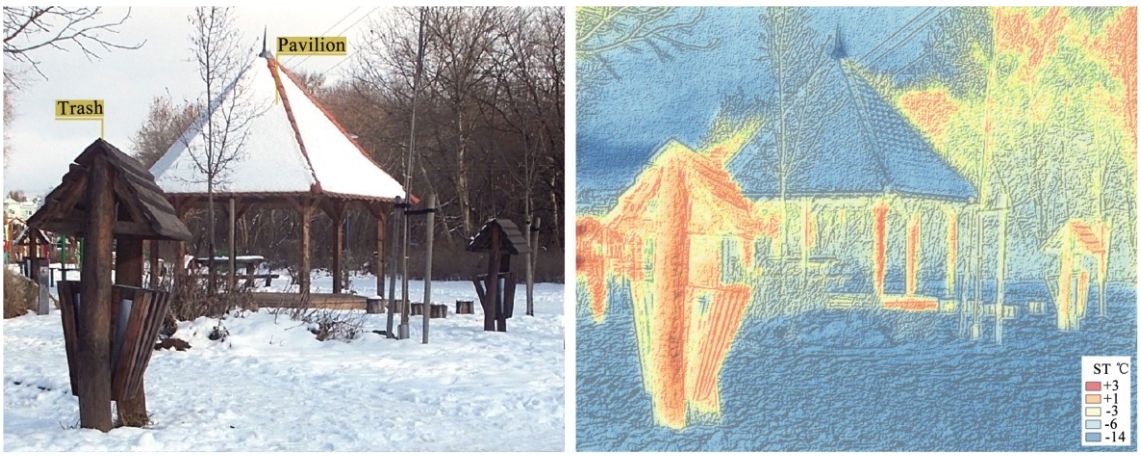

Fig. 11 Surface temperature (ST) differences indicated by snow cover in Hermina Sport and Leisure Park (XVI. District) (taken at 13:32 on 12.01. 2019).

Fig. 12 Surface temperature (ST) differences in a patchy snow-covered side Szilas creek (XVI. District) (taken at 13:59 on 12.01. 2019).

CONCLUSIONS

The study based on surface temperature analysis indicated that winter urban heat island exists in Budapest. Although the difference between the lowest and highest temperatures was not great, the study still revealed that the urban area was warmer than its surroundings. Warmer spots were mostly dispersed within built-up areas. The city's warmest elements were the airport, logistical buildings, huge store and parking areas, garages, and railway stations. Nevertheless, the parks, forests, and other woodland areas were colder than the average temperature. In addition, downtown densely built-up residential areas had a higher surface temperature than the suburban-style family house dominant garden communities. In general, it was revealed that the hilly Buda side (western) was colder than the low-lying and flat Pest side (eastern). The comparison of Budapest's 23 districts revealed that the inner districts (VII, IX) were the warmest, and the XII district was the coldest.

Topography was a significant factor influencing the surface temperature in winter. Our research showed that the surface temperature of the hills (300 m asl) was lower than that of the lowlands (below 120 m asl). The average temperature difference reached 2.68 °C. The slope also influenced the land surface temperature (LST). The results showed that south-facing slopes and south oriented buildings which absorbed solar heat for a long time were warmer than north-facing slopes and buildings oriented to the north. The results were especially spectacular in case Sas hill, Gellért hill, and buildings of Buda Castle. As a result of the low sun angle, a special kind of heat island, the "Vertical Heat Island," could be identified. The landscapes' vertical elements were illuminated and warmed up by the sun mostly from the side, so the heat island developed, especially on hill-slopes, walls, and facades of huge buildings.

Areas with snow coverage had low temperatures. Based on the result of the land surface temperature (LST) map of 06. 01. 2017 the comparison of snow-covered garden communities and arable lands proved, the areas without snow cover were lower by 2-4 °C than areas with snow cover. The same phenomenon appeared on high-resolution thermal images. Based on 40 sites, our study showed that snow has a less cooling effect in garden communities than on arable lands. This fact reinforced the results that in Budapest, a moderate version of urban heat island exists in winter and affects snow cover.

Based on the results, we give the following general guidance for further research and proposals for planning and design:

- Urban heat island characteristics of winter and summer should be compared in future research. Some elements show that the summer's advantage is winter's disadvantage. This can be influenced by coloring, choice of built or plant material, shading by built structures or trees.
- We recommend that planners in Budapest avoid the introduction of evergreen trees as shading elements near the southern side of buildings, as they provide a cooling effect in winter and block sunshine.
- We recommend to minimize winter heating costs; the new residential areas should consider the orientation of buildings with more attention to the south direction.

The paper collected characteristics of winter urban heat island in Budapest, mostly defined by natural and land-use dependant factors. The heat island is locally increased with individual human activities (traffic, transport, heating, production, etc.). These human activities influenced factors that need further research in the future.

ACKNOWLEDGEMENTS

This work was funded by the Department of Landscape Planning and Regional Development, Faculty of Landscape Architecture and Urbanism, Szent István University. The authors are grateful to the anonymous reviewers whose comments helped improve and clarify the article's content.

References

Andreou, E. 2014. The effect of urban layout, street geometry and orientation on shading conditions in urban canyons in the Mediterranean. *Renewable Energy* 63, 587–596. DOI: 10.1016/j.renene.2013.09.051

Beck, H.E., Zimmermann, N.E., McVicar, T.R., Vergopolan, N., Berg, A., Wood, E.F. 2018. Present and future Köppen-Geiger climate classification maps at 1-km resolution. *Scientific Data* 5, 180214. DOI: 10.1038/sdata.2018.214

Bhattacharya, B.K., Mallick, K., Padmanabhan, N., Patel, N.K., Parihar, J.S. 2009. Retrieval of land surface albedo and temperature using data from the Indian geostationary satellite: a case study for the winter months. *International Journal of Remote Sensing* 30, 3239–3257. DOI: 10.1080/01431160802559061

Cai, Z., Han, G., Chen, M. 2018. Do water bodies play an important role in the relationship between urban form and land surface temperature? *Sustainable Cities and Society* 39, 487–498. DOI: 10.1016/j.scs.2018.02.033

Chapman, S., Watson, J.E.M., Salazar, A., Thatcher, M., McAlpine, C.A. 2017. The impact of urbanization and climate change on urban temperatures: a systematic review. *Landscape Ecology* 32, 1921–1935. DOI: 10.1007/s10980-017-0561-4

Chen, X.-L., Zhao, H.-M., Li, P.-X., Yin, Z.-Y. 2006. Remote sensing image-based analysis of the relationship between urban heat island and land use/cover changes. *Remote Sensing of Environment* 104, 133–146. DOI: 10.1016/j.rse.2005.11.016

Deilami, K., Kamruzzaman, Md., Liu, Y. 2018. Urban heat island effect: A systematic review of spatio-temporal factors, data, methods, and mitigation measures. *International Journal of Applied Earth Observation and Geoinformation* 67, 30–42. DOI: 10.1016/j.jag.2017.12.009

Department of the Interior US Geological Survey 2019. Landsat 8 Data Users Handbook. Online available at: https://www.usgs.gov/land-resources/nli/ landsat/landsat-8-data-users-handbook

Dian, C., Pongrácz, R., Dezső, Z., Bartholy, J. 2020. Annual and monthly analysis of surface urban heat island intensity with respect to the local climate zones in Budapest. *Urban Climate* 31, 100573. DOI: 10.1016/j.uclim.2019.100573

Erell, E., Pearlmutter, D., Boneh, D., Kutiel, P.B. 2014. Effect of high-albedo materials on pedestrian heat stress in urban street canyons. *Urban Climate*, ICUC8: *The 8th International Conference on*

Urban Climate and the 10th Symposium on the Urban Environment 10, 367–386. DOI: 10.1016/j.uclim.2013.10.005

Gábor, P., Jombach, S. 2009. The relation between the biological activity and the land surface temperature in Budapest. *Applied Ecology and Environmental Research* 7, 241–251. DOI: 10.15666/aeer/0703_241251

Giridharan, R., Kolokotroni, M. 2009. Urban heat island characteristics in London during winter. *Solar Energy* 83, 1668–1682. DOI: 10.1016/j.solener.2009.06.007

Henits, L., Mucsi, L., Liska, C.M. 2017. Monitoring the changes in impervious surface ratio and urban heat island intensity between 1987 and 2011 in Szeged, Hungary. *Environment Monitoring and Assessment* 189, 86. DOI: 10.1007/s10661-017-5779-8

Hinkel, K.M., Nelson, F.E., Klene, A.E., Bell, J.H. 2003. The urban heat island in winter at Barrow, Alaska. *International Journal of Climatology* 23, 1889–1905. DOI: 10.1002/joc.971

Howard, L. 1818. The Climate of London: Deduced from Meteorological Observations, Made at Different Places in the Neighbourhood of the Metropolis. W. Phillips, Cambridge, MA, USA, 1820; Volume 1.

Kawashima, S. 1990. Effect of vegetation on surface temperature in urban and suburban areas in winter. *Energy and Buildings* 15, 465–469. DOI: 10.1016/0378-7788(90)90022-B

Kawashima, S., Ishida, T., Minomura, M., Miwa, T. 2000. Relations between Surface Temperature and Air Temperature on a Local Scale during Winter Nights. *Journal of Applied Meteorology* 39, 1570–1579.
DOI: 10.1175/1520-0450(2000)039<1570:RBSTAA>2.0.CO;2

Kolokotroni, M., Giridharan, R. 2008. Urban heat island intensity in London: An investigation of the impact of physical characteristics on changes in outdoor air temperature during summer. *Solar Energy* 82, 986–998. DOI: 10.1016/j.solener.2008.05.004

Kong, F., Yin, H., James, P., Hutyra, LR, He, H.S. 2014. Effects of spatial pattern of greenspace on urban cooling in a large metropolitan area of eastern China. *Landscape and Urban Planning* 128, 35–47. DOI: 10.1016/j.landurbplan.2014.04.018

Lam, C.K.C., Lau, K.K.-L. 2018. Effect of long-term acclimatization on summer thermal comfort in outdoor spaces: a comparative study between Melbourne and Hong Kong. *International Journal of Biometeorology* 62, 1311–1324. DOI: 10.1007/s00484-018-1535-1

László, E., Bottyán, Z., Szegedi, S. 2016. Long-term changes of meteorological conditions of urban heat island development in the region of Debrecen, Hungary. *Theoretical and Applied Climatology* 124, 365–373. DOI: 10.1007/s00704-015-1427-9

Li, H., Wang, G., Tian, G., Jombach, S. 2020. Mapping and Analyzing the Park Cooling Effect on Urban Heat Island in an Expanding City: A Case Study in Zhengzhou City, China. *Land* 9, 57. DOI: 10.3390/land9020057

Li, J., Song, C., Cao, L., Zhu, F., Meng, X., Wu, J. 2011. Impacts of landscape structure on surface urban heat islands: A case study of Shanghai, China. *Remote Sensing of Environment* 115, 3249–3263. DOI: 10.1016/j.rse.2011.07.008

Li, Y., Zhang, H., Kainz, W. 2012. Monitoring patterns of urban heat islands of the fast-growing Shanghai metropolis, China: Using time-series of Landsat TM/ETM+ data. *International Journal of Applied Earth Observation and Geoinformation* 19, 127–138. DOI: 10.1016/j.jag.2012.05.001

Liu, H., Weng, Q. 2008. Seasonal variations in the relationship between landscape pattern and land surface temperature in Indianapolis, USA. *Environitoring Monitoring and Assessment* 144, 199–219. DOI: 10.1007/s10661-007-9979-5

Lokoshchenko, M.A. 2014. Urban' heat island' in Moscow. *Urban Climate* 10, 550–562. DOI: 10.1016/j.uclim.2014.01.008

Mathew, A., Khandelwal, S., Kaul, N. 2017. Investigating spatial and seasonal variations of urban heat island effect over Jaipur city and its relationship with vegetation, urbanization and elevation parameters. *Sustainable Cities and Society* 35, 157–177. DOI: 10.1016/j.scs.2017.07.013

Middel, A., Brazel, A.J., Gober, P., Myint, S.W., Chang, H., Duh, J.-D. 2012. Land cover, climate, and the summer surface energy balance in Phoenix, AZ, and Portland, OR. *International Journal of Climatology* 32, 2020–2032. DOI: 10.1002/joc.2408

Oke, T.R. 1973. City size and the urban heat island. *Atmospheric Environment* 1967 7, 769–779. DOI: 10.1016/0004-6981(73)90140-6

Oke, T.R. 1982. The energetic basis of the urban heat island. *Quarterly Journal of the Royal Meteorological Society* 108, 1–24. DOI: 10.1002/qj.49710845502

Oke, T.R. 1987. Boundary Layer Climates. Routledge, London, 464 pp.

Oláh A. B. 2012. The effect of the urban built-up density and the land cover types on the radiated temperature (Phd Dissertation). Corvinus University of Budapest, Budapest. 146 pp.

Oliveira, S., Andrade, H., Vaz, T. 2011. The cooling effect of green spaces as a contribution to the mitigation of urban heat: A case study in Lisbon. *Building and Environment* 46, 2186–2194. DOI:10.1016/j.buildenv.2011.04.034

OMSZ 2020. Annual data Budapest - met.hu. Meteorol. Inf. Serv. Online available at: http://www.met.hu/en/eghajlat/magyarorszag_eghajlata/eghajlati_adatsorok/Budapest/adatok/eves_adatok/

Probáld, F. 2014. The urban climate of Budapest: past, present and future. *Hungarian Geografical Bulletin* 63, 69–79. DOI: 10.15201/hungeobull.63.1.6

Sachanowicz, K., Ciechanowski, M., Tryjanowski, P., Kosicki, J.Z. 2018. Wintering range of Pipistrellus nathusii (Chiroptera) in Central Europe: has the species extended to the north-east using urban heat islands? *Mammalia* 83. 260-271. DOI: 10.1515/mammalia-2018-0014

Unger, J., Makra, L. 2007. Urban-rural difference in the heating demand as a consequence of the heat island. *Acta Climatologica et Chorologica* 40-41, 155–162.

EPA, 2014. Heat Island Effect. US EPA. Online available at: https://www.epa.gov/heat-islands.

Westermann, S., Langer, M., Boike, J. 2012. Systematic bias of average wintertime land surface temperatures inferred from MODIS at a site on Svalbard, Norway. *Remote Sensing of Environment* 118, 162–167. DOI: 10.1016/j.rse.2011.10.025

Woodcock, C.E., Strahler, A.H. 1987. The factor of scale in remote sensing. *Remote Sensing of Environment* 21, 311–332. DOI: 10.1016/0034-4257(87)90015-0

Yin, X., Zhang, Q. 2014. Analysis between AMSR-E swath brightness temperature and snow cover area in winter time over Sierra Nevada, Western US *Proceedings of the SPIE, Asia-Pacific Remote Sensing, Beijing, China,* Volume 9260, id. 92604K 5 pp. (2014). DOI: 10.1117/12.2074214

Zhang, Yazhou, Zhan, Y., Yu, T., Ren, X. 2017a. Urban green effects on land surface temperature caused by surface characteristics: A case study of summer Beijing metropolitan region. *Infrared Physics & Technology.* 86, 35–43. DOI: 10.1016/j.infrared.2017.08.008

Zhang, Yujia, Murray, A.T., Turner, B.L. 2017b. Optimizing green space locations to reduce daytime and nighttime urban heat island effects in Phoenix, Arizona. *Landscape and Urban Plan.* 165, 162–171. DOI: 10.1016/j.landurbplan.2017.04.009

Zhang, Z., He, G. 2007. Comparison between summer and winter urban heat island of Beijing city, Proc. SPIE 6790, MIPPR 2007: *Remote Sensing and GIS Data Processing and Applications; and Innovative Multispectral Technology and Applications*, 67900T (14 November 2007); DOI: 10.1117/12.747322

sciendo

Journal of Environmental Geography 13 (3–4), 44–50.

DOI: 10.2478/jengeo-2020-0011
ISSN 2060-467X

TREND ANALYSIS OF TEMPERATURE AND HUMIDITY IN KWARA STATE, NIGERIA

Adeniyi Adedapo[1]*

Department of Geography, Kwara State Polytechnic
P.M.B 1375, Ilorin, Kwara State, Nigeria
*Corresponding author, e-mail: dapomoses@gmail.com

Research article, received 30 May 2020, accepted 19 November 2020

Abstract

This paper examines the trend analysis of temperature and relative humidity in Kwara State. Climatic data on annual mean temperature (minimum and maximum) and relative humidity for 40 years (1978- 2017) were collected from Nigerian Meteorological Agency (NIMET) Ilorin. Semi-Average method, Mann- Kendull statistics and regression method were used to analyse the trend in temperature and relative humidity. The Standardized Anomaly Index (SAI) was also used to examine the changes in temperature and humidity over the period of 1978 -2017. The result of the analysis indicates that temperature (minimum and maximum) and relative humidity exhibit an upward trend. This implies that temperature and relative humidity increase over the period of 1978 -2017. The Mann-Kendull statistics values show that there is no significant difference in the values of temperature (minimum and maximum) and relative humidity. The result of the Standardized Anomaly Index (SAI) also revealed that the values of temperature and humidity fluctuated around the long –term mean. About 50% of the annual average relative humidity falls above the long term average while 40% of the annual mean maximum temperature falls above the long term average. It can therefore, be deduced that there is the possibility of increment in the values of temperature and relative humidity which could cause a serious challenge to human health and climate change. The study therefore, suggests that increase and fluctuations in temperature and relative humidity should be a critical factor in designing strategies to mitigate the effect of climate change on the environment and human health.

Keywords: Trend Analysis, Minimum and Maximum Temperature, Relative Humidity, Fluctuations

INTRODUCTION

A trend is a pattern of gradual change in a data gathered sequentially at equal spaced time interval. It is an increase or decrease in the value of a variable occurring over a period of several years. Trend is a long-term change (increase or decrease) in a time series (Ragatoa, 2018). Trend analysis is a technique for extracting an underline pattern of a behavior in a data collected over time, and the science of studying changes in pattern in a time series. Trend analysis is generally used to estimate uncertain events in the past and to predict future outcome of an events. Trends have become the most frequently used technique to identify climatic variability in regional and local basis (Amadi et. al., 2014).

Many studies in climate literature have employed trend analysis to examined pattern of changes in climatic parameters, especially variations in temperature. Some examined changes in global and regional mean temperature (Olofintoye and Sule, 2010; Jain and Kumar, 2012; Jones et al., 2013) while some studied trends in temperature on different spatial and temporal scales (Ogolo and Adeyemi, 2009). According to Karaburun et al. (2011) majority of these studies have found an increasing trend in temperature, although the variations differ slightly from one region to another. Xu et al. (2017) reported that temperature has increased more than 0.3 °C/decade in most areas in north China and 0.1–0.3 °C/decade in most of south China. Similarly, Ahmad (2015) also reported that variations of temperature over most part of Iran from 1961–2010 show a positive trend with the rate of change varying from 0.09°C to 0.38°C per decade. Historical evidences have shown that, since 1880, global mean temperature has increased about 0.85 ± 0.2 ºC (IPCC, 2014). Similarly, the general trend of minimum and maximum temperature in Nigeria was found to be increasing (Ragatao et. al., 2018).

Temperature and humidity are essential elements in the study of weather and climate forecasting. They are basic environmental factors influencing thermal comfort which is a fundamental concept for climate control systems. Variations and fluctuations in climatic elements, especially temperature and humidity, and its consequential effect on the environment and human health has become a global concern. Understanding climatic patterns is of great importance when several global challenges such as food insecurity, water crisis, biodiversity loss, and health issues are tied to climate change (IPCC, 2014). Changes in surface air temperature are a fundamental indicator of climate change. Hansen et al. (2012) examined the trend of global temperature change and reported that the increasing temperature may influence sea level and the extermination of species. Similarly, Vicente-Serrano et al. (2014) and Xie et al.

(2011) reported that understanding patterns and trends in relative humidity will reduce uncertainties in the estimation of future climatic changes. Therefore, assessment of the characteristics of climatic elements is vital for understanding of both the temporal and spatial variability at local, regional or global scales and their effect on the environment and human health.

Trend analysis of ambient air temperature and humidity are essential in assessing environmental heat stress on human health (Ogbonmwan et al., 2016). Field et al. (2012) opined that extremely high air temperatures have a profound effect on human and natural systems while Wehner et al. (2017) reported that human health and welfare are mainly affected by the combination of high heat and relative humidity. Wehner et al. (2017) also noted that the highly cited literature on the impacts of climate change (Smith et al., 2014) considers both variations in temperature and humidity on future occupational heat stress. Hot and moist air makes people feel uncomfortable, while extremely dry air cause discomfort on human body. High humidity leads to continuous sweating and also cause overheating or heat exhaustion which can lead to dehydration, chemical imbalances in the body and ultimately death. Patz et al. (2005) opined that the reproduction and survival rates of bacteria and viruses, which are devoid of thermostatic mechanisms, are greatly affected by temperature variability. According to Ye et al. (2013) understanding changes in the surface air temperature and humidity are vital because they can have severe impacts on the hydrological cycle and the surface energy budget. Furthermore, Lewis and King (2016) also reported that knowledge about the specific characteristics of changes in temperature distributions in response to background warming is an essential aspect of fully understanding changes in heat extremes and their related impacts on human and ecosystem health.

From the ongoing discussion, it is clear that knowledge about changes in temperature and humidity are critical to human comfort, climate change and other contemporary environmental problems. Understanding the uncertainties associated with temperature and humidity patterns will provide a knowledge base for better management of heat stress, climate change and other related environmental hazards. According to Meshram et al. (2018) trend analysis of temperature on different spatial scales will help in the construction of future climate scenarios. Therefore, the objectives of the study is to examine the pattern of temperature and humidity in Kwara State with the aim of creating awareness on the changes in temperature (minimum and maximum) and humidity which are useful information in developing strategies to mitigate the impact of heat stress on human comfort, its impact on climate change and other related environmental problems.

STUDY AREA

Kwara State is located on longitude 2°6'E and 5°2'E and latitude 7°30'N and 9°40'N. It is situated within the North Central geopolitical zone of Nigeria. Kwara State shares boundary with Republic of Benin and with five states in Nigeria. These states are Niger in the North, Oyo, Osun and Ekiti in the South, and Kogi in the East. Kwara State comprises of sixteen local government areas. In term of population, according to 2006 population census, the population of Kwara state was 2,365,353 (NPC, 2006). Figure 1 shows the map of Kwara State showing the topography and the location of weather station.

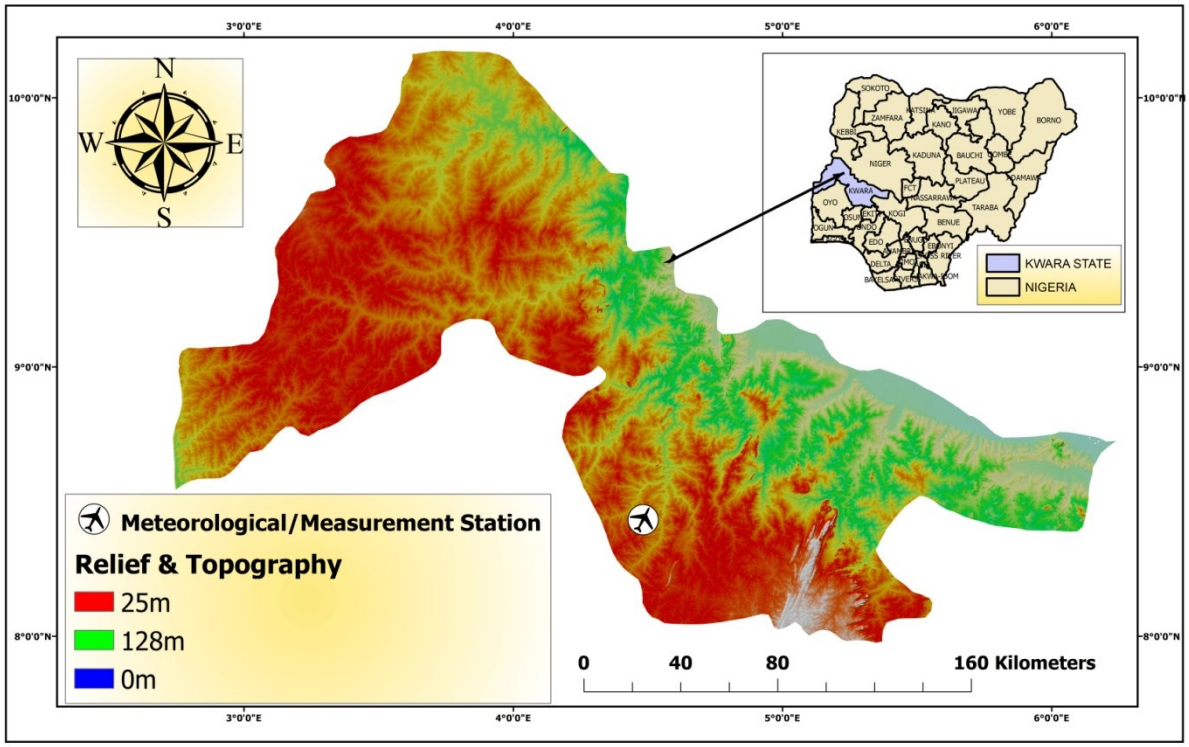

Fig.1 Map of Kwara State showing the Topography and Location of Weather Station

The climate of Kwara State exhibits both wet (rainy) and dry seasons in response to the South West Monsoon wind and the North East continental wind which are the major prevailing winds that blow across the state. The wet or rainy season begins towards the end of April and last till October. The dry season begins in November and end in April. The temperature of the state ranges from 33°C to 35°C from November to January and from 34°C to 37°C from February to April. The total annual rainfall ranges from 990.3mm to 1318mm. The rainfall exhibits double maximal pattern. Relative humidity ranges from 75% to 88% from May to October and 35% to 80% during the dry season (Ajadi and Adeniyi, 2017).

MATERIALS AND METHODS

Power series polynomial model and trigonometric polynomial or fourier series model are the basic models of trend surface analysis. However, the power series model is used in this study because it is the most frequently used model of trend surface analysis. Monthly data on temperature (minimum and maximum) and relative humidity were collected from 1978–2017 from Nigerian Meteorological Agency, (NIMET) Ilorin. The liquid-in-glass thermometer was used to collect data on minimum and maximum temperature while hygrometer was used to collect data on humidity. These instruments are the most common instruments used for measuring temperature and humidity with high accuracy. These data were collected from the weather station in the Ilorin International Airport. The 5 year Moving average was used to calculate short term fluctuations. Semi-Average method was used to analyse the trend in temperature (minimum and maximum) and relative humidity. The method was employed because it is more objective than fitting a line by eye to the plotted series. Regression method was also used to analyse trend in temperature and humidity. The study period was 40 years 1978–2007 and it was divided into four equal parts to examine the deviation of decadal means from the long term mean. The study period was also sub-divided into two sub periods, 1978–2017 and 1978–2007 based on climatic normal that is 30 years (1978–2007). The essence of the sub-division is to investigate the trend in the climatic elements in relation to the percentage change from 1978–2017. Mann-Kendall test was used for the analysis of trend (increasing or decreasing) in temperature and humidity. Mann Kendal test was employed because it is a non parametric test which does not require the data to be normally distributed and also has low sensitivity to short breaks due to inhomogeneous time series (Tabari et al. 2011). In addition, it is the most generally used methods and appropriate method of detecting trends. The Mann Kendall trend test have been extensively used and adapted several times especially in diverse studies on trend analysis (Ragata et al. 2018). The method was employed by Adeniyi (2016) in the study of spatio- temporal variations of wind flow and its implications for energy generation in the Sudano-Sahelian Zone, Nigeria and also by Birhanu et al. (2017) in the study of temperature and precipitation trend over 30 years in Southern Tigray, regional State, Ethiopia.

The Standardized Anomaly Index (SAI) was also used to examine the changes in the values of temperature and humidity over the period of 1978-2017. The Standardized Anomaly Index was calculated using the following equation:

$$SAI = \frac{X_i - \overline{X}}{S.D}$$

Where:

X_i = annual total of the parameter

$\overline{X}$ = mean value of the parameter for the period of study

S.D = standard deviation from the mean value of the parameter for the period of study.

RESULTS AND DISCUSSION

Fluctuations in Annual Temperature and Relative Humidity (1978 – 2017)

The graphs in Figures 2–4 revealed the fluctuations of minimum temperature, maximum temperature and relative humidity in Kwara state (1978–2017). The annual minimum temperature (Fig. 2) in the state falls below the long term average in the years from 1978 to 1979, 1981 to 1982, 1984 to 1986, 1990, 1992 to 1998, 2000 to 2001, 2011 and 2015 to 2017. About 43% of the annual minimum temperature falls above the long term average. The longest consecutive years when annual minimum temperature falls below the long term mean were recorded from 1992 to 1998 while the longest consecutive years when minimum temperature falls above the long term mean were recorded from 2003 to 2005 and 2012 to 2014. The annual maximum temperature (Fig. 3) in the state falls above the long term average in the years from 1987, 1996, 1998, 2000 to 2003, 2006 to 2011 and 2015 to 2017. Fifty percent (50%) of the annual mean maximum temperature falls below the long term average while 40% of the annual mean maximum temperature falls above the long term average. The longest consecutive years when annual mean maximum temperature falls below the long term mean was recorded from 1979 to 1984 while the longest consecutive years when minimum temperature falls above the long term mean was recorded from 2006 to 2011. Figure 4 revealed that the annual relative humidity in the state falls below the long term average in the years from 1982 to 1985, 1987 to 1990, 1992 to 1998, 2000 to 2002 and 2008. About 50% of the annual mean relative humidity falls above the long term average. The longest consecutive years when annual relative humidity falls below the long term mean was recorded from 1992 to 1998 while the longest consecutive years when minimum temperature falls above the long term mean was recorded from 2009 to 2005 and 2017. The above findings show that temperature (minimum and maximum) and relative humidity varies from year to year and fluctuated around the long term mean.

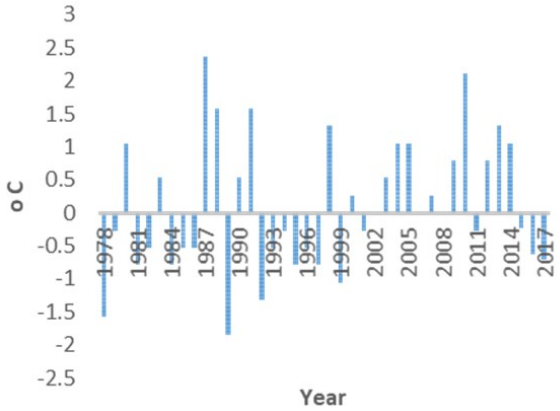

Fig.2 Annual Minimum Temperature Fluctuations for Kwara State

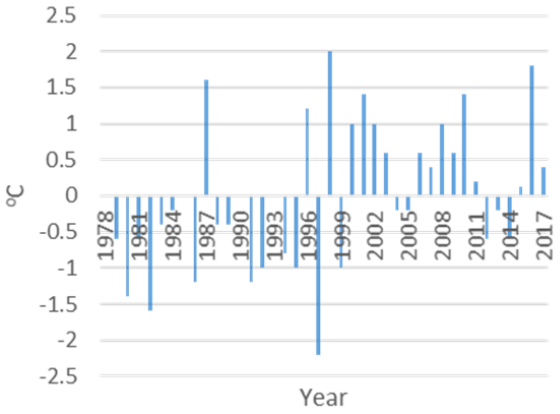

Fig.3 Annual Maximum Temperature Fluctuations for Kwara State

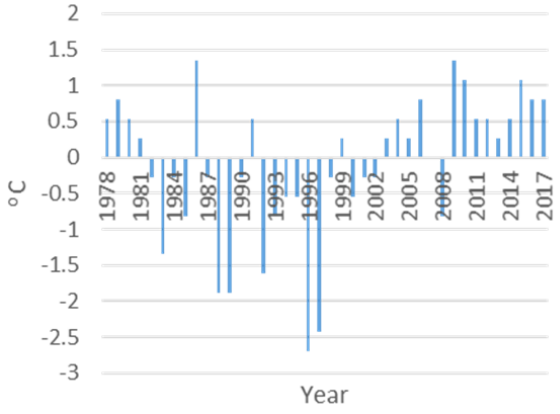

Fig.4 Annual Relative HumidityFluctuations for Kwara State

Deviation of Decadal Means of Climatic Parameters in Kwara State (1978–2017)

Table 1 shows the deviation of the decadal mean values of minimum temperature, maximum temperature and relative humidity from the long term 1978–2017. The highest deviation of decadal mean of minimum temperature was in 2008 to 2017 (+0.2) while that of maximum temperature was in 1998 to 2007. The lowest deviation of decadal mean of relative humidity (+0.6)

Table 1 Deviation of Decadal Means of Climatic Parameters in Kwara State (1978-2017)

Period	Deviation of Decadal Mean		
	Minimum Temperature	Maximum Temperature	Relative Humidity
1978 – 1987	0.00	-0.2	+0.6
1988 – 1997	-0.1	-0.3	-4.1
1998 – 2007	+0.1	+0.3	+0.7
2008 – 2017	+0.2	+0.2	+2.7

Table 2 Deviation of the 1978 – 2017 Means of Climatic Parameters from 1978-2007 in Kwara State

Climatic Elements	1978 - 2017	1978 - 2007	Change	Change [%]
Minimum Temperature [^{0}C]	21.7	21.6	-0.1	-0.46
Maximum Temperature [^{0}C]	32.5	32.4	-0.1	-0.31
Relative Humidity [%]	74.0	73.0	-1.0	-1.35

was in 1978 to 1987. Temperature (minimum and maximum) and relative humidity exhibit positive deviation of decadal mean in 1998–2007 and 2008–2017. This implies that there is an increase in the values of temperature and relative humidity from 1998–2017. The negative signs show a decrease in the values of the climatic parameters.

Deviation of the 1978–2017 Means of Climatic parameters from 1978–2007

The period under study, 1978 to 2017 was divided into two sub- periods, 1978–2017 and 1978–2007 to show the deviation of the means of temperature (minimum and maximum) and humidity of 1978–2017 from 1978–2007. Table 2 shows a decrease in percentage change of minimum temperature, maximum temperature and relative humidity. There was a decrease of –0.46% of minimum temperature and -0.31% decrease of maximum temperature. Relative humidity has -1.35% decrease in percentage change. The negative change in the percentage of change implies that there were declines in the values of minimum temperature, maximum temperature and relative humidity in the state from 1978 -2007, though the rates of deviation were small.

Variation of Temperature and Relative Humidity (1978–2017)

Figures 5–7 show the variation of the mean and the 5-year Moving average of minimum temperature, maximum temperature and relative humidity in Kwara state from 1978 to 2017. The annual values of minimum temperature fluctuated from 21.0°C in 1989 to 22.6°C in 1987 (Fig. 5). Figure 6 shows that maximum

temperature fluctuated from 31.4°C in 1997 to 33.5°C in 1998 while that of relative humidity fluctuated from 71% in 1985 to 79% in 2009 (Fig. 7). This implies that there were little variations in the values of temperature (minimum and maximum) and relative humidity. Similarly, the smoothed by running averages for the period of 5 years also revealed that there is little variation in the values of temperature and relative humidity.

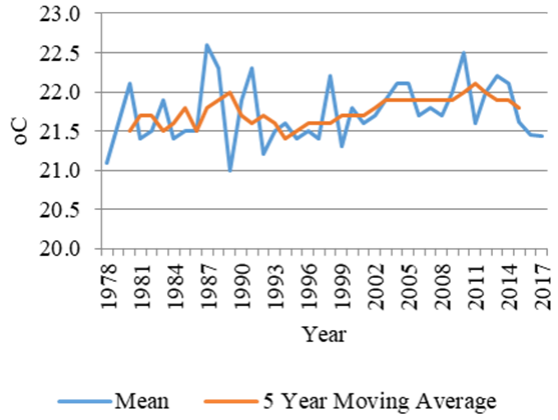

Fig. 5 Trend of 5-Year Moving average of Annual Minimum Temperature in Kwara State

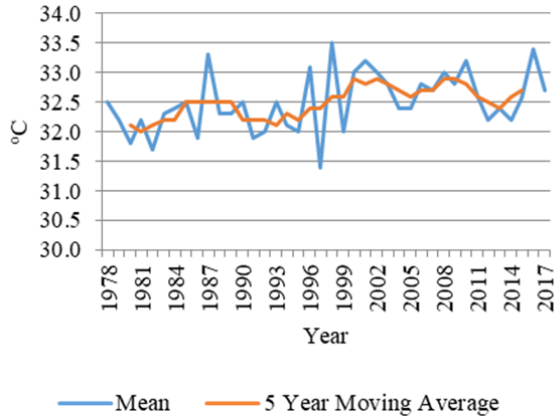

Fig. 6 Trend of 5-Year Moving average of Annual Maximum Temperature in Kwara State

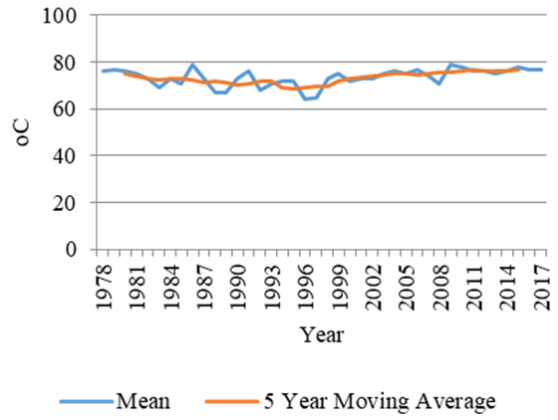

Fig. 7 Trend of 5-Year Moving average of Annual Relative Humidity in Kwara State

Trend in Temperature and Relative Humidity Using Semi Average Method

The annual value of minimum temperature, maximum temperature and relative humidity for the period of 40 years, (1978 to 2017) were analyzed for trends using semi average method (Table 3). From the table, minimum temperature, maximum temperature and relative humidity exhibit an upward trend, although the changes are very small. This implies that values of temperature (minimum and maximum) and relative humidity in the state will keep on increasing. In addition, it also indicates a warming trend. This finding of increase in temperature agreed with the report of the International Panel on Climate Change (IPCC) (2013) which state clearly that temperature trends on a global scale show a warming of 0.85 (0.65-1.06)°C, over the period 1880–2012.

Trend in Temperature and Relative Humidity Using Mann-Kendull Statistics (1978-2017)

The result of the trend analysis using Mann-Kendull statistics shows increasing (positive) trends in the values of temperature and humidity. The result of the statistics in Table 4 also shows that there is no significant difference in the values of temperature (minimum and maximum) and relative humidity at either 95% or 99% probability levels. This is because the values of the Mann-Kendull statistics (r) is less that the theoretical value $(r)_t$. This implies that no differential pattern of variation exist in the values of temperature and relative humidity in the state.

Table 3 Trend in Temperature (Minimum and Maximum) and Relative Humidity Using Semi Average Method

Climatic Elements	First Part Avg.	Second Part Avg.	Trend
Minimum Temperature [°C]	21.6	21.8	Upward Trend
Maximum Temperature [°C]	32.2	32.7	Upward Trend
Relative Humidity [%]	71.9	75.3	Upward Trend

Table 4 Trend in Temperature (Minimum and Maximum) and Relative Humidity Using Mann-Kendull Statistics

Climatic Elements	R
Minimum Temperature	0.06
Maximum Temperature	0.23
Relative Humidity	0.17

Trend Analysis of Temperature and Humidity Using Linear Regression Method

Figures 8–10 show the actual, trend lines and trend equations of temperature (minimum and Maximum) and humidity in Kwara state (1978–2017). From the figures (Figures 8–10), the trend lines show an upward trend. This implies that there is an increase in the values of temperature (minimum and maximum) and relative humidity. In addition, no definite break in the trend of temperature and humidity is observed, although the values fluctuate. The rate of increase in trend is very small. However, an increase in temperature leads to climate change which can negatively affect weather and consequently cause many climatological hazards like drought.

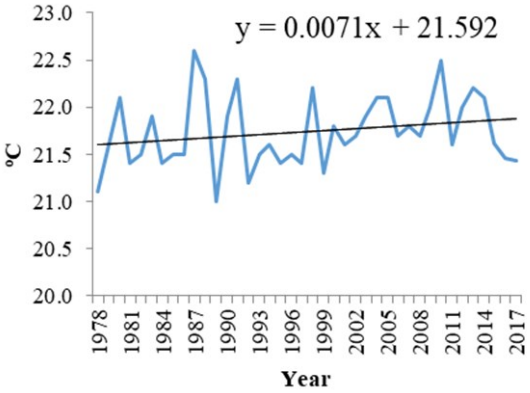

Fig. 8 Trend of Annual Minimum Temperature in Kwara State

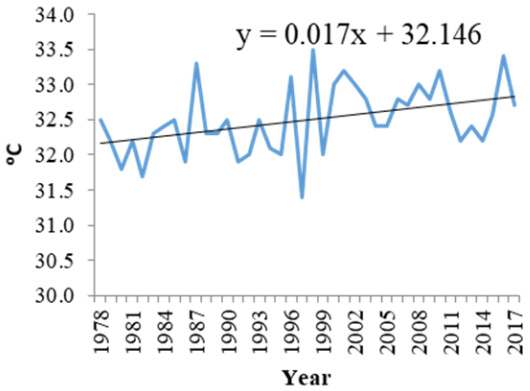

Fig. 9 Trend of Annual Maximum Temperature in Kwara State

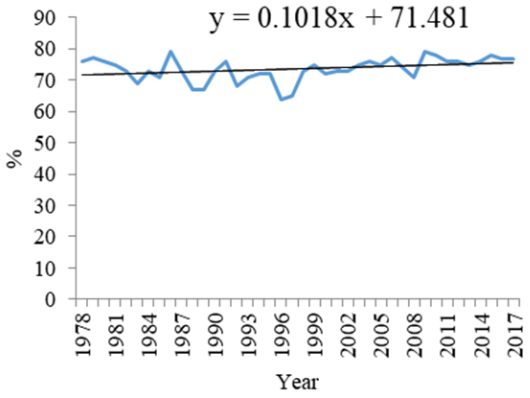

Fig. 10 Trend of Annual Relative Humidity in Kwara State

CONCLUSIONS AND RECOMMENDATIONS

The trend analysis of temperature and relative humidity for 40 years (1978–2017) in Kwara State revealed that annual mean values of minimum temperature, maximum temperature and relative humidity fluctuated around the long- term mean. Fifty percent (50%) of the annual mean maximum temperature falls below the long term average while 40% of the annual mean maximum temperature falls above the long term average. About 50% of the annual mean relative humidity falls above the long term average. This means that the identified climatic parameters in the years under review have show both below and above long term mean pattern. The deviation of decadal means of temperature and relative humidity from the long term mean shows positives in 1998–2007 and 2008–2017. The result of trend analysis shows that temperature and relative humidity exhibits an increasing trend. The increase in temperature indicates a warming trend. This implies that the state is vulnerable to the effect of global warming which is dangerous to the environment and human health. The result also suggests that the increase in temperature can lead to an increase in heat index which can lead to heat disorders such as pain, blisters, fever, headaches, heavy sweating and heat stroke or sunstroke. In addition, increase in temperature can lead to climatological hazards like drought and climate change. The increase in temperature and relative humidity could be as a result of impact of urbanization and other anthropogenic activities in the state. Therefore, the study recommends that potential increase in temperature and relative humidity should be a critical factor in designing strategies to cope with and reduce the effect of climate change on the environment and human health.

References

Adeniyi, A. 2016. Spatio-Temporal Variations of Wind Flow and Its Implications for Energy Generation in The Sudano-Sahelian Zone, Nigeria. Ph.D. Thesis Submitted to the Department of Geography and Environmental Management, University of Ilorin, Ilorin.

Ahmad, R.G. 2015. Changes and Trends in Maximum, Minimum and Mean Temperature Series in Iran. *Atmospheric Science Letters* 16 (3), 366–372. DOI: 10.1002/asl2.569

Ajadi, B. S., Adeniyi, A. 2017. Trends Analysis of Agricultural Productivity in Kwara State, Nigeria. *Journal of Research and Development Studies*. 5 (1), 205–214. Online available at: https://kwarastatepolytechnic.edu.ng/pub/trends%20analysis.pdf

Amadi, S.O., Udo, S.O., Ewona, I.O. 2014. Trends and Variations of Monthly Mean Minimum and Maximum Temperature Data Over Nigeria for the Period 1950-2012. *International Journal of Pure and Applied Physics* 2 (4), 1–27. Online available at: http://www.eajournals.org/wp-content/uploads/Trends-And-Variations-Of-Monthly-Mean-Minimum-And-Maximum-Temperature-Data-Over-Nigeria-For-The-Period-1950-2012..pdf

Birhanu, H., Yingjun, C., Zinabu, M., Miseker, B. 2017. Temperature and Precipitation Trend Analysis over the last 30 years in Southern Tigray regional State, Ethiopia. *Journal of Atmospheric Pollution* 5 (1), 18–23. DOI: 10.20944/preprints201702.0014.v1

Field, C.B., Barros, V., Stocker, T.F., Qin, D., Dokken, D.J., Ebi, K.L., Mastrandrea, M.D., Mach, K.J., Plattner, G.K., Allen, S.K., Tignor, M., Midgley, P.M. (Eds.) 2012. Managing the Risks of Extreme Events and Disasters to Advance Climate Change Adaptation. A Special Report of Working Groups I and II of the

Intergovernmental Panel on Climate Change. Cambridge University Press, Cambridge

Hansen, J., Sato, M., Ruedy, R. 2012. Perception of Climate Change. *Proceedings of the National Academy of Sciences* 109 (37), E2415-E2423. DOI: 10.1073/pnas.1205276109

IPCC, 2014. Climate Change 2014: Synthesis Report. Contribution of Working Groups I, II and III to the Fifth Assessment Report of the Intergovernmental Panel on Climate Change [Pachauri, R.K., Meyer, L.A. (Eds.)]. IPCC, Geneva, Switzerland, 151. Online available at: https://epic.awi.de/id/eprint/37530/1/IPCC_AR5_SYR_Final.pdf

IPCC, 2014. Summary for Policymakers In. Climate Change 2013 – The Physical Science Basis. Contribution of Working Group I to the fifth Assessment Report of the International Panel on Climate Change, Cambridge University Press, Cambridge, 1–30. DOI: 10.1017/CBO9781107415324.004

Jain, S.K., Kumar, V. 2012. Trend analysis of rainfall and temperature data for India. *Current Science* 102 (1), 37 – 49. Online available at: https://www.jstor.org/stable/24080385

Jones, P.D., Parker, D.E., Osborn, T.J., Briffa, K.R. 2016. Global and hemispheric temperature anomalies – land and marine instrumental records. In *Trends: A compendium of Data on Global Change*, Doi: 10.3334/CDIA/cli.002. Online available at: https://cdiac.ess-dive.lbl.gov/trends/temp/jonescru/jones.html

Karaburun, A., Demirci, A., Kora, F. 2011. Analysis of spatially distributed annual, seasonal and monthly temperatures in Istanbul from 1975 to 2006. *World Applied Sciences Journal* 12 (10), 1662–1675. Online available at: http://www.idosi.org/wasj/wasj12(10)/2.pdf

Lewis, S.C., King, A.D. 2016. Evolution of mean, variance and extremes in 21st century temperatures. *Weather and Climate Extremes* 15, 1–10. DOI: 10.1016/j.wace.2016.11.002

Meshram, S.G., Singh, S.K., Meshram C., Deo R.C., Ambade, B. 2018. Statistical evaluation of rainfall times series in concurrence with agricultutre and water resources of Ken River basin, Central India (1901-2010). *Theoretical and Applied Climatology* 134, 1231–1243. DOI: 10.1007/s00704-017-2335-y

Ogbonmwan, S.M., Ogbomida, E.T., Uwadia, N.O., Efegoma, O.R. And Umoru, G.L. 2016. Analysis of Trends in the Variability of Monthly Mean Minimum and Maximum Temperature and Relative Humidity in Benin City. *International Journal on Renewed Energy & Environment* 2, 150–165.

Ogolo, E.O., Adeyemi, B. 2009. Variations and Trends of some Meteorological Parameters at Ibadan, Nigeria. *The Pacific Journal of Science and Technology* 10 (2), 981–987. Online available at: http://www.akamaiuniversity.us /PJST10_2_980.pdf

Olofintoye, O.O., Sule, B.F. 2010. Impact of global warming on the rainfall and temperature in the Niger Delta of Nigeria. *USEP Journal of Research Information and Civil Engineering*, 7 (2), 33–48.

Patz, J.A., Campbell-Lendrum, D., Holloway, T., Foley, J.A. 2005. Impact of Regional Climate Change On Human Health. *Nature* 438, 310–317. DOI: 10.1038/nature04188

Ragatoa, D.S., Ogunjobi, K.O., Okhimamhe, A.A., Francis, S.D., Adet, L. 2018. A Trend Analysis of Temperature in Selected Stations in Nigeria Using Three Different Approaches. *Open Access Library Journal* 5, 1–17. DOI: 10.4236/oalib.1104371

Tabari, H., Marofi, S., Aeini, A., Talaee, P.H., Mohammadi, K. 2011. Trend Analysis of Reference Evapotranspiration in the Western half of Iran. *Agricultural and Forest Meteorology.* 151 (2), 128–136. DOI: 10.1016/j.agrformet.2010.09.009

Vicente-Serrano, S.M., Azorin-Molina, C., Sanchez-Lorenzo, A., Moran-Tejeda, E., Lorenzo-Lacruz, J., Revuelto, J., Lopez-Moreno, J., Espejo, F. 2014. Temporal evolution of surface humidity in Spain: Recent trends and possible physical mechanism. *Climate Dynamics* 42, 2655-2674. DOI: 10.1007/s00382-013-1885-7

Wehner, M., Castillo, F., Stone, D. 2017. The Impact of Moisture and Temperature on Human Health in Heat Waves. *Oxford Research Encyclopedia of Natural Hazard Science*. DOI: 10.1093/acrefore/9780199389407.013.58

Xie, B., Zhang, Q., Ying, Y. 2011. Trends in Precipitation Water and Relative Humidity in China: 1979-2005. *Journal of Applied Meteorology and Climatology* 50 (10), 1985-1994. DOI: 0.1175/2011JAMC2446.1

Ye, X.C., Li, X.H., Liu, J., Xu, C.Y., Zhang, Q. 2013. Variation of Reference Evapotranspiration and Its Contributing Climatic Factors In The Poyang Lake Catchment, China. *Hydrological Processes* 28 (25), 6151–6162. DOI: 10.1002/hyp.10117

Xu, Z., Tang, Y., Connor, T., Li, D., Li, Y., Liu, J. 2017. Climate Variability and Trends at a National Scale. *Scientific Reports* 7, 3258. DOI: 10.1038/s41598-017-03297-5

sciendo

Journal of Environmental Geography 13 (3–4), 51–60.

DOI: 10.2478/jengeo-2020-0012
ISSN 2060-467X

A SOLUTION TO TREAT MIXED-TYPE HUMAN DATASETS FROM SOCIO-ECOLOGICAL SYSTEMS

Lisa B. Clark[1], Eduardo González[1,2*], Annie L. Henry[1], Anna A. Sher[1*]

[1]Department of Biological Sciences, University of Denver, Denver, CO, 80208-9010
[2]Department of Biology, Colorado State University, Fort Collins, CO, 80523
*Corresponding author, e-mail: edusargas@hotmail.com

Research article, received 26 August 2020, accepted 8 December 2020

Abstract

Coupled human and natural systems (CHANS) are frequently represented by large datasets with varied data including continuous, ordinal, and categorical variables. Conventional multivariate analyses cannot handle these mixed data types. In this paper, our goal was to show how a clustering method that has not before been applied to understanding the human dimension of CHANS: a Gower dissimilarity matrix with partitioning around medoids (PAM) can be used to treat mixed-type human datasets. A case study of land managers responsible for invasive plant control projects across rivers of the southwestern U.S. was used to characterize managers' backgrounds and decisions, and project properties through clustering. Results showed that managers could be classified as "federal multitaskers" or as "educated specialists". Decisions were characterized by being either "quick and active" or "thorough and careful". Project goals were either comprehensive with ecological goals or more limited in scope. This study shows that clustering with Gower and PAM can simplify the complex human dimension of this system, demonstrating the utility of this approach for systems frequently composed of mixed-type data such as CHANS. This clustering approach can be used to direct scientific recommendations towards homogeneous groups of managers and project types.

Keywords: Gower's similarity coefficient, partition around medoids clustering, human dimension, coupled human and natural systems, land management

INTRODUCTION

The human dimension of biological conservation, ecological restoration, and environmental management in a broad sense is a recent, growing focus in the scientific literature as an important component of coupled human and natural systems (CHANS, a.k.a. socio-ecological systems, Liu et al., 2007). When considering human systems, both within and separate from CHANS, large datasets are often involved due to the complex and varied nature of survey data. The CHANS framework can also yield data that are challenging to work with due to the interconnections between systems and data that encompasses multiple scales. Multivariate analyses are therefore frequently used, however survey and ecological data often include mixed types of variables (i.e., continuous, ordinal, and categorical), which cannot be treated by most conventional multivariate tests. For example, while cluster analyses are commonly used in social sciences, most use well known distance metrics such as Euclidean (e.g., García-Llorente et al., 2011) or Bray Curtis (e.g., Higuera et al., 2013), which cannot handle mixed data.

Gower dissimilarity matrices with clustering using partitioning around medoids (PAM) have been used recently as a new solution to the problem of mixed data in other disciplines, such as biomedical sciences, ecology, and socioeconomics (Table 1), but never in CHANS before now. The Gower similarity coefficient is specifically designed to deal with mixed data, which becomes even more likely when combining human and natural variables as found in CHANS. Gower also has additional advantages such as allowing for missing values and for different weights to be assigned to each variable (Gower, 1971; Legendre and Legendre, 2012). PAM is an alternative for the popular, non-hierarchical k-means method. Unlike those methods, PAM accepts other distance metrics besides Euclidean and is useful for relatively small sample sizes with outliers (Borcard et al., 2011; Kaufman and Rousseeuw, 1990).

This study illustrates the use of Gower distances with PAM to investigate the human dimension of coupled systems in a case study of managers involved in the control of an invasive tree (*Tamarix spp.*) in the riparian southwestern U.S. Of specific interest was whether there were profiles of managers or projects (based on their education, management role, experience, etc.) that were associated with particular management decisions. More generally, this study examines how characteristics and decisions of this population of managers and their projects could be more easily described through clustering. While many restoration ecology studies have inventoried management actions in river restoration projects (Bernhardt et al., 2007; Morandi et al., 2014), to the authors' knowledge, an in-depth, quantitative exploration of the characteristics of managers and their projects has not been done (except see Sher et al., 2020). Previous literature on the human dimension of

Table 1 Examples of papers using Gower similarity coefficients with partitioning around medoids (PAM) clustering to treat mixed data types.

Field	Examples
Biomedical science	Han et al. 2014, Canul-Reich et al. 2015, Hummel et al. 2017
Genetics	Krichen et al. 2008, Stefani et al. 2014
Marketing/Analytics	Silva et al. 2016, Lismont et al. 2017, Arunachalam and Kumar 2018
Sports research	Akhanli and Hennig 2017
Ecology	Williams et al. 2011, Pimenta et al. 2017
Socioeconomics	Kühne et al. 2010, Gellynck et al. 2011, Hennig and Liao 2013, Iparraguirre et al. 2013, Maione et al. 2018
Sociology	Bohensky et al. 2016, King et al. 2016

This selection was obtained from a search in Google Scholar using the chain "Gower and partitioning around medoids" done on Mar 21, 2018 that yielded 410 results. The list is not exhaustive.

restoration ecology has only focused on one aspect of decision-making such as partnerships or political input (e.g., Kallis et al., 2009; Oppenheimer et al., 2015), despite the myriad of aspects that may be important, including education level, governing organization, and collaboration. It was hypothesized that the proposed statistical method would give interpretable, meaningful clusters of managers, types of projects, and types of management decisions. We then tested the hypothesis that management decisions could be predicted by characteristics of managers and/or projects. This is important because if managers with particular characteristics are consistently making specific management decisions such as choosing to monitor their projects, then scientific recommendations regarding those decisions can be more accurately targeted toward the relevant managers.

We believe that this novel application of Gower distances with PAM will be useful to within any field that may study the natural-human interface with mixed-type data sets, including not only restoration ecology but also human geography, environmental sociology, and environmental psychology.

METHODS

Case study

Tamarix spp. (tamarisk, saltcedar) is a shrubby tree native to Eurasia that can grow in monocultures along riverways and impacts wildlife habitat (Bateman et al., 2013; Sogge et al., 2013; Strudley and Dalin, 2013), soil salinity (Ohrtman and Lair, 2013), and native plant communities (Friedman et al., 2005; Merritt and Poff, 2010). *Tamarix* is one of the most pervasive invasive riparian plants across the southwest U.S. and has also invaded other arid and semi-arid world regions such as Mexico, Argentina, Australia and South Africa (Sher, 2013). Removal of *Tamarix* is a common practice in river management (González et al., 2015), and there are many methods managers use to remove this species, including a broadly-dispersed biological control (Bean and Dudley, 2018). These projects are conducted on lands owned by a variety of agencies including federal (e.g., Bureau of Reclamation), state (e.g., state natural resource departments), local (e.g., conservancy districts), non-profit (e.g., The Nature Conservancy), and private (e.g., individual landowners).

In order to investigate the human dimension of the restoration of *Tamarix*-dominated lands, land managers of *Tamarix* removal projects were identified from a large dataset originally collected to assess the effects of removal method on vegetation (Fig. 1; see González et al., 2017). This was a collaborative effort of 16 research institutions; sites included all locations across the southwestern U.S. where data were available, distributed across the Upper Colorado, Lower Colorado, and Middle Rio Grande river basins. These managers were invited to participate in an online survey and in-person interviews in order to assess whether management decisions in these projects were associated with individual characteristics of those managers or projects. Information about the managers' backgrounds was needed, as well as the approach to restoration specific to each of their projects. The online survey was administered through Qualtrics to land managers. The 20-minute survey was tested through multiple iterations using mock interviews and through Qualtrics by trusted land managers and collaborators to ensure clarity.

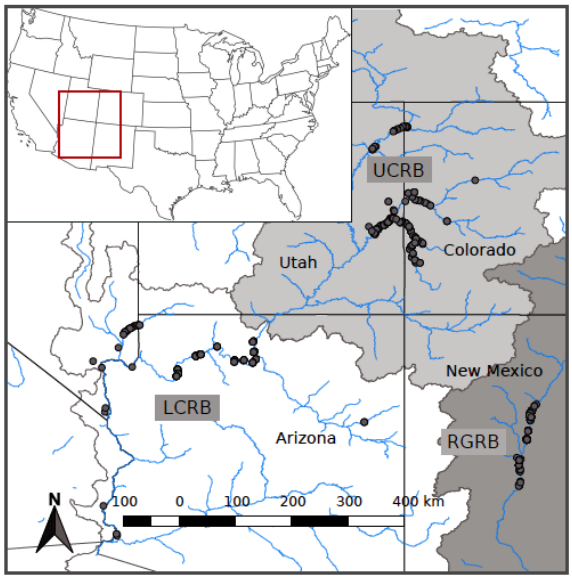

Fig. 1 Map of study area.
UCRB – Upper Colorado River Basin; LCRB – Lower Colorado River Basin; RGRB – Rio Grande River Basin. Points are *Tamarix* removal project sites

The survey was approved by the University of Denver Institutional Review Board (#816375-5), and it was fielded from August 2016 to March 2017 (Clark et al., 2019). We contacted 46 managers via email or phone; only one manager who was contacted did not complete the survey, thus our final sample size was 45 managers. The subsequent survey results encompassed 78 projects including 227 sites where *Tamarix* was treated (93% of treated sites originally sampled for vegetation data reported by González et al., 2017a; 2017b). See Table 2 for diversity of respondents. Seventeen managers had more than one project and 54 projects had multiple managers. Some of the variables were related to each manager, and others to specific projects. Thus, the data were considered in terms of managers (n=45) and projects (n=78). As this study represents nearly all *Tamarix* removal projects in the southwestern U.S. over the last 20 years, our sample size can be considered highly representative of this population.

The survey results produced continuous, ordinal, and categorical variables, organized into two general categories: characteristics and decisions (Table 3). Within each of these, some variables were specific to projects, while others were specific to managers regardless of the project, such as education level. The characteristics variables included: governing agency or organization ("agency"; Table 3), education, experience level, and management role. Agency was considered both in relation to the manager and to the project, as it often differed. Experience was also considered for the manager as an overall measure of management experience and for the project as a measure of location-specific experience. The decision variables covered the manager's goals for each project, degree of collaboration across agencies, information sources, *Tamarix* removal method, and monitoring methods. For information sources, managers were asked to rate the influence of information provided by particular agencies or organizations (e.g., formal: scientific articles; informal: peer conversations) on their decision-making, resulting in a count of the number of influential sources rated "somewhat influential" or higher. In the survey, managers also selected monitoring frequency for each type of monitoring method (e.g., physical, chemical, biological) but because most managers used more than one type and we were interested in how frequently any type of monitoring was done rather than each type, we created an ordinal variable for overall monitoring frequency where the highest frequency for any method was recorded.

Cluster analysis

Four cluster analyses were run for each of the variable categories – manager characteristics, project-specific characteristics, general management decisions, and project-specific management decisions – using partitioning around medoids (PAM method; Borcard et al., 2011; Kaufman and Rousseeuw, 1990) on a Gower dissimilarity matrix (Gower, 1971; Legendre and Legendre, 2012). The weighting of each set of variables was adjusted for each cluster analysis to give equal

Table 2 Summary of respondent characteristics

Characteristic	**Proportion of each category**
Gender	Men 47% | Women 53%
Education level	High school 4% | Bachelors 33% | Masters 47% | Doctorate 18%
Experience level	< 11 years 24% | 11-20 years 22% | > 20 years 42% | Did not identify as a land manager 9%
Owning agencies	*Federal* 49% | *State* 18% | *Local* 12% | *Private/Non-profit* 14% | *More than one agency* 8%
	Federal includes: National Park Service, Bureau of Land Management, US Fish and Wildlife Service, Bureau of Reclamation State includes: 1 state park service, 2 state natural resource departments, 3 state fish and wildlife services Local includes: 3 municipalities, 1 tribe, 1 conservation district Private/Non-profit includes: 1 non-profit, 1 private company, 1 university, individuals
Managing agencies	*Federal* 29% | *State* 12% | Local 9% | *Private/Non-profit* 14% | *More than one agency* 36%
	Federal includes: National Park Service, Bureau of Land Management, US Fish and Wildlife Service, Bureau of Reclamation State includes: 1 state natural resource department, 1 state fish and wildlife service, 1 conservancy district Local includes: 2 municipalities, 1 tribe Private/Non-profit includes: 1 non-profit, 1 private company, individuals
Employing agencies	*Federal* 47% | *State* 11% | *Local* 16% | *Non-profit* 20% | *Private* 4%
	Federal includes: National Park Service, Bureau of Land Management, US Fish and Wildlife Service, Bureau of Reclamation, US Army Corps of Engineers State includes: 4 state natural resource departments Local includes: 2 municipalities, 1 county, 2 conservation districts Non-profit includes: 3 non-profits, 1 private company, 1 university

Percentages are calculated based on the total number of managers (for gender, education, experience, and employing agency) or projects (for owning and managing agency).

Table 3 Twenty-four survey variables used for analysis, by cluster category: characteristics vs. decisions for managers and for specific projects.

Category	Variable type	Variable	Description
Manager characteristics	continuous	Management role	Number of roles out of: directly make decisions, implement decisions made by others, oversee projects with input from a partnership, collect data, other
	ordinal	Overall experience	<11 years, 11-20 years, >20 years
	ordinal	Education	High school, Bachelors, Masters, PhD
	categorical	Employing agency	Private, non-profit, local, state, federal
Project-specific charac.	ordinal	Experience in project area	<11 years, 11-20 years, >20 years
	categorical	Managing agency of proj.	Private/non-profit, local, state, federal, collaborative
	categorical	Owning agency of project	Private/non-profit, local, state, federal, collaborative
Management decisions	categorical	Type of inform. sources	Formal (e.g., peer-reviewed literature, conference talks), informal (e.g., conversations, past experience), mixed
	continuous	Number of information sources	-
	continuous	Number of monitoring methods	Includes visual, biological, physical, and chemical
	ordinal	Frequency of monitoring	Variable or <every 4 yrs, every 1-2 yrs, >annual
	continuous	Number of monitoring groups	Includes self, other personnel within agency, collaborators, university scientists, private consultants, other
	continuous	Number of collaborating groups	Includes federal personnel, state personnel, private consultants, scientists, neighbors/peers, other
	continuous	Number of collab. scientist groups	Includes federal, state, county, private consultants, non-profit agency, university, other
	continuous	Number of researching groups	Includes self, university scientists, other scientists
	continuous	Removal method (four variables)	Proportion of sites with each method (biocontrol only, cut-stump, heavy machinery, and burning) by manager
Project-specific decisions	categorical	Goals (14 variables)	Yes/no for each of 14 goals within the following categories: Plant, Wildlife, Water, People, Other
	continuous	Removal method (four variables)	Proportion of sites with each method (biocontrol only, cut-stump, heavy machinery, and burning) within a project

weight to each variable as the number of sub-variables was not consistent. However, for the project-specific management decisions, the goals of "none", "other", and "livestock forage" were only rarely selected in the surveys and drove the clustering in preliminary analyses, so were given a lower weight than the other goals.

All clustering methodologies assign observations to the same cluster based on algorithms that consider the distance (or similarity) between observations. The clustering algorithm used by the PAM method is an extension of the popular K-means algorithm, which uses Euclidean distances only and therefore cannot deal with categorical data. Unlike K-means, the PAM algorithm can be fed with a dissimilarity matrix, a matrix that contains all pairwise distances between the observations, instead of the raw data. This broadens the choice of distance measures to others that allow continuous as well as ordinal and categorical variables. The PAM algorithm computes k representative observations, called medoids, through an iterative process that ends when the average dissimilarity of the medoids to all the observations in the cluster is the minimal possible. As in K-means, the number of clusters (k) has to be defined *a priori*. We used the optimum average silhouette width (ASW) method to estimate the best number of clusters (Kaufman and Rousseeuw, 1990). In this study, the number of cluster groups was based on the highest average silhouette width that had a feasible logical interpretation, determined by significant differences on the survey variables between cluster groups using chi-square or Mann-Whitney U comparisons for each variable.

The dissimilarity matrix that was used to feed the PAM procedure was computed using the Gower similarity coefficient (Gower, 1971; Legendre and Legendre, 2012). The Gower metric has other advantages besides allowing mixed data (i.e., data that includes continuous, ordinal, and categorical variables). First, all variables including ordinal and categorical are scaled to [0,1] so the requirement of the PAM method of all variables being dimensionally homogeneous (Borcard et al., 2011) is met. Normality for continuous variables is not required. Second, missing values are discarded from the calculation without the need of removing the observation or the variable; so the dataset can include missing values and no power is lost. Third, it is possible to set different

weights for each variable. In our case study, we assigned weights to the variables so that each set of variables (i.e., collaboration, role, etc.) was equal in weight. All continuous variables were scaled before calculating the Gower coefficients. The Gower's similarity coefficient between two observations (s_{ij}) is calculated following the equation:

$$S_{ij} = \frac{\sum_{k=1}^{p} w_{ijk}\, s_{ijk}}{\sum_{k=1}^{p} w_{ijk}} \quad (1),$$

where s_{ij} denotes the similarity of observations i and j for the k^{th} variable, and wij is the weight given to the k^{th} variable (a weight of 0 is given in case of missing values for i or j). The similarity s_{ijk} is defined for continuous and ordinal variables as

$$1 - \left| x_{ik} - x_{jk} \right| / r \quad (2),$$

where r is the range of the variable. For categorical variables, s_{ijk} is defined as 0 if x_{ik} and x_{jk} differ and 1 if x_{ik} and x_{jk} are the same. The Gower's dissimilarity matrix is computed by transforming the similarities of all pairs of observations as

$$\sqrt{(1 - s_{ij})} \quad (3).$$

The Gower coefficients were calculated using the function daisy of the package cluster (Maechler et al. 2018) and the PAM clustering were run using the function pamk of the package fpc (Hennig, 2013) in R 3.4.1 (R Core Team, 2017).

Cluster assessment

In order to define the profiles of the resulting cluster groups, the mean response to each of the variables used to run the cluster analysis for each of the four cluster group pairs were compared Pearson's chi-square tests, for categorical data, or Mann-Whitney U, for continuous data, in JMP 13.0.0 (SAS Institute, 2014). Mann-Whitney is a non-parametric test, selected because our continuous variables were rarely normally distributed. To determine if the "characteristic" cluster groups (both for managers and for projects) helped explain "decisions" variables, the same approach was used with characteristic clusters as the independent variable and individual decisions variables as the dependent variables. To account for the increased risk of a Type I error due to the large number of tests, a Bonferroni adjustment was applied to the alpha based on the number of analyses for each sub-question.

RESULTS AND DISCUSSION

In this case study, Gower similarity coefficients and PAM clustering was used to summarize survey data comprised of mixed variable types in a coupled human and natural system. This approach created four clear sets of clusters relating to manager characteristics, project characteristics, management decisions, and project-specific decisions based on survey responses by managers of invasive *Tamarix* removal projects. Surprisingly, the characteristic clusters did not, for the most part, explain management decisions, suggesting that individual managers did not make choices based on their background, but instead that these decisions may be more the product of the agency or collaborative group and determined by their resources and/or priorities (Sher et al., 2020). These results demonstrate the utility of this analysis approach and provide insight into the structure of this specific system, which can assist understanding of and thus communication with managers.

Previous research that has included surveys of managers has rarely investigated the linkage between managers backgrounds and management actions taken as determined by combinations of factors (but see Sher et al., 2020). More often, surveys of approaches (Bernhardt et al., 2007; Morandi et al., 2014) or attitudes of managers has been assessed (e.g., Curtis and de Lacy, 1998, Padgett and Imani, 1999), typically with very little if any quantitative hypothesis testing (but see Clark et al., 2019). At least one such study has implemented a multivariate clustering method for identifying opinions and attitudes of land managers toward implementing conservation initiatives (Knight et al., 2010), but no subsequent analysis appears to have been done with these clusters. In another, background was linked to management approach, but these traits were only considered singly, rather than contributing to a multi-dimensional profile (Raymond and Brown, 2011). It is our hope that this method of using Gower similarity coefficients and PAM clustering can help facilitate more studies of the hypothesized causal relationships between elements, as was done here.

Cluster results

For each of the four variable groups, distinct pairs were created by the cluster analysis (Table 4-7). Coefficients are either Mann-Whitney U (continuous variables) or Pearson's chi-square (ordinal and categorical variables) and indicate significant differences between the cluster groups if bolded ($p < 0.05$). The manager characteristics cluster groups were explained primarily by employing agency, education, and management role, with an equal number of managers in each group (Table 4). Managers in group 1 ("federal multitaskers") had lower education, worked for mostly federal agencies, and had more management roles including overseeing projects with input from a partnership, relative to group 2 ("educated specialists").

Projects were distinguished by all of the variables used in the analysis: local experience, managing agency, and owning agency (Table 5). Most projects in the first group were characterized by having more locally-experienced managers and tending to be owned and managed by larger or collaborative entities ("public") whereas group 2 projects ("private") were owned and

Table 4 Description of cluster groups created from manager characteristics (ASW=0.22), Group 1: Federal multitaskers (n=22), Group 2: Educated specialists (n=23)

Variable	Weight	Group 1	Group 2	coefficient	P
Role					
Direct management role	0.05	64%	65%	0.11	0.92
Implement decisions made by others	0.05	36%	9%	3.38	0.07
Oversee projects with input from a partnership	0.05	**86%**	**39%**	**11.62**	**<0.001**
Collect data	0.05	50%	26%	2.83	0.09
Median breadth of management roles (0-4)	0.05	**3**	**1**	**8.52**	**0.004**
Experience					
Most common experience level	0.25	>20 years	11-20 years	5.92	0.12
Education					
Most common education level	0.25	**Bachelors**	**Masters**	**18.20**	**<0.001**
Agency					
Most common employing agency	0.25	**Federal**	**Non-profit/ University**	**19.21**	**<0.001**

Table 5 Description of cluster groups created from project-specific characteristics (ASW=0.51), Group 1: Public (n=49), Group 2: Private (n=25)

Variable	Weight	Group 1	Group 2	coefficient	P
Experience					
Most common local experience level	0.33	**11-20 years**	**<11 years**	**8.84**	**0.01**
Managing agency					
Most common managing agency	0.33	**Collaborative**	**Private/Non-profit**	**63.28**	**<0.001**
Owning agency					
Most common owning agency	0.33	**Federal**	**Private/Non-profit /University**	**53.87**	**<0.001**

managed mostly by smaller organizations such as private companies or non-profits.

There were two groups from the general management decision cluster analysis; these were significantly distinguished by information sources, monitoring, and the use of heavy machinery to remove *Tamarix* (Table 6). The first group ("quick and active") used fewer sources of information but those sources were a mix of formal and informal; they used less comprehensive but more frequent monitoring and more heavy machinery than the other group ("thorough and careful"). The project-specific management decisions (Table 7) were characterized by the selection of goals related to ecosystem health such as native plant diversity or habitat improvement and more removal by burning (group 1: "ecocentric") while group 2 ("limited scope") had few goals selected but did select "none" or "other" (e.g., community involvement, water conservation, research) goals more often and had more removal by heavy machinery. These groupings provided an overview of the managers involved in *Tamarix* removal projects and the decisions they make, helping us understand which traits or aspects of projects are likely to be aligned.

This clustering tool also facilitated the analysis of relationships between variables. Numbers in Table 8 are the coefficients from either Mann-Whitney U or Pearson's chi-square tests depending on the type of variable. No significant relationships were found with Bonferroni adjusted α=0.004 and α=0.003 for general and project-specific decisions, respectively. Counter to predictions, no strong relationships between manager characteristics and decisions made about projects (as shown by non-significant pairwise comparisons with individual variables; Table 8a) were found (e.g., Hagger et al., 2017; Martin-Lopez et al., 2007; Roche et al., 2015). This result suggests that either managers exhibit no bias in decision making in these restoration projects based on their own backgrounds, and/or that there are enough other controls in place through mechanisms to overwhelm any such bias (Clark et al., 2019, Sher et al., 2020). These controls are likely to include the constraints and goals of specific agencies, the influence of collaborators, and the availability of resources for a given project. It is also possible that any influence of manager characteristics on decisions were too small to be detected by a sample of this size.

Similarly, whether projects were "public" or "private" did not strongly predict management decisions made about those projects, although private projects were more likely to have the listed goals, especially aesthetics and native plant diversity, than public projects (Table 8b). Public projects were more likely to have used biological control, but these results were not statistically

Table 6 Description of cluster groups created from general management decisions (ASW=0.18), Group 1: Quick and active (n=24), Group 2: Thorough and careful (n=20)

Variable	Weight	Group 1	Group 2	coefficient	P
Information source					
Most common type of information sources	0.125	**mix**	**formal**	**15.40**	**<0.001**
Median breadth of information sources (0-22)	0.125	**13**	**21**	**7.82**	**0.005**
Monitoring					
Median breadth of monitoring methods (0-4)	0.125	**2**	**3**	**10.11**	**0.002**
Most common monitoring frequency	0.125	**> once a year**	**> once a year or < every 4 years**	**8.09**	**0.04**
Collaboration					
Median breadth of monitoring groups (0-6)	0.0625	2	3	2.54	0.11
Median breadth of collaborating groups (0-7)	0.0625	3	2.5	0.10	0.75
Median breadth of science collaborators (1-7)	0.0625	4	4.5	0.78	0.38
Median breadth of researching groups (0-4)	0.0625	2	1	1.40	0.24
Removal method					
Mean proportion of biocontrol only	0.0625	0.18	0.05	2.98	0.08
Mean proportion of cut-stump	0.0625	0.18	0.28	3.42	0.06
Mean proportion of heavy machinery	0.0625	**0.39**	**0.09**	**4.07**	**0.04**
Mean proportion of burning	0.0625	0.16	0.19	0.42	0.52

Table 7 Description of cluster groups created from project-specific decisions (ASW=0.34), Group 1: Ecocentric (n=43), Group 2: Limited scope (n=29)

Variable	Weight	Group 1	Group 2	coefficient	P
Plant-related goals					
Native plant diversity	0.0606	**93%**	**28%**	**33.37**	**<0.001**
Ecosystem resilience	0.0606	**79%**	**7%**	**36.09**	**<0.001**
Exotic plant removal	0.0606	**95%**	**76%**	**6.01**	**0.01**
Wildlife-related goals					
Habitat improvement	0.0909	**100%**	**31%**	**41.06**	**<0.001**
Endangered species	0.0909	**65%**	**0%**	**30.90**	**<0.001**
Water-related goals					
Channel maintenance	0.0606	21%	14%	0.60	0.44
Restore over-bank flooding	0.0606	**60%**	**17%**	**13.20**	**<0.001**
Water quality	0.0606	**28%**	**3%**	**7.00**	**0.008**
People-related goals					
Aesthetics	0.0606	40%	38%	0.02	0.89
Recreation	0.0606	28%	34%	0.35	0.55
Wildfire mitigation	0.0606	**63%**	**21%**	**12.37**	**<0.001**
Other goals					
Livestock forage	0.0303	9%	0%	2.86	0.09
Other	0.0303	**2%**	**28%**	**10.10**	**0.002**
None	0.0303	**0%**	**14%**	**6.28**	**0.01**
Removal method					
Mean proportion of biocontrol only	0.0455	0.09	0.14	0.04	0.85
Mean proportion of cut-stump	0.0455	0.22	0.33	0.53	0.47
Mean proportion of heavy machinery	0.0455	**0.23**	**0.33**	**6.48**	**0.01**
Mean proportion of burning	0.0455	**0.25**	**0.11**	**4.57**	**0.03**

significant with an adjusted alpha of $p<0.003$. However, it should be noted that as this study sample represented a near-census of *Tamarix* projects in the southwestern U.S., such descriptive statistics may still be meaningful. Projects that were owned and managed privately or by non-profits may have had the flexibility to have more specific and customized goals than those projects that required buy-in from larger or more diverse stakeholders.

Taken together, this information can inform future collaborations with managers and scientists in this coupled system by giving context to their interactions. For example, managers who are federal multitaskers may not have the capacity to try new methods but educated specialists may be more willing and able to do so. Thus, educated specialists may be the best candidates to try innovative new practices and could be more directly targeted in communications and dissemination. Additionally, increased understanding of managers by scientists is essential for building trust in relationships with managers, which is crucial to the success of any collaboration (Vangen and Huxham, 2003).

Method assessment

When treating mixed-type data from CHANS systems, there are many advantages to using cluster analyses and PAM with Gower in particular. When cluster analysis is used, the whole dataset can be utilized rather than having to choose a priori which variables will be the most important, which has been the usual practice to treat mixed-type data to date. With PAM clustering and Gower, categorical variables – which are very common when assessing characteristics of people (e.g., education level or gender) – do not need to be omitted or converted

Table 8 Pairwise comparisons between manager (a) and project (b) characteristic cluster groups (columns) and management decisions (rows)

	Characteristic cluster groups			
a) General approach	**Federal multitaskers**	**Educated specialists**	**coefficient**	**P**
Information type	mixed/formal	mixed	0.79	0.67
Number of information sources	19	17	2.07	0.15
Number of monitoring groups	3	2	0.02	0.89
Number of monitoring methods	2	2	0.01	0.92
Monitoring frequency	> once a year	every 1-2 years	2.07	0.56
Number of collaborating groups	3	3	0.0006	0.98
Number of science collaborators	4	4	0.59	0.44
Number of researching groups	2	1	3.06	0.08
Biocontrol	0.15	0.09	2.18	0.14
Cut-stump	0.25	0.20	0.91	0.34
Heavy machinery	0.25	0.25	0.03	0.87
Burning	0.14	0.20	0.006	0.94
b) Project-specific approach	**Public**	**Private**	**coefficient**	**P**
Native plant diversity	**57%**	**84%**	**5.18**	**0.03**
Ecosystem resilience	47%	56%	0.55	0.46
Exotic plant removal	83%	96%	2.53	0.11
Habitat improvement	68%	80%	1.16	0.28
Endangered species	36%	80%	0.42	0.52
Channel maintenance	19%	16%	0.11	0.74
Restore over-bank flooding	40%	48%	0.38	0.54
Water quality	17%	20%	0.10	0.75
Aesthetics	**28%**	**60%**	**7.18**	**0.01**
Recreation	28%	36%	0.54	0.46
Wildfire mitigation	38%	60%	3.10	0.08
Livestock forage	2%	12%	3.03	0.08
Other	17%	4%	2.53	0.11
None	9%	0%	2.25	0.13
Biocontrol	**0.13**	**0.06**	**4.44**	**0.04**
Cut-stump	0.29	0.19	2.21	0.14
Heavy machinery	0.15	0.27	0.07	0.79
Burning	0.18	0.20	0.0006	0.98

in some way to a nominal numerical value that is then improperly represented. In addition to dealing with mixed type variables, PAM is also more robust to outliers than traditional methods (Arunachalam and Kumar, 2018; Maione et al., 2018), can deal with non-symmetrical data (Gellynck et al., 2011), and can be used for relatively small sample sizes like ours as is also common with human datasets (Iparraguirre et al., 2013; King et al., 2016). The Gower coefficient also allows for weighting of variables and missing values in the dataset. Unlike PAM, Gower is sensitive to outliers (Sander and Lubbe, 2018). Despite this drawback, this analysis method is one of the best solutions to dealing with mixed data types in a multivariate setting.

CONCLUSIONS

This study has demonstrated the application of a clustering method used in other fields of study to a CHANS context. PAM with Gower is useful in this study due to the need to comprehensively reflect complex data. In this way, managers and their decisions can be understood in a holistic manner and the cluster groupings can inform future recommendations and the allocation of resources. This method also has the potential to be useful in other CHANS studies such as endangered species management, grazing management, or water management where there are even more factors involved with the addition of politics and federal or state regulations.

Acknowledgements

This research was supported by a National Science Foundation Dynamics of Coupled Natural and Human Systems award (project number 1617463), a Pustmueller Grant, and the University of Denver. The authors thank all managers who participated in the survey and/or interview. The assistance of Carly McGuire, Madison Sligh, and Kayleigh Kearnan with data collection and entry was much appreciated. Thanks also go to N. Sayre and R. Lave for help with data collection protocols.

References

Akhanli, S.E., Hennig, C. 2017. Some Issues in Distance Construction for Football Players Performance Data. Archives of Data Science 2(1). DOI: 10.5445/KSP/1000058749/09

Arunachalam, D., Kumar, N. 2018. Benefit-based consumer segmentation and performance evaluation of clustering approaches: An evidence of data-driven decision-making. *Expert Systems with Applications* 111, 11–34. DOI: 10.1016/j.eswa.2018.03.007

Bateman, H.L., Paxton, E.H., Longland, W.S. 2013. Tamarix as Wildlife Habitat. In Sher, A.A., Quigley, M.T. (Eds.) Tamarix: A Case Study of Ecological Change in the American West. Oxford University Press, New York, 168–188. DOI: 10.1093/acprof:osobl/9780199898206.003.0010

Bean, D., Dudley, T. 2018. A synoptic review of *Tamarix* biocontrol in North America: tracking success in the midst of controversy. *BioControl* 63(3), 361–376. DOI: 10.1007/s10526-018-9880-x

Bernhardt, E.S., Sudduth, E.B., Palmer, M.A., Allan, J.D., Meyer, J.L., Alexander, G., Follastad-Shah, J., Hassett, B., Jenkinson, R., Lave, R., Rumps, J., Pagano, L. 2007. Restoring rivers one reach at a time: Results from a survey of U.S. river restoration practitioners. *Restoration Ecology* 15, 482–493. DOI: 10.1111/j.1526-100X.2007.00244.x

Bohensky, E.L., Kirono, D.G.C., Butler, J.R.A., Rochester, W., Habibi, P., Handayani, T., Yanuartati, Y. 2016. Climate knowledge cultures: Stakeholder perspectives on change and adaptation in Nusa Tenggara Barat, Indonesia. *Climate Risk Management* 12, 17–31. DOI: 10.1016/j.crm.2015.11.004

Borcard, D., Gillet, F., Legendre, P. 2011. Numerical Ecology with R. Springer, New York.

Canul-Reich, J., Hernández-Torruco, J., Frausto-Solis, J., Méndez Castillo, J.J. 2015. Finding relevant features for identifying subtypes of Guillain-Barré Syndrome using Quenching Simulated Annealing and Partitions Around Medoids. *International Journal of Combinatorial Optimization Problems and Informatics* 6(2), 11–27.

Clark, L.B., Henry, A.L., Lave, R., Sayre, N.F., González, E., Sher, A.A. 2019. Successful information exchange between restoration science and practice. *Restoration Ecology* 27(6), 1241–1250. DOI: 10.1111/rec.12979

Curtis, A., de Lacy, T. 1998. Landcare, stewardship and sustainable agriculture in Australia. *Environmental Values* 7, 59–78. DOI: https://www.jstor.org/stable/30302269

Friedman, J.M., Auble, G.T., Shafroth, P.B., Scott, M.L., Merigliano, M.F., Freehling, M.D., Griffin, E.R. 2005. Dominance of non-native riparian trees in western USA. *Biological Invasions* 7(4), 747–751. DOI: 10.1007/s10530-004-5849-z

García-Llorente, M., Martín-López, B., Nunes, P.A.L.D., González, J.A., Alcorlo, P., Montes, C. 2011. Analyzing the Social Factors That Influence Willingness to Pay for Invasive Alien Species Management Under Two Different Strategies: Eradication and Prevention. *Environmental Management* 48(3), 418–435. DOI: 10.1007/s00267-011-9646-z

Gellynck, X., Kühne, B., Weaver, R.D. 2011. Relationship quality and innovation capacity of chains: the case of the traditional food sector in the EU. *Proceedings in Food System Dynamics* 2(1), 1–22. DOI: 10.22004/ag.econ.100498

González, E., Sher, A.A., Anderson, R.M., Bay, R.F., Bean, D.W., Bissonnete, G.J., Bourgeois, B., Cooper, D.J., Dohrenwend, K., Eichhorst, K.D., El Waer, H., Kennard, D.K., Harms-Weissinger, R., Henry, A.L., Makarick, L.J., Ostoja, S.M., Reynolds, L.V., Robinson, W.W., Shafroth, P.B. 2017a. Vegetation response to invasive Tamarix control in southwestern U.S. rivers: A collaborative study including 416 sites. *Ecological Applications* 27(6), 1789–1804. DOI: 10.1002/eap.1566

González, E., Sher, A.A., Anderson, R.M., Bay, R.F., Bean, D.W., Bissonnete, G.J., Cooper, D.J., Dohrenwend, K., Eichhorst, K.D., El Waer, H., Kennard, D.K., Harms-Weissinger, R., Henry, A.L., Makarick, L.J., Ostoja, S.M., Reynolds, L.V., Robinson, W.W., Shafroth, P.B., Tabacchi, E. 2017b. Secondary invasions of noxious weeds associated with control of invasive Tamarix are frequent, idiosyncratic and persistent. *Biological Conservation* 213, 106–114. DOI: 10.1016/j.biocon.2017.06.043

González, E., Sher, A. A., Tabacchi, E., Masip, A., Poulin, M. 2015. Restoration of riparian vegetation: a global review of implementation and evaluation approaches in the international, peer-reviewed literature. *Journal of Environmental Management* 158, 85-94. DOI: 10.1016/j.jenvman.2015.04.033

Gower, J.C. 1971. A general coefficient of similarity and some of its properties. *Biometrics* 27(4), 857–871. DOI: 10.2307/2528823

Hagger, V., Dwyer, J., Wilson, K. 2017. What motivates ecological restoration? *Restoration Ecology* 25, 832–843. DOI: 10.1111/rec.12503

Han, S., Sung, K.R., Lee, K.S., Hong, J.W. 2014. Outcomes of laser peripheral iridotomy in angle closure subgroups according to anterior segment optical coherence tomography parameters. *Investigative Ophthalmology & Visual Science* 55, 6795–6801. DOI: 10.1167/iovs.14-14714

Hennig, C. 2013. fpc: Flexible procedures for clustering. R package version 21-5.

Hennig, C., Liao, T.F. 2013. How to find an appropriate clustering for mixed-type variables with application to socio-economic stratification. *Journal of the Royal Statistical Society. Series C: Applied Statistics* 62, 309–369. DOI: 10.1111/j.1467-9876.2012.01066.x

Higuera, D., Martín-López, B., Sánchez-Jabba, A. 2013. Social preferences towards ecosystem services provided by cloud forests in the neotropics: Implications for conservation strategies.

Regional Environmental Change 13, 861–872. DOI: 10.1007/s10113-012-0379-1

Hummel, M., Edelmann, D., Kopp-Schneider, A. 2017. Clustering of samples and variables with mixed-type data. *PloS ONE* 12(11), 1–24. DOI: 10.1371/journal.pone.0188274

Iparraguirre, J., Gentry, T., Pena, D. 2013. Vulnerability of Primary Care Organizations to the National Health Service Reform in England. *Applied Economic Perspectives and Policy* 35(4), 634–660. DOI: 10.1093/aepp/ppt021

Kallis, G., Kiparsky, M., Norgaard, R. 2009. Collaborative governance and adaptive management: Lessons from California's CALFED Water Program. *Environmental Science & Policy* 12, 631–643. DOI: 10.1016/j.envsci.2009.07.002

Kaufman, L., Rousseeuw, P. 1990. Finding Groups in Data: And Introduction to Cluster Analysis. Wiley seri. John Wiley and Sons Inc.

King, M.L., Hering, A.S., Aguilar, O.M. 2016. Building predictive models of counterinsurgent deaths using robust clustering and regression. *Journal of Defense Modeling and Simulation* 13(4), 449–465. DOI: 10.1177/1548512916644074

Knight, A. T., Cowling, R. M., Difford, M., & Campbell, B. M. 2010. Mapping human and social dimensions of conservation opportunity for the scheduling of conservation action on private land. *Conservation Biology* 24(5), 1348–1358. DOI: https://www.jstor.org/stable/40864035

Krichen, L., Martins, J.M.S., Lambert, P., Daaloul, A., Trifi-Farah, N., Marrakchi, M., Audergon, J.M. 2008. Using AFLP Markers for the Analysis of the Genetic Diversity of Apricot Cultivars in Tunisia. *Journal of the American Society for Horticultural Science* 133(2), 204–212. DOI: 10.21273/JASHS.133.2.204

Kühne, B., Vanhonacker, F., Gellynck, X., Verbeke, W. 2010. Innovation in traditional food products in Europe: Do sector innovation activities match consumers' acceptance? *Food Quality and Preference* 21(6), 629–638. DOI: 10.1016/j.foodqual.2010.03.013

Legendre, P., Legendre, L. 2012. Numerical Ecology. 3rd English. Elsevier Science, Amsterdam.

Lismont, J., Vanthienen, J., Baesens, B., Lemahieu, W. 2017. Defining analytics maturity indicators: A survey approach. *International Journal of Information Management* 37, 114–124. DOI: 10.1016/j.ijinfomgt.2016.12.003

Liu, J., Dietz, T., Carpenter, S.R., Alberti, M., Folke, C., Moran, E., Pell, A.N., Deadman, P. 2007. Complexity of Coupled Human and Natural Systems. *Science* 317, 1513–1516. DOI: 10.1126/science.1144004

Maechler, M., Rousseeuw, P., Struyf, A., Hubert, M., Hornik, K. 2018. Cluster Analysis Basics and Extensions. R package version 2.0.7-1.

Maione, C., Nelson, D.R., Barbosa, R.M. 2018. Research on social data by means of cluster analysis. *Applied Computing and Informatics* 15(2), 153–162. DOI: 10.1016/j.aci.2018.02.003

Martin-Lopez, B., Montes, C., Benayas, J. 2007. The non-economic motives behind the willingness to pay for biodiversity conservation. *Biological Conservation* 139(1-2), 67–82. DOI: 10.1016/j.biocon.2007.06.005

Merritt, D.M., Poff, N.L. 2010. Shifting dominance of riparian *Populus* and *Tamarix* along gradients of flow alteration in western North American rivers. *Ecological Applications* 20(1), 135–152. DOI: 10.1890/08-2251.1

Morandi, B., Piégay, H., Lamouroux, N., Vaudor, L. 2014. How is success or failure in river restoration projects evaluated? Feedback from French restoration projects. *Journal of Environmental Management* 137, 178–188. DOI: 10.1016/j.jenvman.2014.02.010

Ohrtman, M.K., Lair, K.D. 2013. Tamarix and Salinity: An Overview. In: Sher, A.A., Quigley, M.T. (Eds.) Tamarix: A Case Study of Ecological Change in the American West. Oxford University Press, New York, 123–145. DOI: 10.1093/acprof:osobl/9780199898206.003.0008

Oppenheimer, J.D., Beaugh, S.K., Knudson, J.A., Mueller, P., Grant-Hoffman, N., Clements, A., Wight, M. 2015. A collaborative model for large-scale riparian restoration in the western United States. *Restoration Ecology* 23(2), 143–148. DOI: 10.1111/rec.12166

Padgett, D.D., Imani, N.O. 1999. Qualitative and quantitative assessment of land-use managers' attitudes towards environmental justice. *Environmental Management* 24(4), 509–515. DOI: 10.1007/s002679900250

Pimenta, V., Barroso, I., Boitani, L., Beja, P. 2017. Wolf predation on cattle in Portugal: Assessing the effects of husbandry systems. *Biological Conservation* 207, 17–26. DOI: 10.1016/j.biocon.2017.01.008

Raymond, C.M., Brown, G. 2011. Assessing conservation opportunity on private land: socio-economic, behavioral, and spatial dimensions. *Journal of Environmental Management* 92(10), 2513–2523. DOI: 10.1016/j.jenvman.2011.05.015

R Core Team. 2017. R: A language and environment for statistical computing. R Foundation for Statistical Computing, Vienna, Austria. Online available at: http://www.R-project.org/

Roche, L.M., Schohr, T.K., Derner, J.D., Lubell, M.N., Cutts, B.B., Kachergis, E., Eviner, V.T., Tate, K.W. 2015. Sustaining Working Rangelands: Insights from Rancher Decision Making. *Rangeland Ecology and Management* 68(5), 383–389. DOI: 10.1016/j.rama.2015.07.006

Sander, U., Lubbe, N. 2018. The potential of clustering methods to define intersection test scenarios: Assessing real-life performance of AEB. *Accident Analysis & Prevention* 113, 1–11. DOI: 10.1016/j.aap.2018.01.010

SAS Institute, I. 2014. JMP version 13.0.

Sher, A.A. 2013. Introduction to the Paradox Plant. In: Sher, A.A. and Quigley, M.T. (Eds.) Tamarix: A Case Study of Ecological Change in the American West. Oxford University Press, New York:1–18. DOI: 10.1093/acprof:osobl/9780199898206.003.0001

Sher, A.A., Clark, L., Henry, A.L., Goetz, A.R.B., González, E., Tyagi, A., Simpson, I., Bourgeois, B. 2020. The Human Element of Restoration Success: Manager Characteristics Affect Vegetation Recovery Following Invasive *Tamarix* Control. *Wetlands*. DOI: 10.1007/s13157-020-01370-w

Silva, F., Teixeira, B., Pinto, T., Santos, G., Vale, Z., Praça, I. 2016. Generation of realistic scenarios for multi-agent simulation of electricity markets. *Energy* 116, 128–139. DOI: 10.1016/j.energy.2016.09.096

Sogge, M. K., E. H. Paxton, Van Riper, C. 2013. Tamarisk in Riparian Woodlands: A Bird's Eye View'. In: Sher, A.A., Quigley, M.T. (Eds.) Tamarix: A Case Study of Ecological Change in the American West. Oxford University Press, New York, 189–206. DOI: 10.1093/acprof:osobl/9780199898206.003.0011

Stefani, F.O.P., Jones, R.H., May, T.W. 2014. Concordance of seven gene genealogies compared to phenotypic data reveals multiple cryptic species in Australian dermocyboid Cortinarius (Agaricales). *Molecular Phylogenetics and Evolution* 71, 249–260. DOI: 10.1016/j.ympev.2013.10.019

Strudley, S., Dalin, P. 2013. Tamarix as Invertebrate Habitat'. In: Sher, A.A. Quigley, M.T. (eds.) Tamarix: A Case Study of Ecological Change in the American West. Oxford University Press, New York, 207–224. DOI: 10.1093/acprof:osobl/9780199898206.003.0012

Vangen, S., Huxham, C. 2003. Nurturing Collaborative Relations: Building Trust in Interorganizational Collaboration. *The Journal of Applied Behavioral Science* 39(1), 5–31. DOI: 10.1177/0021886303039001001

Williams, J.N., Hollander, A.D., Geen, A.T.O., Thrupp, L.A., Hanifin, R., Steenwerth, K., Mcgourty, G., Jackson, L.E. 2011. Assessment of carbon in woody plants and soil across a vineyard-woodland landscape. *Carbon Balance and Management* 6(1), 1–14. DOI: 10.1186/1750-0680-6-11